2006

Adaptive backstepping based online loss minimization control of an induction motor drive / by San Woo Nam.

Nam, Sang Woo

ADAPTIVE BACKSTEPPING BASED ONLINE LOSS MINIMIZATION CONTROL OF AN INDUCTION MOTOR DRIVE

By

Sang Woo Nam

A THESIS SUBMITTED IN PARTIAL FULFILLMENT OF THE

REQUIRMENTS FOR THE DEGREE OF

MASTER OF SCIENCE

LAKEHEAD UNIVERSITY

THUNDER BAY, ONTARIO

JULY 2006

Your file Votre référence
ISBN: 978-0-494-21519-7
Our file Notre référence
ISBN: 978-0-494-21519-7

Abstract

The efficiency of an induction motor (IM) can be improved by the optimum selection of a flux level in the motor. Among the numerous loss minimization algorithms (LMA), a loss-model-based approach offers a fast response and no torque pulsation. However, it requires the accurate loss model and the knowledge of the motor parameters to find the optimum flux level. Therefore, a technical difficulty in deriving the loss-model-based LMA lies in the complexity of the full loss model and the on-line parameter adaptation for the precise motor parameters.

In an effort to overcome the drawbacks of on-line loss model controllers (LMC), this thesis presents a new loss-model-based LMA for inverter-fed IM drives aiming at both high efficiency and high dynamic performance.

A new LMC is proposed for the loss minimization of vector-controlled IM drives. An IM model in d-q coordinates is referenced to the rotor magnetizing current and then an iron loss resistance is added in parallel to the magnetizing inductance. This transformation leads to no leakage inductance on the rotor side by incorporating it into other parameters. This decomposition feature into d-q components makes the derivation of the motor loss model and LMC simpler while keeping the effect of leakage inductances.

In order to achieve high dynamic performance, an adaptive backstepping based nonlinear controller (ABNC) is designed incorporating iron loss under the parameter uncertainties of rotor resistance and load torque. In proposed IM equations, no additional state variables are added while iron loss is considered. Thus, an ABNC

incorporating iron loss can be designed without much more complexity compared to the one with neglected iron loss. ABNC achieves desirable motor dynamics at any operating point while the flux level is varied by the LMC in order to reduce the input power.

Adaptive backstepping technique provides a tool to design the controller avoiding wasteful cancellations of certain nonlinearities. Another important feature of an adaptive backstepping technique is that it can derive parameter update laws simultaneously with control laws from the error dynamics. With an extra gain introduced in adaptation laws design, we take advantage of this feature by combining the ABNC with LMC, thus an on-line parameter adaptation of LMC can be obtained with no extra effort.

The complete closed loop control of the proposed LMC based IM drive is implemented in real-time using digital signal processor board DS 1104 for a laboratory 1/3 hp motor. The dynamic performance of the proposed controller and parameter adaptation features are examined. The effectiveness of the proposed loss minimization scheme through a wide range of speed regions including the field weakening region is demonstrated through computer simulation and experimental results.

Acknowledgements

I would like to express my most sincere thanks and appreciation to my supervisor, Dr. M. Nasir Uddin for his continuous and valuable guidance and encouragement throughout the program. This work would not have been possible without his support. I acknowledge the assistance from all Faculty and staff members especially, Mr. Manfred Klein and Mr. Kailash Bhatia for their assistance with my experimental work. I also thank my fellow graduate student Md Muminul Chy for the useful and pleasant discussions on both academic and non-academic topics.

Finally, I express my sincere appreciation and love to my wife, Melana Theriault for her continued support and patience during the program. I also thank my parents Mr Sung-Hee Nam and Mrs. Oak-Ja Yoo and my parents-in-law Mr Pierre Simoneau and Mrs. Nicole Bosse as well as other family members.

Table of Contents

List of Figures

List of Symbols

u_a, u_b, u_c	a, b and c stator phase voltages
$u_{a,ref}, u_{b,ref}, u_{c,ref}$	command a, b and c stator phase voltages
u_s	stator voltage complex space vector
u_{sd}, u_{sq}	d and q axis voltages
$u_{sd,ref}, u_{sq,ref}$	command d and q axis voltages
$u_{triangle}$	triangular carrier wave
i_{sa}, i_{sb}, i_{sc}	a, b and c stator phase currents
$i_{a,ref}, i_{b,ref}, i_{c,ref}$	command a, b and c stator phase current
i_s	stator current complex space vector
i_{sd}, i_{sq}	d and q axis currents
$i_{sd,ref}, i_{sq,ref}$	command d and q axis currents
ψ_s, ψ_r	flux linkage complex space vectors for stator and rotor
i_m	magnetizing current complex space vector
i_{md}, i_{mq}	d and q axis magnetizing current
i_{mr}	magnetizing current in rotor flux oriented vector control
$i_{mr,ref}$	command magnetizing current
α	complex spatial operator $e^{j2\pi/3}$

R_s, R_r	resistances of the stator and rotor windings
L_m	magnetizing inductance
L_{ls}, L_{lr}	self leakage inductance of the stator and the rotor
L_s, L_r	self inductance of the stator and the rotor
σ	leakage factor $(1 - L_m^2 / (L_s L_r))$
R_r'	referred rotor resistance $R_r' = (L_m / L_r)^2 R_r$
R_f'	iron loss resistance
R_t	parallel sum of R_r' and R_f'
L_s'	referred stator inductance $(L_s' = \sigma L_s)$
L_m'	referred magnetizing inductance $(L_m' = (1-\sigma) L_s)$
Z_p	number of pole pairs
ω_m	angular speed of the rotor
ω_{ref}	motor command speed
ω_r	electrical rotor speed $(\omega_r = Z_p \omega_m)$
ω_{sl}	speed slip
ω_e	angular speed of the rotor flux $(\omega_e = \omega_r + \omega_{sl})$
θ_r	rotor position angle
θ_{sl}	slip angle
θ_e	rotor flux angle
p	differential operator $(p \equiv \frac{d}{dt})$
T_e	developed electromagnetic torque
T_l	load torque
J	rotor inertia constant
V_{ds}	dc bus voltage for the inverter

List of Acronyms

ABNC	Adaptive Backstepping Based Nonlinear Controller
ADC	Analog to Digital Converter
DAC	Digital to Analog Converter
DSP	Digital Signal Processor
FOC	Field Oriented Control
IGBT	Inverted Gate Bipolar Transistor
IM	Induction Motor
LF	Loss Factor
LMA	Loss Minimization Algorithm
LMC	Loss Model Controller
PI	Proportional Integral
PMSM	Permanent Magnet Synchronous Motor
PWM	Pulse Width Modulation
RM	Reluctance Motor
RTI	Real Time Interface
SC	Search Controller
SVM	Space Vector Modulation
TI	Texas Instruments
VSI	Voltage Source Inverter

Chapter 1

Introduction

There has been a growing global concern over energy consumption and the environment and high energy efficiency has become one of the most important factors in the development of the products that consume electrical energy. Considering the fact that more than 50% of electrical energy produced is consumed by motors, and three-phase induction motors are most widely used in industry [1], efficiency optimization of an induction motor (IM) drive requires more attention than ever before. Most of the induction motors in industry are still operated without any means of control. In case of high-powered but relatively unsophisticated machinery such as pumps, fans, blowers, and compressors, there is little need for high dynamic performance of electric drive system, but speed control can bring significant energy savings in most cases. Even with controlled IM drives, there has been much effort to improve their efficiency. IM drive losses consist of grid loss, converter loss, motor loss and transmission loss [2-3]. In an effort to improve efficiency, there have been improvements in the materials, design and construction techniques for the equipment involved IM drives. However, converter loss and motor loss are still greatly dependent on control strategies, especially when the motor operates at light load. The efficiency optimization of IM drives can be realized in various ways by different

types of loss minimization control technique. The ideal loss minimization controller should not only achieve the minimum loss in all situations even with parameter variations, sudden changes of command speed and torque and load disturbances, but also satisfy the requirements of dynamic motor response. This thesis analyzes the previous research on this issue and presents a new loss minimization strategy for an IM drive in an attempt to overcome the drawbacks found in previous research, so that both high efficiency and high control dynamic performance are achieved.

1.1 Induction Motors

Induction motors have found very wide industrial applications, as well as in main powered home appliances. Simple and rugged design, low-cost, low maintenance and direct connection to an AC power source are the main advantages of induction motors [4-5]. The principle of induction machine operation is similar to that of the transformer. The induction motor always runs at a speed slightly less than the synchronous speed, because there is no torque production in an induction machine at synchronous speed.

Among various types of induction motors available in the market, almost 90% of the three-phase induction motors are squirrel cage motors. In squirrel-cage motors the rotor consists of uninsulated metal bars forming the "squirrel cage" and is not accessible as shown Fig.1.1. The lack of wiring and inaccessibility of the rotor gives the additional degree of ruggedness allowing them to be used in aggressive or volatile environments.

Wound-rotor induction motors are used in special applications in which the existence and accessibility of the rotor winding is an advantage. However, as they are more expensive and less reliable than squirrel-cage motors, wound-rotor motors have

been replaced by controlled drives with squirrel-cage motors. Thus, only the squirrel-cage induction motors will be considered in this thesis.

The disadvantage of induction motors is the difficulty of control. Because the induction motors are highly coupled non-linear dynamic plant, their applications in the area of the speed, position, or torque control have been limited and DC motors are still common. However, due to the progress in both control techniques and the electric drive system equipment such as power converters, sensors and microprocessors, IM has been gaining increasing popularity in industrial applications even where the precise control is required.

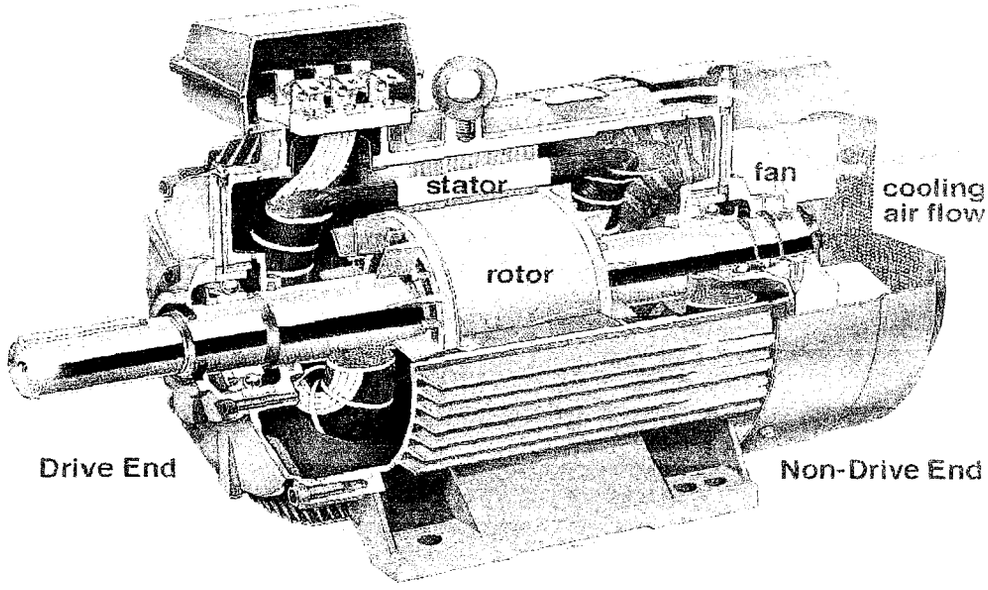

Fig.1.1: Squirrel-cage induction motor

1.2 The Efficiency of IMs

The primary purpose of an IM drive is to operate the motor at a speed and torque which is required by the operator of the motor drive. But having fulfilled that, there is an extra degree of freedom in terms of efficiency optimization. In other words, for a

given torque and speed, the motor losses can be reduced by the different selection of flux levels (or its equivalent quantity) in the motor. The basic principle of loss reduction in IM drives is explained in Fig. 1.2. If the rotor leakage inductance and core saturation are ignored for the simplicity of the notion, the current phasors of a motor at light load can be depicted as shown in Fig.1.2, where I_m, I_s and I_r are the magnetizing current, stator current and rotor current respectively. Developed torque is proportional to $I_m I_r$, the vector product of the rotor magnetizing current and rotor current. Therefore, it is possible to obtain the same torque with different combinations of magnetizing current and rotor current values. In Fig.1.2, the developed torque, which is proportional to the shaded area, is the same in all three cases.

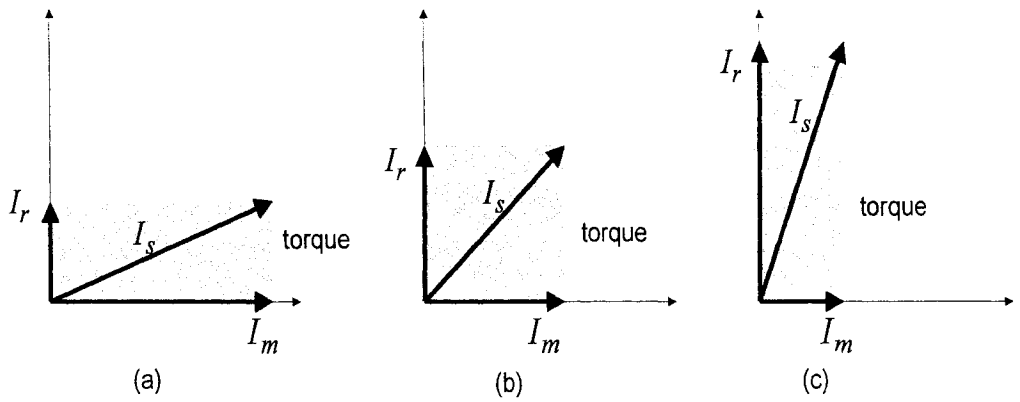

Fig.1.2: Illustration of the torque production with different magnetizing current levels: (a) Nominal, (b) Medium and (c) Low Magnetizing Current.

Type of Loss	(a)	(b)	(c)
Stator Copper Loss	Large	Small	Large
Rotor Copper Loss	Small	Medium	Large
Iron Loss	Large	Medium	Small

Table1.1: Relative loss levels for stator copper loss, rotor copper loss and core loss at three different magnetizing currents.

Table 1.1 shows the relative loss for stator copper loss, rotor copper loss and core loss at the different magnetizing current levels. For a given torque, the iron loss can be minimized by using the minimum possible magnetizing current. This also minimizes the stator copper loss components. However, to create the required torque with less magnetizing current, the rotor current must be increased by increasing the stator current and, consequently increasing the stator copper loss. Among the three different cases, (a), (b) and (c) in Fig.1.2, (b) shows the least total losses.

The conclusion is that by a proper adjustment of the magnetizing current, appropriate balance between copper and iron losses can be achieved to minimize the electromagnetic losses. Many controllers with different strategies have been proposed to achieve maximum efficiency of IM drives but, they all share the same principle, that is to find an optimum balance of the magnetic and electric loading. However, different approaches achieve different levels of performance.

1.3 General Description of IM Drives

Over a long period of time, the simple open loop volt/hertz (v/f) control method has been popularly used in low performance drives [6]. In scalar control schemes the phase relations between IM space vectors are not controlled during transient times. A small drift in speed and air-gap flux due to fluctuation in load torque and supply voltage, as well as sluggish transient response, are some of the problems associated with this scheme. In a majority of industrial applications, these drawbacks are of no consequence, but still unacceptable for high-performance drive applications which require fast and accurate speed tracking response, and quick recovery of speed from any disturbances.

In order to overcome these drawbacks, the concept of field orientation was introduced by Blaschke [7]. Blaschke examined how field orientation occurs naturally in a separately excited DC motor. The armature flux and the field flux are always perpendicular to each other due to the effect of the compensating winding. In an induction machine, a similar condition can be created by the decomposition of the stator current into two components, flux-producing current and torque-producing current, in the rotating reference frame. Thus, the control of AC motors becomes a close correspondence to DC machines while maintaining its general advantage over DC machine. Field oriented control (FOC) has gained widespread acceptance as a high-performance control strategy for IM drives [8-9]. The FOC method requires high computational power of microcontrollers. With the evolution of fast microprocessors and Digital Signal Processors (DSPs), implementation of FOC in real-time has been achieved and new nonlinear control methods have been developed during the past 10 years, such as the feedback linearization, passivity-based, and backstepping designs. There methods are generally called nonlinear control schemes. [10-12].

The feedback linearization control (FLC) consists of two steps. In the first step, a nonlinear compensation which cancels the nonlinearities included in the IM is implemented as an inner feedback loop. In the second step, a controller which ensures stability and some predefined performance is designed based on conventional linear theory, and this linear controller is implemented as an outer feedback loop [13].

In contrast to the feedback linearization, which results from a purely mathematical approach, the passivity-based control has evolved from consideration of physical properties such as energy saving and passivity [14]. The main idea of passivity-based design is to reshape the energy of the IM in such a way that the required asymptotic output tracking properties will be achieved.

Lastly, backstepping design is a relatively new technique for the control of IM [15]. The most appealing point is the use of virtual control variables to make the original high order system simpler and smaller. Thus the final control outputs can be derived step by step through suitable Lyapunov functions ensuring global stability. An adaptive robust nonlinear controller can be derived using this control method in a straightforward manner. More details about the backstepping design and application to the IM drive will be dealt with in the following chapters of this thesis.

1.4 Literature Review

1.4.1 Loss Minimization Control of IM Drives

The control strategy to improve motor efficiency can be divided into two categories: 1) loss-model-based controller (LMC), 2) search controller (SC).

1) Loss-Model-Based Controller: The model-based controller computes losses by using the machine model and selects a flux level that minimizes losses.

Various loss models for loss minimization of IM drive have been reported in the literature [16-25]. In the early works, the potentiality of loss minimization is addressed for the scalar drive using simple loss modeling in [16,17]. H.G.Kim et al. [18] suggested an optimal efficiency control algorithm for an induction motor supplied by a current source inverter. It was shown that any torque and speed pair can be obtained by many combinations of rotor frequency (or slip) and flux, each combination resulting in a different level of loss. The motor flux was reduced to decrease the total loss and to improve the power factor at light load. The required relationship between the stator current and the rotor frequency for the minimum loss was obtained numerically and a control loop had minor modifications to the constant flux control scheme. Kioskeridis and Margaris [19] calculated the total of iron loss,

copper losses and stray loss and derived LMC to determine the optimal flux level that minimizes the total loss of scalar controlled induction motor drive. P.Famouri and J.J. Cathey [20] derived the per-unit efficiency of the IM as function of slip, frequency and losses including the copper losses, core loss, rotational power loss, and power loss crossing the motor airgap. This equation was used to find the frequency that maximizes the efficiency at any torque-speed operating point. This method is the closed loop control technique with the improvement over the open loop volt/hertz (v/f) method. Lorenz and Yang [21] developed a method of optimally determining dynamic flux trajectories for closed-cycle operation of field oriented induction machines. Dynamic programming approach was used to minimize the copper and iron losses. They consider the copper and iron losses to formulate the loss model and defined an objective function that depends on the drive's loss. The limits on motor flux, speed, voltage and current were considered as constraints of the dynamic programming problem. Then, the optimal flux and the flux producing d-axis current trajectories over the cycle were obtained by solving the problem. A microcomputer implementation of the control system was also presented. Garcia et al. [22] derived a loss model consisting of resistors reflecting iron loss, rotor and stator copper losses as a function of stator current components, i_{ds} and i_{qs} in d-q frame. The IM equivalent circuit was simplified by deleting leakage inductance in the induction motor equivalent circuit. Based on this model, they developed a closed-form equation for the optimum flux level in the field-oriented frame. This algorithm allows the electromagnetic losses in a variable speed and torque IM drive to be decreased while keeping a good dynamic response. The efficiency sensitivity to parameter variations was also studied. Chakraborty and Hori [23] proposed the hybrid method combining the loss model approach and search approach together for the indirect vector-

controlled IM to extract the best of both. The first estimation is from the loss model approach and the subsequent adjustment of flux is through the search technique. Thus, the hybrid method improved both the speed and the capability of adaptation for a possible change in load or a variation in motor parameters. However, both the computation of loss model and measurement of input power have to be done in this method, and this makes overall control system complicated. The loss model developed in [22] was simplified even more by rearranging the iron loss resistance and utilized for the LMC part of the hybrid method to obtain the first estimate of the flux. Bernal et al [24] proposed a generalized d-q loss model for the different types of motors such as IM's, PMSM's, RM's or DC motors, showing that the structure of losses follows a similar template for all these machines. The loss model presented in [22] is used as the IM loss model again. S. Lim et al [25] developed a simplified loss model without sacrificing the leakage inductance. In the simplified model, the loss was represented as a resistance connected to a dependent voltage source. According to the simulation and experimental results, the loss calculation based on this simplified model was closer to that of full model than previous works.

2) Search Controller: On the other hand, SCs finds the optimum flux level based on the exact measurement of power input [26-31].

Moreira et al [26] used the information of third-harmonic components of the stator phase voltage to reduce the d-axis current. He also used the third harmonic signal to estimate the motor speed, as well as to decouple torque and flux producing components of the stator current. Sul and Park [27] proposed an efficiency maximizing technique by defining an optimal slip. The optimal slip is first searched by trial and error, and stored in the microprocessor memory. Then the controlled system is forced to track the optimal slip from the lookup table. This technique can be

considered as an indirect way to minimize the input power. Kirschen et al. [28] decreased the flux command in small steps until the minimum input power is achieved for the given torque and speed. This task is done by the speed control loop which adjusts the q-axis current to compensate the effect of changes in the rotor flux. This is a very simple and easy solution, but the problem is the long search time for the convergence. It took about 30 seconds for the controller to bring the motor to the minimal loss operating condition when the motor was operating at the rated flux condition. The long search time was necessary because the flux was reduced in several small steps in order not to cause undesirable speed disturbances produced by large changes in the rotor flux. Even with small step time, the torque pulsation was unavoidable. Sousa et al. [29] proposed a fuzzy-logic-based controller to improve the work of Kirschen et at [28]. They adaptively reduced the reference flux producing current with adaptive step size to speed up the convergence. As the motor flux approached the optimum value, a Fuzzy controller reduced the step size of change. The torque pulsation problem is taken care of by applying feed-forward compensation. However, the iron loss and parameter deviation were not considered in compensation. Kim et al. [30] designed a controller aiming at both high efficiency and high dynamic performance. They adjusted the squared rotor flux according to a minimum power algorithm based on the Fibonacci search method. The torque ripple is not generated in this configuration, since the speed and rotor flux are decoupled by means of nonlinear control. The nonlinear controller requires the accurate value of the rotor resistance to calculate the accurate rotor flux. This value was obtained by an online identification algorithm. The experimental results showed the shorter search time with larger flux steps as compared to that in [28], while no undesirable disturbances appear in the motor torque and speed. However, these improvements on system performance have

added sufficient complexity in overall control algorithm. Ta and Hori [31] improved the convergence by adopting the golden-section-based search algorithm. However, major problems exist in selecting the upper and lower limits of the flux-producing current before the algorithm starts. To achieve an acceptable dynamic performance and to increase the speed of search, a priori knowledge of the drive system is necessary.

1.4.2 Adaptive Backstepping Controller for IM

Various nonlinear control methodologies have been applied to the control of IM. The adaptive backstepping method has been gaining popularity in design of speed controllers for DC, induction and permanent magnet motors in recent years [32,33]. This technique allows the designer to incorporate most system non-linearities and uncertainties in the design of the controller, which is the important advantage over other nonlinear control methods such as feedback linearization. Tan and Chang [15,34] combined the adaptive backstepping approach with field orientation for the IM drive. The field orientation transformation brings significant simplification to the IM model so that backstepping design technique can be applied more easily. The designed nonlinear controller successfully achieved rotor angular speed and rotor flux amplitude tracking objectives with uncertainties in the rotor resistance and load torque. H. Tan et.al [35] utilized the adaptive backstepping technique for position control of IM system. They first derived a simplified linear small signal model for the IM system via the field orientation principle and developed an adaptive backstepping controller free of singularity or overparameterization under uncertainties of inertia, friction, and load torque which are the major concerns in the motion control applications. The simulation results showed the successful position tracking. Huang

and Fu [36] proposed an adaptive backstepping controller for linear induction motor to achieve speed/position tracking. A nonlinear transformation was proposed to facilitate controller design. They also considered the end effect of the linear induction motor in their controller design. There have been attempts to combine the adaptive backstepping method with other control techniques. Shieh and Shyu [37] combined the nonlinear sliding-mode torque and flux control with adaptive backstepping approach. Based on the state-coordinates transformed model representing the torque and flux magnitude dynamics, the nonlinear sliding-mode control was designed to track a liner reference model. Then, the adaptive backstepping control approach was utilized to obtain the robustness for mismatched parameter uncertainties. In [38], the authors developed the adaptive sliding-mode backstepping motion controller for a mechanical system driven by an IM. They adopt the sliding mode torque control as the inner loop controller and then designed the position controller to generate the toque command using the backstepping method.

1.5 Problem Identification and Thesis Objective

As discussed in the literature review, LMC computes losses by using the machine model and selects a flux level that minimizes the losses. Thus, the LMC offers advantages of fast response and no torque ripple as compared to the search controller.

However, one of the weaknesses of LMC is that the accuracy depends on the extent of correct modeling of the motor drive and the losses. In the development of the loss model, there is always a tradeoff between accuracy and complexity. To find the loss expression from the full loss model is a very complex job and an attempt to make it simple will sacrifice the accuracy. In the loss model used in the previous works [22-24], the leakage inductance is neglected in order to simplify the induction

motor equivalent circuit. S.Lim et al [25] developed a simplified loss model without sacrificing the leakage inductance, but the developed expression for an optimum flux level has a different format from the one in [22]. As a result, it is impossible for that expression to be used for the generalized model in [24] for the different types of motors such as IM's, PMSM's, RM's and DC motors.

Another weakness of the LMC is that its performance is dependent on the knowledge of motor parameters. Even if the modeling of losses is done sufficiently rigorously, LMC cannot find the optimum flux level when the accurate motor parameters are unknown, and its performance deteriorates when parameters change. Online estimation of the parameters can be a solution for this issue, but it can make the overall loss minimization scheme far more complicated. In the loss model used in the previous works [22-25] all parameters are considered constant. Therefore, when the parameters, especially rotor resistance changes, the exact loss minimization cannot be achieved.

Other than the loss issue, in the previous works [32-34] adaptive backstepping based controllers were designed without considering the iron loss. It is well known that neglecting the iron loss in an induction motor model causes performance deterioration. In rotor-flux-oriented vector control, which is by far the most popular technique for vector control due to simplicity, rotor flux is often estimated because its measurement is almost impossible in practice. Ignoring iron loss in an induction motor model causes errors in the calculation of rotor flux (or the equivalent value), slip and torque and these errors eventually result in performance deterioration [39-41]. To investigate and cope with this problem, there has been much research in the PI based vector control of an IM [42-44]. However, little work has been done in the area of nonlinear control of an IM. This is mainly because the extra state variables in the

motor model have to be introduced in order to explain the current flowing through an iron loss resistor, and this makes the derivation of the nonlinear controller much more complicated.

This work is directed to develop and implement an adaptive backstepping based LMC for IM drive which can achieve both high performance and minimum motor loss.

The first objective is to develop a new loss model and LMA to determine an optimum flux level. The ideal loss model will be an accurate and simple one. In this work, an IM model in d-q coordinates is referenced to the rotor magnetizing current and then an iron loss resistance is added in parallel to the magnetizing inductance. This transformation leads to no leakage inductance to consider on the rotor side. This decomposition feature into d-q components in the steady state motor model enables us to derive the equation to find an optimum flux level in the same fashion as the one in [22], which is widely used for the development of the LMA. However, in this work leakage inductance is not neglected. Furthermore, since the equation for the optimum flux has the same format as in the previous work, by simply redefining the motor parameters referenced to the magnetizing current, it can be applied to the existing loss minimization schemes without any modification

The second objective of this work is to develop an adaptive-backstepping-based nonlinear controller (ABNC) incorporating iron loss under the parameter uncertainties of rotor resistance and load torque in order to achieve high dynamic performance and to combine with a loss minimization scheme. The choice of the ABNC as speed controller with proposed LMC gives the following advantages:

- Firstly, the controller incorporating an iron loss can be systematically designed on exactly the same motor model as the loss expression is developed. In this

model, no extra state variables are added while iron loss is considered. Therefore, an ABNC incorporating iron loss can be designed without much more complexity as compared to the one with neglected iron loss.

- Secondly, by utilizing the important feature of the adaptive backstepping design method that a parameter update law can be obtained simultaneously with a control law, the online estimation of parameters for LMC can be achieved without extra effort.

The last objective of this work is the simulation and real time implementation of closed loop vector control of the proposed IM drive system. The simulation study is performed using Simulink/Matlab [45]. The real-time implementation is carried out using a DSP controller board, DS-1104 for an available laboratory 1/3 hp motor [46]. The dynamic performance of the proposed nonlinear controller and parameter adaptation features are examined and the effectiveness of the LMA is also demonstrated through a wide range of speed region including the field weakening region.

1.6 Thesis Organization

The organization of the remaining chapters of this thesis is as follows. Chapter 2 explains the basic concept of field oriented control (FOC) and necessary coordinate transformations for it. The derivation of the mathematical IM model incorporating iron loss is explained as well. Here it is shown that the FOC technique and referencing the IM model to rotor magnetizing current greatly simplify the mathematical model of IM. Chapter 3 explains losses which are involved in IM drive and the practical methods of loss reduction in IM drive and the new LMC is derived based on the motor model from chapter 2. Chapter 4 explains the adaptive backstepping technique

and shows step-by-step procedures for ABNC and parameter adaptation design in detail. Stability analysis is also presented. Chapter 5 describes the complete drive system combining the new LMC and ABNC. Extensive simulation results regarding both controller dynamics and loss minimization aspects of the total drive system are presented. Chapter 6 describes the real-time implementation of the proposed drive system of IM. The complete drive is implemented in real-time using a DS1104 DSP board on a laboratory 1/3 hp induction motor. The detailed real-time implementation procedures for both hardware and software are provided in this chapter. Various experimental results of the proposed scheme and discussion are presented. Finally, chapter 7 presents a summary of the contributions of this work, future scope of this work, and the conclusions. After that all pertinent references and appendices are listed.

Chapter 2

Mathematical Model of IM

This chapter explains the concept of the field oriented control of IM and the necessary coordinate transformations to apply it to an IM drive. The mathematical model of IM incorporating the iron loss is also derived in the d-q rotating reference frame using the coordinate transformations explained.

2.1 Field Oriented Control (FOC)

In a separately excited DC machine, the field current and the armature current flow in separate winding. Therefore, they can be controlled independently. Usually, particularly under high-load conditions, the flux is kept constant at the rated level within the speed range of zero to the rated value.

The objective of field oriented control (FOC), also called vector control, is to control an AC induction motor like a separately excited DC motor, thus obtaining the following DC machine advantages: instantaneous control of the separate quantities allowing accurate transient and steady state management. In rotor-flux-oriented control, in order to separate the stator currents of the induction machine into flux-and torque-producing components, the reference frame speed ω_e is chosen to be the instantaneous speed of the rotor flux space vector and locking its phase such that the

rotor flux space vector is aligned with the *d*–axis (equivalent to the flux or magnetizing axis). This means the q-axis component of the rotor flux is always zero and the d-axis component of the rotor flux is a constant value. Then, the torque expression in the d-q reference becomes:

$$T_d \propto \psi_{rd} i_{sq}$$

Because the amplitude of the rotor flux, ψ_{rd} is fixed value we have a linear relationship between torque and torque component, i_{sq}. Thus, the torque can be controlled by controlling the toque component of the stator current vector.

2.2 Coordinate Transformations

The IM model used for FOC design can be obtained by using the space vector theory [8] The 3-phase motor quantities (such as voltage, currents, magnetic flux, etc.) are expressed in terms of complex space vectors. With regard to the current, assuming that i_a, i_b, and i_c are the instantaneous balanced 3-phase stator currents,

$$i_a + i_b + i_c = 0$$

The stator current space vector can then be defined as follows:

$$i_s = k(i_a + \alpha i_b + \alpha^2 i_c)$$

where α is the spatial operators $e^{j2\pi/3}$ and k is the transformation constant, which is chosen as k=2/3. Figure 2.1 shows the stator current space vector and its components. This current space vector depicts the three phase sinusoidal system. It still needs to be transformed into a two time invariant co-ordinate system. This transformation can be divided into two steps:

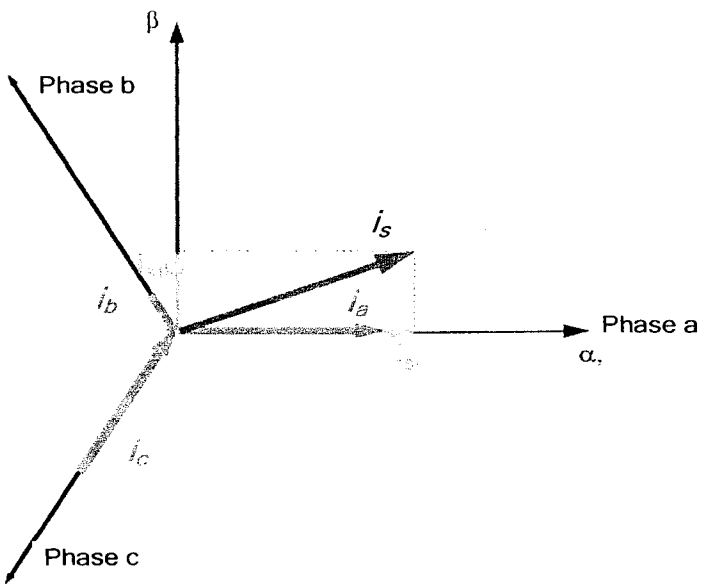

Fig.2.1: Stator current space vector and its components in α and β axis at certain instant.

- Clarke's transformation: (abc) to ($\alpha\beta$) of a two co-ordinate time variant system
- Park's transformation: ($\alpha\beta$) to (dq) of a two co-ordinate time invariant system

2.2.1 Clarke's Transformation

Complex space vectors can be described using only two orthogonal axes called (α, β). The utilization of the two-axis theory reduces the number of equations and simplifies the control design. With regard to the stator current, the real part of the space vector is equal to the instantaneous value of the direct-axis stator current component, $i_{s\alpha}$ and whose imaginary part is equal to the quadrature-axis stator current component, $i_{s\beta}$. Thus, the stator current space vector in the stationary reference frame attached to the stator can be expressed as:

$$i_s = i_{s\alpha} + j i_{s\beta}$$

The abc phase quantities can be directly transformed into the stationary $\alpha\beta 0$ axis quantities using the following equation:

$$\begin{bmatrix} x_\alpha \\ x_\beta \\ x_0 \end{bmatrix} = \frac{2}{3}\begin{bmatrix} \cos(\theta_r(0)) & \cos(\theta_r(0)-\frac{2\pi}{3}) & \cos(\theta_r(0)+\frac{2\pi}{3}) \\ \sin(-\theta_r(0)) & \sin(-\theta_r(0)+\frac{2\pi}{3}) & \sin(-\theta_r(0)-\frac{2\pi}{3}) \\ \frac{1}{2} & \frac{1}{2} & \frac{1}{2} \end{bmatrix}\begin{bmatrix} x_a \\ x_b \\ x_c \end{bmatrix} \tag{2.1}$$

where $\theta_r(0)$ is the angle of α -axis in respect to a-phase axis. The corresponding inverse relation is given by:

$$\begin{bmatrix} x_a \\ x_b \\ x_c \end{bmatrix} = \begin{bmatrix} \cos(\theta_r(0)) & \sin(-\theta_r(0)) & \frac{1}{2} \\ \cos(\theta_r(0)-\frac{2\pi}{3}) & \sin(-\theta_r(0)+\frac{2\pi}{3}) & \frac{1}{2} \\ \cos(\theta_r(0)+\frac{2\pi}{3}) & \sin(-\theta_r(0)-\frac{2\pi}{3}) & \frac{1}{2} \end{bmatrix}\begin{bmatrix} x_\alpha \\ x_\beta \\ x_0 \end{bmatrix} \tag{2.2}$$

For a balanced 3-phase system, x_0 does not exit. If $\theta_r(0)$ is set to 0 so that the α -axis coincides with the a-phase as depicted in Fig.2.1, the equation for this transformation can be written as:

$$\begin{bmatrix} x_\alpha \\ x_\beta \end{bmatrix} = \begin{bmatrix} \frac{2}{3} & -\frac{1}{3} & -\frac{1}{3} \\ 0 & \frac{1}{\sqrt{3}} & -\frac{1}{\sqrt{3}} \end{bmatrix}\begin{bmatrix} x_a \\ x_b \\ x_c \end{bmatrix} \tag{2.3}$$

and inverse relation is

$$\begin{bmatrix} x_a \\ x_b \\ x_c \end{bmatrix} = \begin{bmatrix} 1 & 0 \\ -\frac{1}{2} & \frac{\sqrt{3}}{2} \\ -\frac{1}{2} & -\frac{\sqrt{3}}{2} \end{bmatrix}\begin{bmatrix} x_\alpha \\ x_\beta \end{bmatrix} \tag{2.4}$$

The rotor position angle is defined as:

$$\theta_r = \int_0^t \omega_r(t)dt + \theta_r(0) \tag{2.5}$$

where ω_r is electrical rotor angle which is mechanical rotor speed ω_m times the number of pole pairs Z_P. Then, the rotor flux angle is defined as

$$\theta_e = \theta_r + \theta_{sl} \tag{2.6}$$

where θ_{sl} is the slip angle. The angular definitions are depicted in Fig.2.2

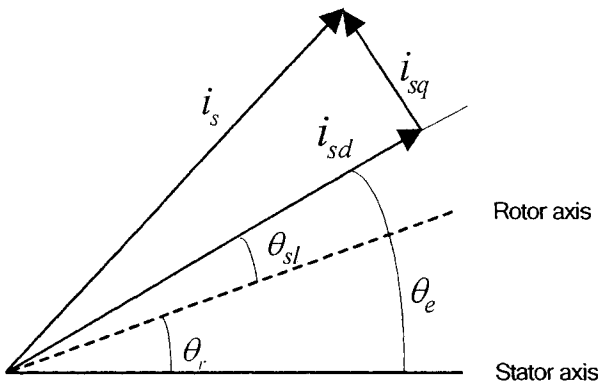

Fig.2.2: Rotor field angle definition

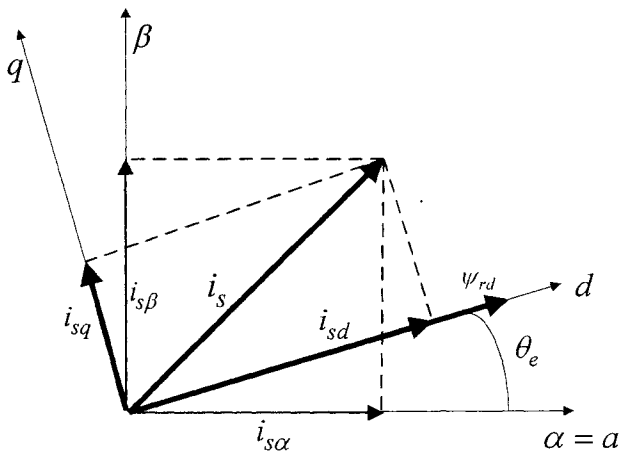

Fig.2.3: Stator current space vector and its components in the d,q rotating reference frame.

2.2.2 Park's Transformation

In the new frame (α,β), the expression of the torque is still dependent on the position of the rotor flux, preventing any easy solution of the electrical differential equation. To remove this dependency, the electrical equations are projected in a 2-phase (d,q) system that rotates at the speed of the electrical speed of the rotor and where the d axis is aligned with electrical position of the rotor flux. In this frame, the electrical expression of the torque becomes independent from θ_e. Figure 2.3 shows the relative position of the stationary and rotating d-q axes and how the stator current

space vector can be decoupled in the rotating reference frame. The equations corresponding to this transformation are given by:

$$\begin{bmatrix} x_d \\ x_q \end{bmatrix} = \begin{bmatrix} \cos\theta_e & \sin\theta_e \\ -\sin\theta_e & \cos\theta_e \end{bmatrix} \begin{bmatrix} x_\alpha \\ x_\beta \end{bmatrix} \tag{2.7}$$

The inverse relation is:

$$\begin{bmatrix} x_\alpha \\ x_\beta \end{bmatrix} = \begin{bmatrix} \cos\theta_e & -\sin\theta_e \\ \sin\theta_e & \cos\theta_e \end{bmatrix} \begin{bmatrix} x_d \\ x_q \end{bmatrix} \tag{2.8}$$

2.3 Induction Motor Model

Using complex space vectors as defined in Chapter 2.2 the dynamics for the motor in a rotating reference frame is given by:

$$u_s = R_s i_s + p\psi_s + j\omega_e \psi_s \tag{2.9}$$

$$0 = R_r i_r + p\psi_r + j(\omega_e - \omega_r)\psi_r \tag{2.10}$$

where u_s, R_s and R_r are the stator voltage space vector, resistances of the stator and rotor windings respectively. p is the differential operator d/dt, $\omega_e = d\theta_e / dt$ is the electrical angular speed of the rotor flux and $\omega_r = d\theta_r / dt$ is the electrical rotor speed. The flux linkages space vector for the stator and rotor are defined by:

$$\psi_s = L_s i_s + L_m i_r = L_{ls} i_s + L_m i_m \tag{2.11}$$

$$\psi_r = L_r i_r + L_m i_s = L_{lr} i_r + L_m i_m \tag{2.12}$$

where

$$L_s = L_{ls} + L_m$$

$$L_r = L_{lr} + L_m$$

$$i_m = i_s + i_r$$

Incorporating (2.11) and (2.12) into (2.9) and (2.10) yields

$$u_s = R_s i_s + L_s p i_s + j\omega_e L_s i_s + L_m p i_r + j\omega_e L_m i_r \tag{2.13}$$

$$0 = R_r i_r + L_r p i_r + L_m p i_s + j(\omega_e - \omega_r) L_r i_r + j(\omega_e - \omega_r) L_m i_s \tag{2.14}$$

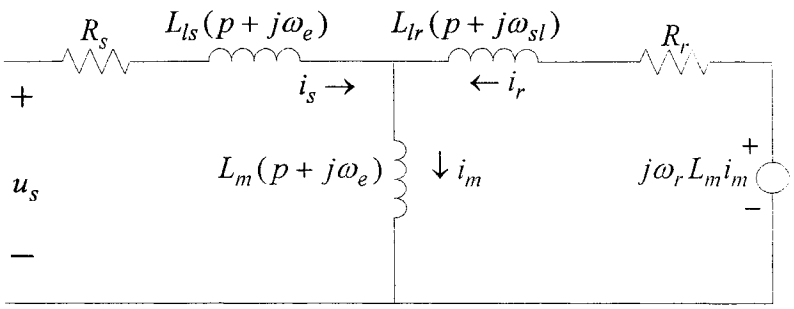

Fig.2.4: Dynamic equivalent circuit of induction motor

The equivalent circuit of an IM is shown in Fig.2.4.

2.3.1 IM Model referenced to Rotor Magnetizing Current

An equivalent circuit for IM can be expressed in a number of ways by the different choices of a flux linkage constant ρ in

$$i_m = i_s + \frac{i_r}{\rho} \tag{2.15}$$

The motor dynamics in (2.9)-(2.12) are the specific case of $\rho = 1$ (that is, $i_m = i_s + i_r$). With the choice of $\rho = L_m / L_r$, the rotor current can be rewritten as:

$$i_r = -\frac{L_m}{L_r}(i_s - i_m) \tag{2.16}$$

Substituting (2.16) into (2.13) and (2.14), and the straight forward calculations result in the following space vector motor model referenced to the rotor magnetizing current in a rotating reference frame.

$$u_s = R_s i_s + L'_s p i_s + j\omega_e L'_s i_s + L'_m p i_m + j\omega_e L'_m i_m \tag{2.17}$$

$$0 = R'_r(i_s - i_m) - L'_m p i_m - j(\omega_e - \omega_r) L'_m i_m \tag{2.18}$$

where the parameter L'_s, L'_m and R'_r are defined as:

$$L'_s = L_s(1 - \frac{L_m^2}{L_s L_r}) = L_s \sigma \tag{2.19}$$

$$L'_m = \frac{L_m^2}{L_r} \tag{2.20}$$

$$R'_r = R_r \frac{L_m^2}{L_r^2} \tag{2.21}$$

and the flux linkages for the stator and rotor can also be redefined as:

$$\psi'_r = L'_m i_m \tag{2.22}$$

$$\psi'_s = L'_s i_s + L'_m i_m \tag{2.23}$$

The notation for this transformation is illustrated in Fig.2.5 and the space vector equivalent circuit is shown in Fig.2.6. With the projection of space vectors into d-q axes ($u_s = u_{sd} + ju_{sq}$, $i_s = i_{sd} + ji_{sq}$ and $i_m = i_{md} + ji_{mq}$) and $i_{mq} = 0$, $i_{md} = i_{mr}$ =*constant* for the rotor flux oriented control scheme, (2.17) and (2.18) can be expressed as:

$$u_{sd} = R_s i_{sd} + L'_s p i_{sd} - \omega_e L'_s i_{sq} + L'_m p i_{mr} \tag{2.24}$$

$$u_{sq} = R_s i_{sq} + L'_s p i_{sq} + \omega_e L'_s i_{sd} + \omega_e L'_m i_{mr} \tag{2.25}$$

$$i_{mr} = \frac{1}{1 + \frac{L'_m}{R'_r} p} i_{sd} \tag{2.26}$$

$$\omega_{sl} = \frac{R'_r}{L'_m} \frac{i_{sq}}{i_{mr}} \tag{2.27}$$

The electro-mechanical dynamic equation is given by:

$$J \frac{d\omega_m}{dt} = T_e - T_l - B_m \omega_m \tag{2.28}$$

where J is the moment of inertia, T_l is the load torque and B_m is the friction damping coefficient and assumed to be zero in this work.

The developed torque, T_e is expressed by:

$$T_e = \frac{3}{2} Z_p L'_m i_{mr} i_{sq} = \frac{3 Z_P (L'_m i_{mr})^2}{2 R'_r} \omega_{sl} \tag{2.29}$$

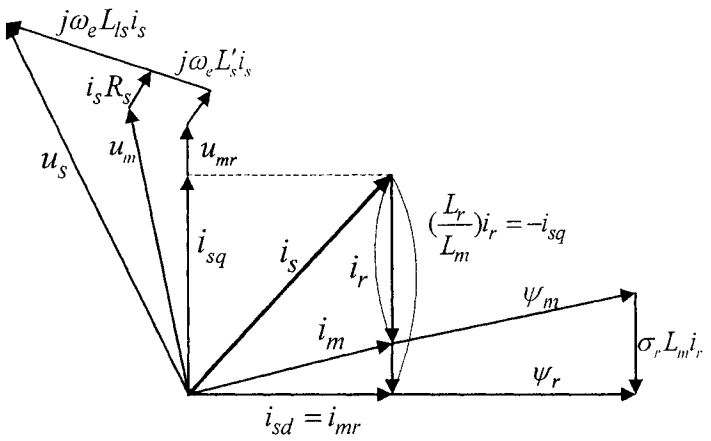

Fig.2.5: Phasor diagram of steady-state equivalent circuits of an induction motor

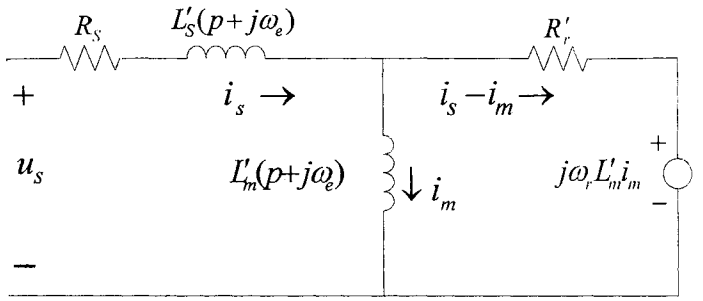

Fig.2.6: Space vector equivalent circuit in a rotor flux oriented reference frame

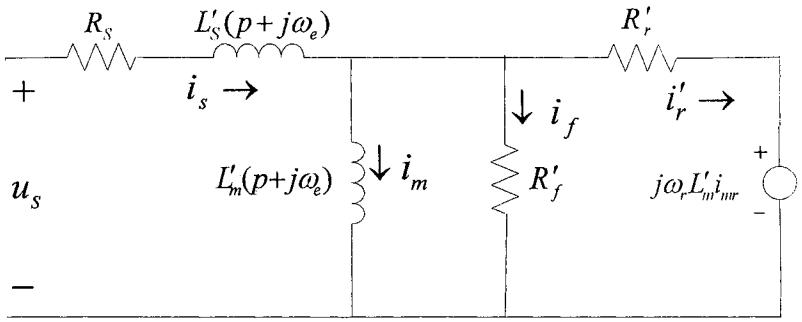

Fig.2.7: Space vector equivalent circuit of an induction motor including an iron loss resistor.

2.3.2 Incorporation of Iron Loss

In the IM model described in (2.24) to (2.29), the iron loss is not taken into account. It is well known from the literature that the neglect of the iron loss in the design of a vector controller causes detuning problem and results in performance deterioration [39-41].

The iron loss is modeled by adding the iron loss resistance R'_f in parallel to the magnetizing inductance as shown in Fig.2.7. With the addition of R'_f to the IM model, the stator voltage equation (2.17) is unchanged compared to the model without the iron loss resistance. However, there is extra current flowing through the iron loss resistance and this extra current has to be considered in the motor equation. From Fig.2.7, the current through the iron loss resistance can be expressed as:

$$i_f = \frac{L'_m}{R'_f}(p + j\omega_e)i_{mr} \tag{2.30}$$

Then, the following equations are obtained using the space vector:

$$u_s = R_s i_s + L'_s p i_s + j\omega_e L'_s i_s + L'_m p i_m + j\omega_e L'_m i_m \tag{2.31}$$

$$i_s = i_m + i_f + i'_r = i_m + \frac{L'_m}{R'_f}(p + j\omega_e)i_m + \frac{L'_m}{R'_r}(p + j(\omega_e - \omega_r))i_m \tag{2.32}$$

Using $u_s = u_{sd} + ju_{sq}$, $i_s = i_{sd} + ji_{sq}$, $i_m = i_{md} + ji_{mq}$ and $i_{mq} = 0$, $i_{md} = constant$ for the rotor flux orientation control scheme, we obtain from (2.31) and (2.32) that

$$u_{sd} = R_s i_{sd} + L'_s p i_{sd} - \omega_e L'_s i_{sq} + L'_m p i_{md} \tag{2.33}$$

$$u_{sq} = R_s i_{sq} + L'_s p i_{sq} + \omega_e L'_s i_{sd} + \omega_e L'_m i_{md} \tag{2.34}$$

$$i_{sd} = i_{md} + (\frac{L'_m}{R'_f} + \frac{L'_m}{R'_r})p i_{md} \tag{2.35}$$

$$i_{sq} = \omega_e \frac{L'_m}{R'_f} i_{md} + (\omega_e - \omega_r)\frac{L'_m}{R'_r} i_{md} \tag{2.36}$$

Defining R_t as parallel sum of R_r' and R_f' (that is, $R_t = R_r' \| R_f'$) and $i_{mr} = i_{md}$, from (2.35) the magnetizing current can be expressed by

$$i_{mr} = \frac{1}{1+(\frac{L_m'}{R_r'}+\frac{L_m'}{R_f'})p} i_{sd} = \frac{1}{1+\frac{L_m'}{R_t}p} i_{sd} \tag{2.37}$$

From (2.36), slip speed can be derived as

$$\omega_{sl} = \frac{R_r'}{L_m'}\frac{i_{sq}}{i_{mr}} - \omega_e \frac{R_r'}{R_f'} = \frac{R_t}{L_m'}\frac{i_{sq}}{i_{mr}} - \omega_r \frac{R_t}{R_f'} \tag{2.38}$$

From (2.38), the developed torque can be written

$$T_e = \frac{3}{2} Z_p \frac{(L_m' i_{mr})^2}{R_r'} \omega_{sl} = k_e i_{mr} i_{sq} - k_e \omega_e \frac{L_m'}{R_f'} i_{mr}^2 \tag{2.39}$$

where $k_e = \frac{3}{2} Z_p L_m'$

Ignoring R_f', which means $R_f' = \infty$, in (2.37), (2.38) and (2.39) will cause errors in the calculation of the load magnetizing current, slip and torque. Incorporating (2.35) and (2.36) into (2.33) and (2.34) respectively, we have a final set of motor dynamic expressions including a mechanical equation.

$$p i_{sd} = -\frac{R_s}{L_s'} i_{sd} + \omega_e i_{sq} - \frac{R_t}{L_s'} i_{sd} + \frac{R_t}{L_s'} i_{mr} + \frac{1}{L_s'} u_{sd} \tag{2.40}$$

$$p i_{sq} = -\frac{R_s}{L_s'} i_{sq} - \omega_e i_{sd} - \frac{R_t}{L_s'} i_{sq} - \omega_r (1 - \frac{R_t}{R_f'}) \frac{L_m'}{L_s'} i_{mr} + \frac{1}{L_s'} u_{sq} \tag{2.41}$$

$$p i_{mr} = \frac{R_t}{L_m'} (i_{sd} - i_{mr}) \tag{2.42}$$

$$p\omega_m = \mu i_{mr} i_{sq} - \mu \omega_e \frac{L_m'}{R_f'} i_{mr}^2 - \frac{T_l}{J} \tag{2.43}$$

where J is the rotor inertia constant and $\mu = \frac{3}{2} Z_p \frac{L_m'}{J}$

Note that R_r' in equations (2.24)-(2.29) have been replaced with R_t and no extra state variables are added while the iron loss is incorporated in the equations. This set

of equations will be used in the rest of this thesis. From observing the structural property of equations (2.40) to (2.43) we can find out that there are two second-order subsystems in the induction motor model. The first subsystem is (2.41) and (2.43), and the second subsystem is (2.40) and (2.42). The first subsystem consists of two state variables of ω_m and i_{sq}, and is controlled by u_{sq} while the second subsystem consists of i_{mr} and i_{sd}, and is controlled by u_{sd}. This division into d and q components in motor equation coincides with the principle of FOC as explained earlier. Although there exists the coupling among the state variables in (2.43), the backstepping technique can still be applied in the design of a controller incorporating the iron loss.

2.4 Concluding Remarks

In this chapter, the principle of the field oriented control (FOC) of IM is explained. The coordinate transformation from abc to dq in order to implement the FOC and the space vector representation of IM are also explained in detail. Utilizing these concepts, the mathematical model of IM incorporating the iron loss has been derived in the d-q rotating reference frame. The derived IM model has incorporated the iron loss while no extra state variables are added. This mathematical model will be used in the design and development of LMA and ABNC in the following chapters.

Chapter 3

Loss Minimization Control of IM Drives

In this chapter, we classify the types of losses involved in IM drives and review the different methods of loss reduction with the focus on the control technique based method. A new loss minimization control strategy for an adjustable speed/torque IM drive is also presented.

3.1 Methods of Loss Reduction

Operation of an IM is very efficient at or near rated conditions. However, in cases of applications which require adjustable torque and/or speed, especially operation at light load with rated flux, IM operates at very low efficiency. Considering the typical IM drive configuration as shown in Fig.3.1 consisting of a three-phase diode rectifier, IGBT inverter and squirrel-cage induction motor, IM drive losses can be divided into grid loss, converter loss, motor loss and transmission loss [2]. The brief description of these losses is as follows:

- Grid loss is caused by harmonic contents in input current.
- Converter loss mainly consists of switching and conduction losses from the inverter, rectifier loss, and harmonic motor loss which is caused by current ripples

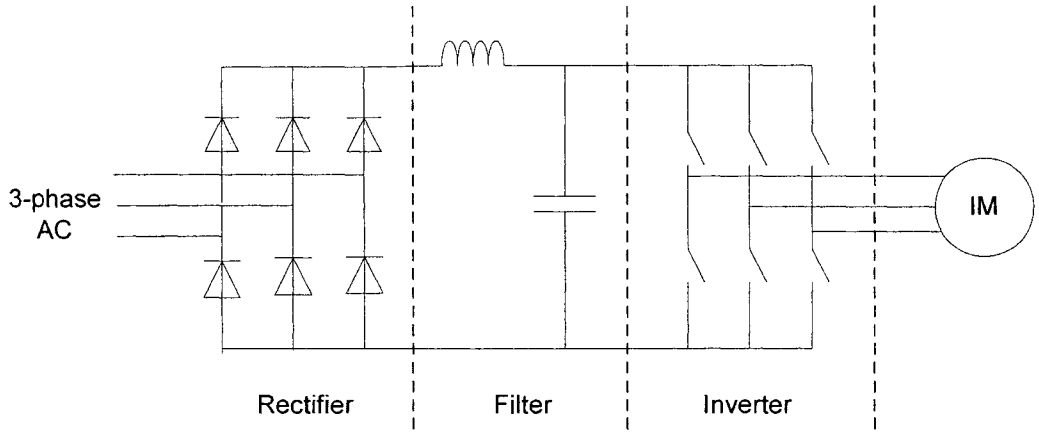

Fig.3.1: Typical IM drive configuration

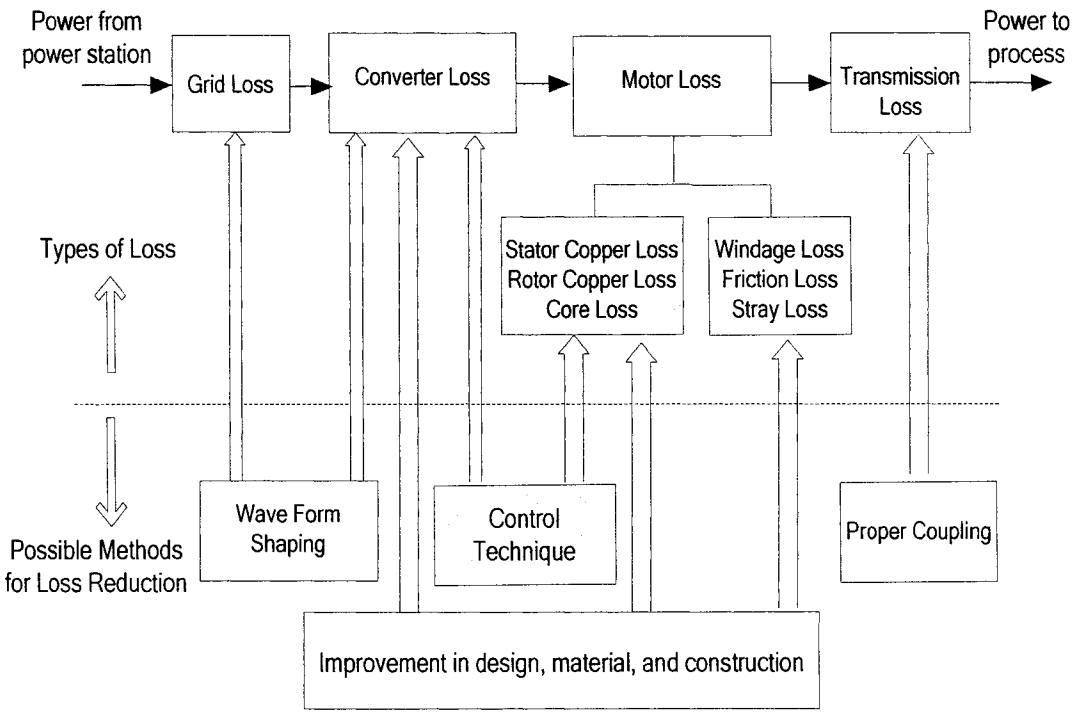

Fig.3.2: Different types of losses in IM drives and possible methods for loss reduction

from the pulse width modulated (PWM) converter. Converter loss is also decided by the modulation strategy, but this matter is not discussed in this thesis.

- Transmission loss could come from the bad coupling of the load. Generally, belt type coupling has poorer performance than a direct shaft coupling.
- The motor loss constitutes stator and rotor copper losses, core loss, mechanical (friction and windage) losses, and stray load loss [47]. Core and copper losses dominate the overall motor loss (about 80%) compared to stray, friction and windage, and they depend on the magnetic and electric loading of the machine and therefore controllable. The stray loss depends mainly on the construction of the motor and also on the harmonics in the supply voltage.

Among these losses, converter loss and especially motor loss are dependent on flux levels. In the current work, stray, friction, windage losses and converter losses are neglected.

The reduction of loss can be achieved by different methods. Improvement in design, material, and fabrication of the motor and converter achieve the loss reduction. For example, for high efficiency motor, the use of more copper to reduce copper loss and the use of low hysteresis laminated steel to reduce core loss reduce the motor loss [48-49]. Improvement of voltage and current waveforms of the motor power supply reduces harmonic losses [50-51].

In this thesis, we consider a case where both high dynamic performance and optimum efficiency in a wide range of load and speed are needed. Therefore, among the many methods for efficiency optimization, this thesis focuses on developing a better control technique to reduce motor loss which is the dominant loss in IM drives. Figure 3.2 summarizes the different types of losses in IM drives and shows the possible methods for each loss reduction. Shaded blocks imply the focus in the thesis.

3.2 Loss Minimization by Control Techniques

3.2.1 Search Controller (SC)

The basic principle of the search controller is to measure the input power and then iteratively search for the flux level (or its equivalent variables) until the minimum input power is detected while keeping the output power of the motor constant. Because the motor output power cannot be measured in practice, the speed is kept constant and load torque is assumed to be constant during the optimization period. If power measurement is done at the input of the rectifier, converter losses are taken into account in search of minimum input power. However, a voltage sensor and a current sensor are required and it would be an expensive solution. In order to reduce the cost of measurement, the DC-link power can be measured. In this case, only one extra current sensor is required while the inverter loss is considered. The most cost-effective and easiest way is to minimize the stator current which does not require extra measuring devices. Because SC offers optimum efficiency based on the exact

	Advantages	Disadvantages
LMC	● Fast response ● No torque pulsations ● Simple to implement	● Requires the knowledge of motor and loss model ● Dependency on the parameter
SC	● No loss model necessary ● No dependency on the parameters ● Include the inverter losses (in some cases)	● Slow Convergence ● Torque pulsations ● Extra sensors for power measurement (in some cases)

Table3.1: Comparison of Loss Minimization Control Strategies

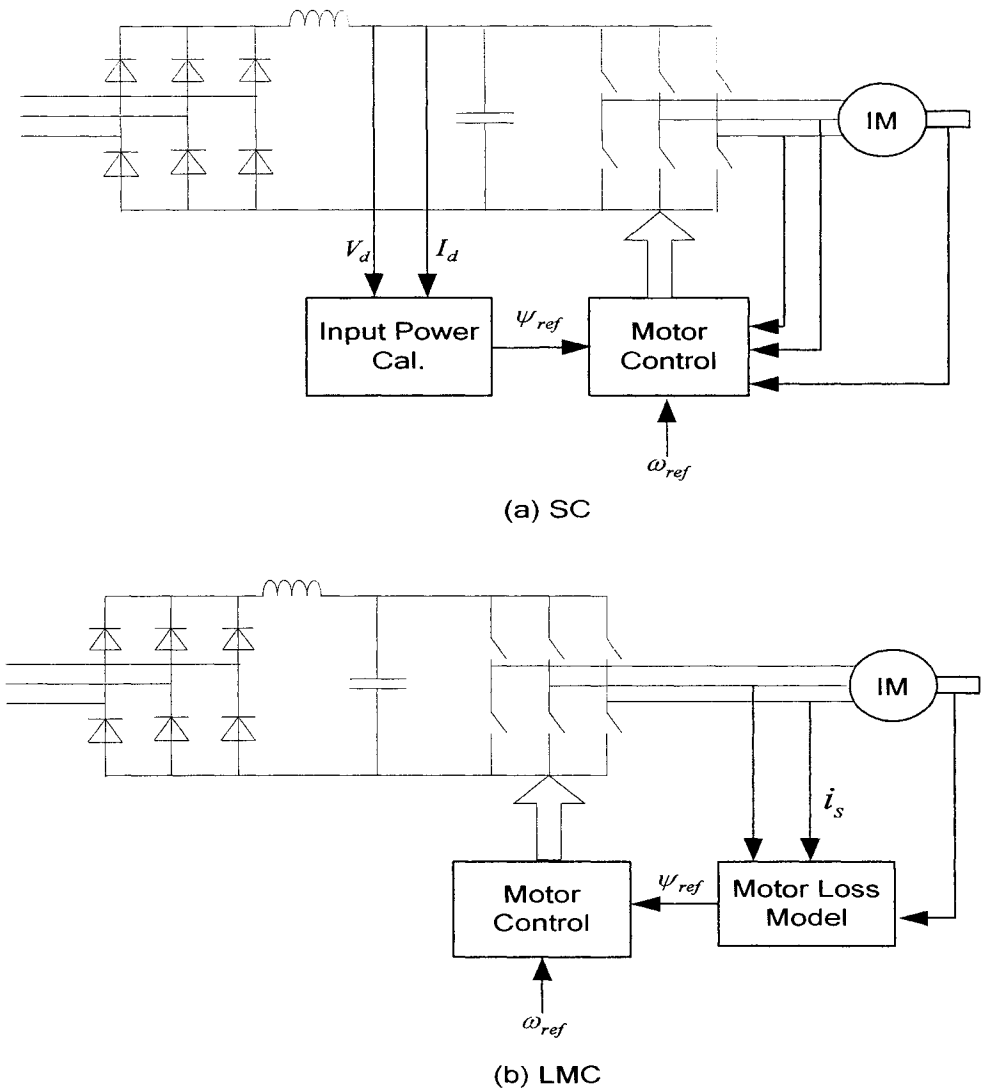

Fig.3.3: General schemes for SC and LMC

measurement of power input, it does not depend on the machine parameters. However, important drawbacks of the search controller are the slow convergence and torque ripples [26-31].

3.2.2 Loss Model based Controller (LMC)

LMC computes losses by using the machine model and solve a flux level that minimizes the losses [16-25]. The optimum flux level is determined based on a loss

model in various ways and the loss model chosen to implement is often determined by how the motor control is realized. In a vector control scheme, loss models are described in d-q coordinates. LMC is fast and does not produce torque ripple. However, the accuracy depends on the correct modeling of the motor drive and the losses, and its performance deteriorates when the parameter changes. The advantages and disadvantages of SC and LMC are summarized in Table 3.1. Schemes of SC and LMC are shown in Fig.3.3.

3.3 Proposed Loss Minimization Strategy

3.3.1 Loss Calculation

In the steady state of the motor model in Fig.2.7, there is no leakage inductance on the rotor side and the sum of the recalculated rotor current i_r' and the iron current i_f is perpendicular to the magnetizing current i_{mr}. Because of this, the circuit illustrates decomposition of the stator current i_s into the rotor flux-oriented components: $i_{sd} = i_{mr}$ which forms the flux ψ_r, and $i_{sq} = i_f + i_r'$ which is related to the control of torque developed by the motor. Note that i_f does not contribute to the developed torque and only i_r' controls the developed torque. From the motor model (2.40)-(2.43), the steady-state IM equivalent circuit in the d and q axis are shown in Fig.3.4.

In the development of the loss model, a typical method for model simplicity used in previous research [22-24] is to ignore the leakage inductance. The decomposition feature of the proposed motor model makes the derivation of the loss model more straightforward without any assumption for model simplicity. From Fig.3.4, the total

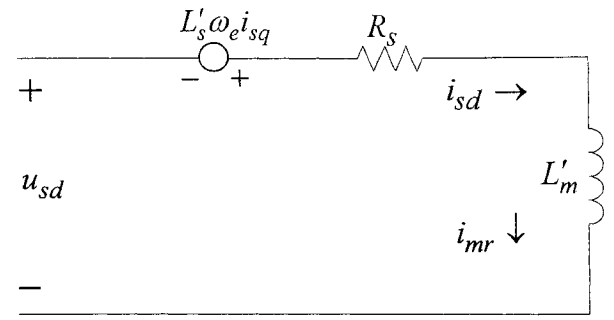

(a) d-axis equivalent circuit

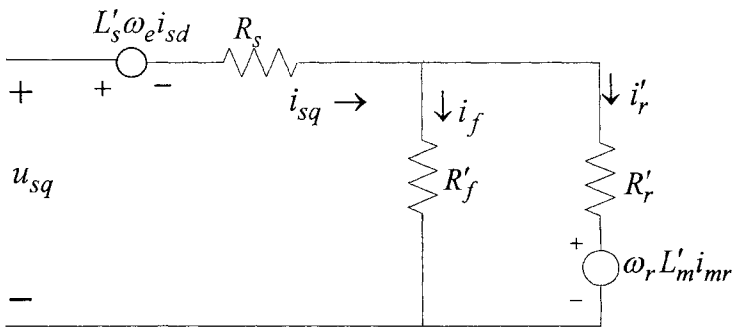

(b) q-axis equivalent circuit

Fig.3.4: Steady state IM equivalent circuit

losses are given by:

$$\begin{aligned} P_{total} &= P_{cus} + P_{iron} + P_{cur} \\ &= R_s(i_{sd}^2 + i_{sq}^2) + R'_f(i_{sq} - i'_r)^2 + R'_r i'^2_r \end{aligned} \tag{3.44}$$

where P_{cus} is stator copper losses, P_{iron} is iron losses and P_{cur} is rotor copper losses. Since only the stator voltage and the current are real state variables, we need to express the total losses in terms of i_{sd} and i_{sq}. From Fig.3.4, the rotor current can be expressed as:

$$i'_r = i_{sq} - i_f = i_{sq} - \frac{R'_r}{R'_f} i'_r - \omega_r \frac{L'_m}{R'_f} i_{sd} \tag{3.45}$$

Then,

$$i'_r = \frac{R'_f}{R'_f + R'_r} i_{sq} - \omega_r \frac{L'_m}{R'_f + R'_r} i_{sd} \tag{3.46}$$

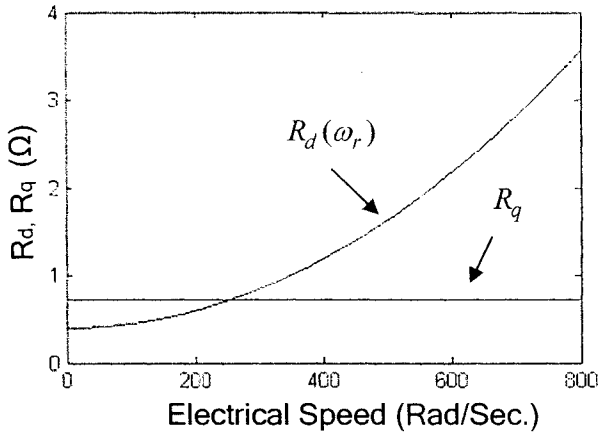

Fig.3.5: Plot of $R_d(\omega_r)$ and R_q against electrical speed

Substituting i_r' from (3.46) into (3.44) yields:

$$\begin{aligned} P_{total} &= P_{cus} + P_{iron} + P_{cur} \\ &= R_s(i_{sd}^2 + i_{sq}^2) + \frac{R_f'}{(R_f' + R_r')^2}(R_r'^2 i_{sq}^2 + L_m'^2 \omega_r^2 i_{sd}^2 + 2R_r' L_m' \omega_r i_{sq} i_{sd}) \\ &\quad + \frac{R_r'}{(R_f' + R_r')^2}(R_f'^2 i_{sq}^2 + L_m'^2 \omega_r^2 i_{sd}^2 - 2R_f' L_m' \omega_r i_{sq} i_{sd}) \qquad (3.47) \\ &= R_s(i_{sd}^2 + i_{sq}^2) + \frac{R_f' R_r'}{R_f' + R_r'} i_{sq}^2 + \frac{L_m'^2 \omega_r^2}{R_f' + R_r'} i_{sd}^2 \\ &= R_d(\omega_r) i_{sd}^2 + R_q i_{sq}^2 \end{aligned}$$

where $R_d(\omega_r) = R_s + \frac{L_m'^2}{R_f' + R_r'}\omega_r^2$ and $R_q = R_s + \frac{R_f' R_r'}{R_f' + R_r'}$

In (3.47), $R_d(\omega_r)$ and R_q are the d-q axes equivalent resistors representing the total loss. The total loss is a function of electrical rotor speed because $R_d(\omega_r)$ is dependent on ω_r. In low speed operation, core loss (hysteries and eddy current loss) is relatively low compared to copper losses. However, as the speed increases, the contribution of the eddy current loss increases and finally becomes a dominant portion of the total loss. Fig. 3.5 shows $R_d(\omega_r)$ and R_q values against electrical speed and explains this

fact. In Chapter 2, rotor flux is defined as: $\psi_r' = L_m' i_{mr}$ and in steady state $\psi_r' = L_m' i_{sd}$. Hence iron loss is caused by the d-axis stator current. $R_d(\omega_r)$ in Fig.3.5 is proportional to the square of ω_r. It motivates us to reduce the d-axis current (or equivalent values) for the loss minimization. However, too much decrease in i_{sd} will lead to extremely large i_{sq} for a desired torque production, resulting in a large copper loss. Therefore, a compromise between iron loss and copper loss has to be made for optimal operation.

3.3.2 Loss Minimization Algorithm

The developed electrical torque can be expressed in different ways. From Fig.3.4 and (3.46), we can express the torque as:

$$\begin{aligned} T_e &= \frac{3}{2} Z_p L_m' i_{mr} i_r' \\ &= \frac{3}{2} Z_p L_m' \left(\frac{R_f'}{R_f' + R_r'}\right) i_{sq} i_{mr} - \frac{3}{2} Z_p \omega_r \frac{(L_m' i_{mr})^2}{R_f' + R_r'} \end{aligned} \tag{3.48}$$

In Chapter 2, the slip and torque were expressed as follows:

$$\omega_{sl} = \frac{R_r'}{L_m'} \frac{i_{sq}}{i_{mr}} - \omega_e \frac{R_r'}{R_f'} = \frac{R_t}{L_m'} \frac{i_{sq}}{i_{mr}} - \omega_r \frac{R_t}{R_f'} \tag{3.49}$$

$$T_e = \frac{3}{2} Z_p \frac{(L_m' i_{mr})^2}{R_r'} \omega_{slip} = \frac{3}{2} Z_p L_m' i_{sq} i_{mr} - \frac{3}{2} Z_p \omega_e \frac{(L_m' i_{mr})^2}{R_f'} \tag{3.50}$$

If the second expression from (3.49) is plugged into (3.50), the torque expression becomes the exactly same as (3.48).

Since $R_f' \gg R_r'$ and $R_f' + R_r' \gg (L_m i_{mr})^2$, the torque can be approximated as:

$$T_e \simeq \frac{3}{2} Z_p L_m' i_{sq} i_{mr} = K_t i_{sq} i_{mr} \tag{3.51}$$

where $K_t = \frac{3}{2} Z_P L'_m$

Then, in the steady state

$$i_{sq}(i_{sd}) = \frac{T_e}{K_t i_{sd}}. \tag{3.52}$$

The differentiation of total loss expression (3.47) with respect to i_{sd} for a constant torque gives:

$$\frac{dP_{total}}{di_{sd}} = 2R_d(\omega_r) i_{sd} + 2R_q i_{sq}(i_{sd}) \frac{di_{sq}(i_{sd})}{di_{sd}} \tag{3.53}$$

Plugging (3.51) and (3.52) into (3.53) leads to the following relation between i_{sq} and i_{sd}:

$$\frac{dP_{total}}{di_{sd}} = 2R_d(\omega_r) i_{sd} - 2R_q \frac{i_{sq}^2}{i_{sd}} = 0 \tag{3.54}$$

That is

$$R_d(\omega_r) i_{sd}^2 = R_q i_{sq}^2 \tag{3.55}$$

This result implies that the motor losses reach a minimum when the d and q axes losses are equal. Thus, an optimum level of magnetizing current, $i_{mr,opt}$ for minimum loss is given by:

$$i_{imr\_opt} = \sqrt{\frac{R_q}{R_d(\omega_r)}} i_{sq} = K i_{sq} \tag{3.56}$$

where $K \equiv \sqrt{\frac{R_q}{R_d(\omega_r)}} = \frac{i_{mr\_opt}}{i_{sq}}$ is Loss Factor (LF).

In a rotor flux oriented FOC of IM drives, torque control loop determines the reference value of i_{sq} and $i_{sd} = i_{mr}$ in steady state. Therefore, if every IM parameter is assumed to be constant at a particular speed, a single value of K is used to obtain $i_{mr,ref}$ from the instantaneous value of i_{sq} from (3.56). If $i_{mr,ref}$ exceeds the rated

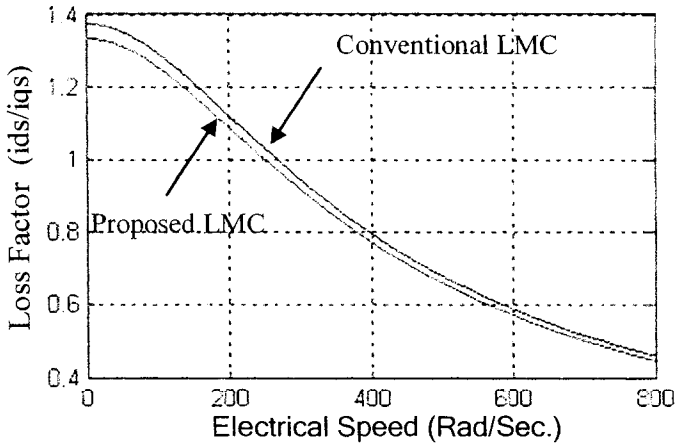

Fig.3.6: Loss Factor values of the traditional LMA and the proposed LMA against the electrical rotor speed.

value, the rated i_{mr} is used as reference to avoid magnetic saturation. When $i_{mr,ref}$ is equal to the rated value, there is no difference in the control algorithm as compared to the conventional FOC. Fig.3.6 shows LF of the traditional LMC utilized in [22] and the proposed LMC against the electrical rotor speed using the motor parameters specified in Appendix A. It is observed that the proposed scheme shows a smaller loss factor than the traditional one in all the speed ranges. Thus, it indicates that the proposed LMC yields less motor loss as compared to the conventional one.

From the perspective of torque control, it is not desirable to change the flux level frequently and in some applications, torque or speed control objective is more important than the loss minimization. Therefore, $i_{mr,ref}$ should be determined from a long-term viewpoint. For this purpose, the moving average filter is used for the experiment, so that instead of generating $i_{mr,ref}$ immediately, the magnetizing current command is chosen as the mean value of commands in a certain time window. The formula for a moving average filter is given by:

$$i_{imr\_opt(k)} = \frac{1}{N}\sum_{i=0}^{N} i_{imr\_opt(k-i)}$$

where N denotes the number of data in the time window.

For the simulation study, $i_{mr,ref}$ is fed through a filter with following transfer function:

$$G(s) = \frac{1024}{s^2 + 64s + 1024}$$

This filter offers a critically damped second-order response and reaches 99% of the reference value in about 0.2 sec.

3.4 Concluding Remarks

The losses involved in IM drives are classified and the causes of losses and the corresponding possible methods of loss reduction are explained in this chapter. With a focus on developing a better control technique to reduce motor loss, the basic principles of two different control techniques, SC and LMC, are explained and their advantages and disadvantage are compared. In order to overcome the disadvantages of LMC, a new LMA is proposed based on the motor model derived in Chapter 2. The step-by-step design procedures for control and parameter update laws are presented in the following chapter, which can be combined with the developed LMA to further overcome LMC's dependency on the parameters.

Chapter 4

Control System Design

This chapter explains the basic principle of the adaptive backstepping technique. Step-by-step design procedures to derive control and parameter update laws for IM drive are presented in detail. Stability analysis for the proposed controller is also provided.

4.1 Adaptive Backstepping Technique

Adaptive Backstepping is a systematic and recursive design methodology for nonlinear feedback control which makes use of the Lyapunov stability theory [52,53]. The key idea of adaptive backstepping is to systematically decompose a complex nonlinear control problem into simpler and smaller ones and to select recursively appropriate functions of state variables as so-called "virtual-control". Each backstepping stage results in a new virtual-control to deal with a decomposed subsystem problem and this virtual-control becomes a reference to the next design step for another subsystem. At the final stage, true control input for the original control objectives can be formed by summing up the Lyapunov functions associated with each individual design stage. While feedback linearization methods require

precise models and often cancel some useful nonlinearities, the adaptive backstepping design offers a choice of design tools for accommodation of uncertainties and nonlinearities and can avoid wasteful cancellations.

Another important feature of the backstepping design method is that it can be easily combined with adaptive control techniques. Parameter update laws can be obtained simultaneously with design steps of control laws. Hence, no extra effort to build other means for parameter adaptation is needed and the compensation of the parameter uncertainties in the system is quite straightforward.

Among the IM parameters, the rotor resistance is hard to measure and can vary up to $\pm$ 50% mainly because of the changes in temperature and load profile during operation. Therefore, the rotor resistance in terms of LMC is more critical than any other motor parameters. The load torque is unknown in most applications and has a great influence in servo performance. Therefore, in this thesis we design an adaptive backstepping controller with parameter uncertainties of the rotor resistance and load torque. The actual parameter adaptation law is derived for R_t, which is the parallel sum of R_r' and R_f', and rotor resistance value is extracted from it.

4.2 Adaptive Backstepping based Nonlinear Controller (ABNC)

The control objective is to design an asymptotically stable controller for IM to make both the amplitude of the magnetizing current i_{mr} and the mechanical rotor speed ω_m follow the reference signals satisfactorily. It is assumed that R_t, the parallel sum of rotor resistance and iron loss resistance and T_l, load torque are unknown but constant parameters, which need to be estimated on line.

Another issue that has to be mentioned before the start of the controller design is the estimation of the magnetizing current. In practice, measuring rotor flux is almost impossible or too expensive. Thus, in most control systems, the estimated values are used. This estimation can be obtained by many different methods such as applying observer [54], or Kalman filter technique [55]. In this thesis, the field amplitude i_{mr} and field angle θ_e are estimated based on the current equation derived in Chapter 2, which is defined for $\hat{i}_{mr} \neq 0$.

$$\hat{i}_{mr}(t) = \frac{1}{1+\frac{L'_m}{R_t}p} i_{sd}(t) \tag{4.1}$$

$$\begin{aligned} \hat{\theta}_e(t) &= \theta_r(t) + \hat{\theta}_{sl}(t) \\ &= \theta_m Z_p + \int_0^t \left(\frac{R_t}{L'_m}\frac{i_{sq}}{\hat{i}_{mr}} - \omega_r \frac{R_t}{R'_f}\right) d\tau \end{aligned} \tag{4.2}$$

Note that iron loss resistance is incorporated in the estimation of the magnetizing current. For the simplicity of the presentation the estimation symbol 'hat' is omitted in the following sections. Thus, unless otherwise mentioned, all the magnetizing currents used in the equations are estimated values.

4.2.1 Speed and Flux Control Design Steps

Step 1: For the speed and the magnetizing current tracking objectives, the tracking errors are defined by:

$$e_1 = i_{mr} - i_{mr,ref} \tag{4.3}$$

$$e_3 = \omega_m - \omega_{ref} \tag{4.4}$$

Then, the speed and magnetizing current error dynamic are given by:

$$\dot{e}_1 = \frac{R_t}{L'_m}(i_{sd} - i_{mr}) - \dot{i}_{mr,ref} \tag{4.5}$$

$$\dot{e}_3 = \mu i_{mr} i_{sq} - \mu\omega_e \frac{L'_m}{R'_f} i_{mr}^2 - \frac{T_l}{J} - \dot{\omega}_{ref} \tag{4.6}$$

To start the backstepping procedure, we choose i_{sd} and $i_{mr} i_{sq}$ as "virtual control" to make e_1 and e_3 in above equations converge to zero, which means that our tracking objectives are met. Assuming T_l and R_t are known at the beginning, we use the Lyapunov function given by:

$$V_1 = \frac{1}{2}(e_1^2 + e_3^2) \tag{4.7}$$

The derivatives of V_1 along with error dynamic (4.5) and (4.6) can be expressed as:

$$\begin{aligned} \dot{V}_1 &= e_1\dot{e}_1 + e_3\dot{e}_3 \\ &= e_1[\frac{R_t}{L'_m}(i_{sd} - i_{mr}) - \dot{i}_{mr,ref}] + e_3[\mu i_{mr} i_{sq} - \mu\omega_e \frac{L'_m}{R'_f} i_{mr}^2 - \frac{T_l}{J} - \dot{\omega}_{ref}] \end{aligned} \tag{4.8}$$

If the stabilizing virtual functions are chosen as

$$i_{sd,ref} = i_{mr} - k_1 \frac{L'_m}{\hat{R}_t} e_1 + \frac{L'_m}{\hat{R}_t} i_{mr,ref} \tag{4.9}$$

$$(i_{mr} i_{sq})_{ref} = \frac{1}{\mu}(-k_3 e_3 + \mu\omega_e \frac{L'_m}{R'_f} i_{mr}^2 + \frac{\hat{T}_l}{J} + \dot{\omega}_{ref}) \tag{4.10}$$

the derivative of the Lyapunov function is given by:

$$\dot{V}_1 = -k_1 e_1^2 - k_3 e_3^2 \tag{4.11}$$

With choices of $k_1 > 0$, $k_3 > 0$, the function is a negative semi-definite. Therefore, the tracking requirements are met. Note that since T_l and R_t are unknown parameters, the estimated values ($\hat{T}_l$, $\hat{R}_t$) are used in the virtual functions.

Step 2: In this step, we try to make i_{sd} and $i_{mr} i_{sq}$ become as desired in the previous step. Since i_{sd} and $i_{mr} i_{sq}$ are not final control inputs, other error variables are defined as below

$$e_2 = i_{sd} - i_{sd,ref} \tag{4.12}$$

$$e_4 = i_{mr} i_{sq} - (i_{mr} i_{sq})_{ref} \tag{4.13}$$

With the stabilizing virtual input chosen in the previous step, the newly-defined error variables e_2 and e_4 can be expressed by:

$$e_2 = i_{sd} - i_{sd,ref} = i_{sd} - i_{mr} + k_1 \frac{L'_m}{\hat{R}_t} e_1 - \frac{L'_m}{\hat{R}_t} \dot{i}_{mr,ref} \tag{4.14}$$

$$\begin{aligned} e_4 &= i_{mr} i_{sq} - (i_{mr} i_{sq})_{ref} \\ &= i_{mr} i_{sq} - \frac{1}{\mu}(-k_3 e_3 + \mu \omega_e \frac{L'_m}{R'_f} i_{mr}^2 + \frac{\hat{T}_l}{J} + \dot{\omega}_{ref} + \frac{\tilde{T}_l}{J}) \end{aligned} \tag{4.15}$$

where parameter estimation errors are defined as:

$$\tilde{T}_l = \hat{T}_l - T_l \tag{4.16}$$

$$\tilde{R}_t = \hat{R}_t - R_t \tag{4.17}$$

Then, error dynamic equations (4.5) and (4.6) can be combined with e_2 and e_4, and rewritten as:

$$\dot{e}_1 = -k_1 e_1 + \frac{\hat{R}_t}{L'_m} e_2 - \frac{\tilde{R}_t}{L'_m}(i_{sd} - i_{mr}) \tag{4.18}$$

$$\dot{e}_3 = -k_3 e_3 + \mu e_4 + \frac{\tilde{T}_l}{J} \tag{4.19}$$

After tedious but straightforward calculation, dynamical equation for the error variables e_2 and e_4 can be computed as:

$$\dot{e}_2 = \phi_1 + \frac{1}{L'_s} u_{sd} + \phi_2 \tilde{R}_t \tag{4.20}$$

$$\dot{e}_4 = \phi_3 + \frac{1}{L'_s} i_{mr} u_{sq} + \phi_4 \tilde{R}_t + \frac{k_3 \tilde{T}_l}{\mu J} \tag{4.21}$$

where

$$\phi_1 = -\frac{R_s}{L'_s} i_{sd} + \omega_e i_{sq} - (\frac{\hat{R}_t}{L'_s} + \frac{\hat{R}_t}{L'_m} - k_1)(i_{sd} - i_{mr}) - \frac{k_1 L'_m}{\hat{R}_t} \dot{i}_{mr,ref} - \frac{L'_m}{\hat{R}_t} \ddot{i}_{mr,ref} \tag{4.22}$$

$$\phi_2 = (\frac{1}{L'_s} + \frac{1}{L'_m} - \frac{k_1}{\hat{R}_t})(i_{sd} - i_{mr}) \tag{4.23}$$

$$\begin{aligned}\phi_3 = {} & \frac{\hat{R}_t}{L'_m}(i_{sd} - i_{mr})i_{sq} + i_{mr}(-\frac{R_s}{L'_s}i_{sq} - \omega_e i_{sd} - \frac{\hat{R}_t}{L'_s}i_{sq} \\ & - \omega_r \frac{L'_m}{L'_s}(1 - \frac{\hat{R}_t}{R'_f})i_{mr}) - \frac{1}{\mu}(-k_3\mu i_{mr}i_{sq} + k_3\mu\omega_e \frac{L'_m}{R'_f}i_{mr}^2 \\ & + k_3\frac{\hat{T}_l}{J} + k_3\dot{\omega}_{ref} + \frac{\dot{\hat{T}}_l}{J} + \ddot{\omega}_{ref} + 2\mu\omega_e \frac{L'_m}{R'_f}i_{mr} + \mu\dot{\omega}_e \frac{L'_m}{R'_f}i_{mr}^2)\end{aligned} \tag{4.24}$$

$$\phi_4 = -\frac{1}{L'_m}(i_{sd} - i_{mr})i_{sq} + \frac{1}{L'_s}i_{mr}i_{sq} - \omega_r \frac{L'_m}{L'_s}\frac{1}{R'_f}i_{mr}^2 \tag{4.25}$$

ϕ_1 and ϕ_3 will be used in the design of the final control law while ϕ_2 and ϕ_4 will be used in the design of the parameter update law.

Since we see the actual control inputs u_{sd} and u_{sq} in the error dynamics, we can design the final control. Without considering parameter estimation errors $\tilde{T}_l$, $\tilde{R}_t$, a new Lyapunov function to design the final control is defined as:

$$V = \frac{1}{2}(e_1^2 + e_2^2 + e_3^2 + e_4^2) \tag{4.26}$$

The derivative of V along the trajectory of the system, i.e., (4.18)-(4.21), is

$$\begin{aligned}\dot{V} &= e_1\dot{e}_1 + e_2\dot{e}_2 + e_3\dot{e}_3 + e_4\dot{e}_4 \\ &= e_1(-k_1e_1 + \frac{\hat{R}_t}{L'_m}e_2) + e_2(\phi_1 + \frac{1}{L'_s}u_{sd}) \\ &\quad + e_3(-k_3e_3 + \mu e_4) + e_4(\phi_3 + \frac{1}{L'_s}i_{mr}u_{sq})\end{aligned} \tag{4.27}$$

If we choose the control laws as

$$u_{sd} = L'_s(-\frac{\hat{R}_t}{L'_m}e_1 - k_2e_2 - \phi_1) \tag{4.28}$$

$$u_{sq} = \frac{L'_s}{i_{mr}}(-\mu e_3 - k_4e_4 - \phi_3) \tag{4.29}$$

the derivative of the Lyapunov function becomes

$$\dot{V} = -k_1 e_1^2 - k_2 e_2^2 - k_3 e_3^2 - k_4 e_4^2 \ . \tag{4.30}$$

For $k_1, k_2, k_3, k_4 > 0$, the tracking requirements of the magnetizing current and rotor speed are met.

4.2.2 Parameter Adaptation

With the final control input (4.28) and (4.29), we achieve closed loop error dynamics in matrix form governed by:

$$\dot{e} = Ae + W\tilde{\vartheta} \tag{4.31}$$

That is

$$\begin{bmatrix} \dot{e}_1 \\ \dot{e}_2 \\ \dot{e}_3 \\ \dot{e}_4 \end{bmatrix} = - \begin{bmatrix} k_1 & 0 & 0 & 0 \\ 0 & k_2 & 0 & 0 \\ 0 & 0 & k_3 & 0 \\ 0 & 0 & 0 & k_4 \end{bmatrix} \begin{bmatrix} e_1 \\ e_2 \\ e_3 \\ e_4 \end{bmatrix} + \begin{bmatrix} -(i_{sd} - i_{mr})/L'_m & 0 \\ \phi_2 & 0 \\ 0 & 1/J \\ \phi_4 & k_3/\mu J \end{bmatrix} \begin{bmatrix} \tilde{R}_t \\ \tilde{T}_l \end{bmatrix}$$

$\tilde{\vartheta}$ is an unknown perturbation to the error dynamics and both e and W can be computed from directly measured signal and estimated values. We consider a new Lyapunov function as

$$V = e^T P e + \tilde{\vartheta}^T \Gamma^{-1} \tilde{\vartheta} \tag{4.32}$$

where Γ is a positive-definite symmetric adaptive gain matrix and P is the positive-definite symmetric matrix which solves the Lyapunov equation , $A^T P + PA = -Q$ given any positive-definite symmetric matrix Q. Time-differentiation on both sides of (4.32) gives

$$\dot{V} = -e^T Q e + 2\tilde{\vartheta}^T (\Gamma^{-1} \dot{\tilde{\vartheta}} + W^T P e) \tag{4.33}$$

If we select the parameter update law

$$\dot{\tilde{\vartheta}} = -\Gamma W^T P e \tag{4.34}$$

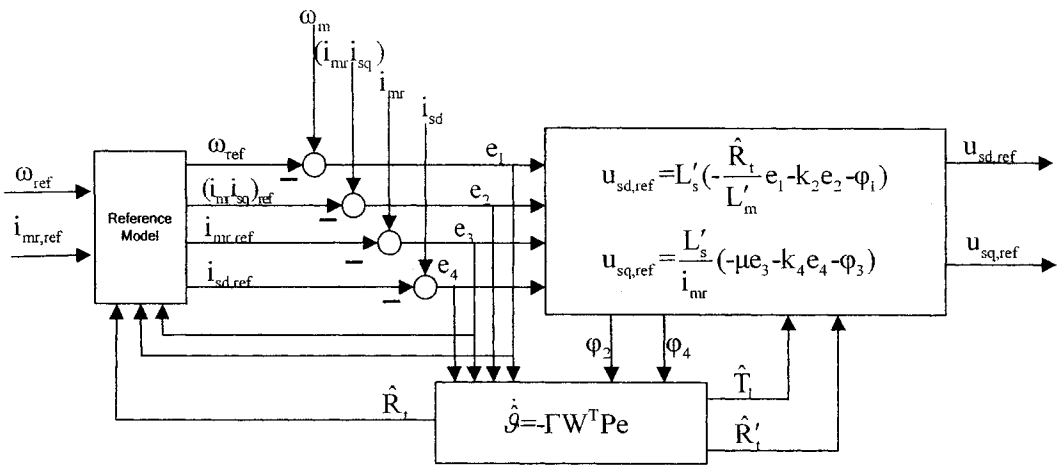

Fig.4.1: Block diagram of nonlinear controller and adaptation laws

then, derivative of the Lyapunov function is given by:

$$\dot{V} = -e^T Qe = -k_1 e_1^2 - k_2 e_2^2 - k_3 e_3^2 - k_4 e_4^2 \le 0 \tag{4.35}$$

4.2.3 Stability Analysis

$\dot{V} \le 0$ from (4.35) implies that $V(t) \le V(0)$, therefore the tracking errors, e_1, e_2, e_3 and e_4 ,and the parameter errors, $\tilde{R}_t$ and $\tilde{T}_l$ are bounded and confined to a closed ellipsoidal region in the error space. Integrating (4.35) gives

$$V(t) = V(e(0), \tilde{\vartheta}(0)) + \int_0^t \dot{V}(\tau) d\tau = V(e(0), \tilde{\vartheta}(0)) - \int_0^t e^T Qe d\tau \tag{4.36}$$

Thus,

$$\int_0^t e^T Qe d\tau = V(e(0), \tilde{\vartheta}(0)) - V(t) \ . \tag{4.37}$$

Considering $\dot{V}(t) \le 0$ and $V(t) \ge 0$, we can derive the following result

$$\lim_{t \to \infty} \int_0^t e^T Qe d\tau \le V(e(0), \tilde{\vartheta}(0)) < \infty \ . \tag{4.38}$$

Through Barbalat's Lemma [58], it can be shown that e_1, e_2, e_3 and e_4 converge to zero as $t \to \infty$. Hence, the rotor speed and field magnetizing current tracking objectives are achieved under parameter uncertainties of R_t and T_l. The block diagram of the nonlinear controller and adaptation laws is given in Fig.4.1

4.3 Concluding Remarks

The fundamental ideas of adaptive backstepping are presented in this chapter. Based on the mathematical model in Chapter 2, an adaptive backstepping based nonlinear controller (ABNC) is proposed for the induction motor drive incorporating the iron loss as a robust speed controller. The detailed design procedures for control and parameter update laws are presented as well as stability analysis. Before going to implementation in real-time, it is a usual practice to predict the performance of the drive in simulation. Therefore, the simulation of a vector controlled IM drive incorporating ABNC is given in the following chapter.

Chapter 5

Simulation of the Complete Adaptive Backstepping based Online Loss Minimization Control of an IM Drive

This chapter presents the development of a proposed IM drive system for the simulation study using MATLAB/Simulink software. After an explanation about the overall system with particular attention to the three-phase inverter and its operation by PWM control scheme, extensive simulation results on the proposed controller, LMA and complete IM drive system are presented.

5.1 Drive System

In order to verify the effectiveness of the proposed loss minimization scheme and control strategy in Chapters 3 and 4, the computer simulation model has been developed using Matlab/Simulink software [45]. The proposed closed loop vector control scheme of the IM is shown in Fig.5.1 and corresponding Simulink schematic diagram is shown in Fig.5.2. The IM parameters used in the simulation and subsystems of Simulink model are given in Appendix A and Appendix C, respectively.

The motor phase currents are fed into the Clarke and Park transformation block, namely *abc/dq* block. This transformation gives the currents in the *dq* coordinates rotating reference frame. The magnetizing current reference is generated based on the

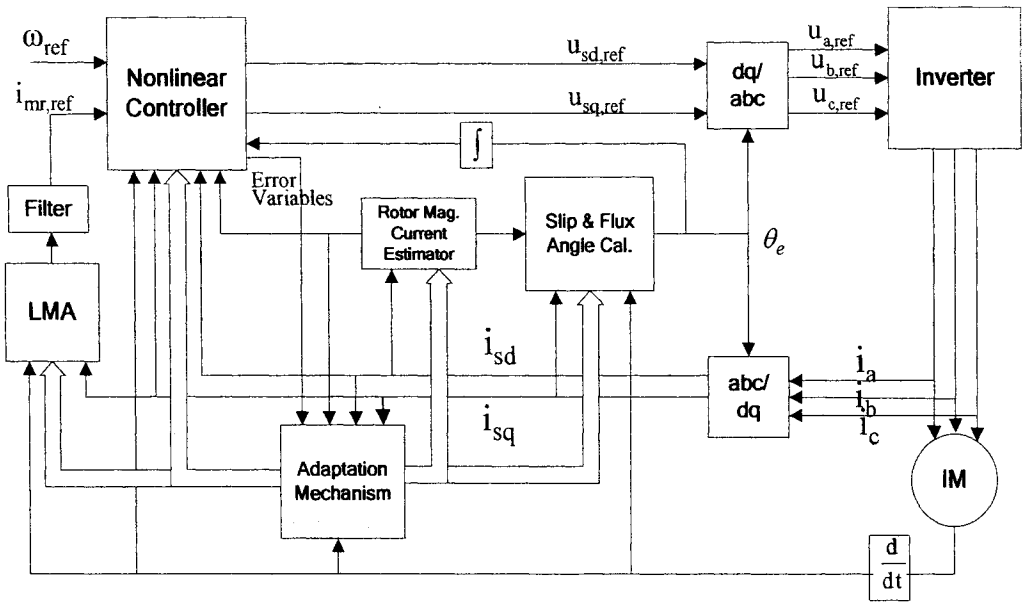

Fig.5.1: Block diagram of the proposed IM control system

currents transformed into *dq* coordinates and the electrical rotor speed of the motor using equation (3.56). This magnetizing current reference and rotor speed reference are the inputs to the ABNC. The command voltages ($u_{sd,ref}, u_{sq,ref}$), which is the outputs of the ABNC, are determined using the control law equations (4.28) and (4.29) as displayed in Fig.4.1. The command voltages are applied to the inverse Clark and Park transformation (*dq/abc* block) to reverse into *abc* coordinate values. These are the input to the three-phase inverter and will generate the signals that drive the inverter by comparing with high frequency Pulse Width Modulation (PWM) carrier signals. The details about the operation of the three-phase inverter and PWM technique are explained in the following sub-sections. Note that both *abc/dq* and *dq/abc* transformation need the information of the rotor flux position. This rotor flux position along with the rotor magnetizing current are estimated utilizing equations (4.1) and (4.2) as explained in chapter 4. The parameters R_l and T_l are estimated

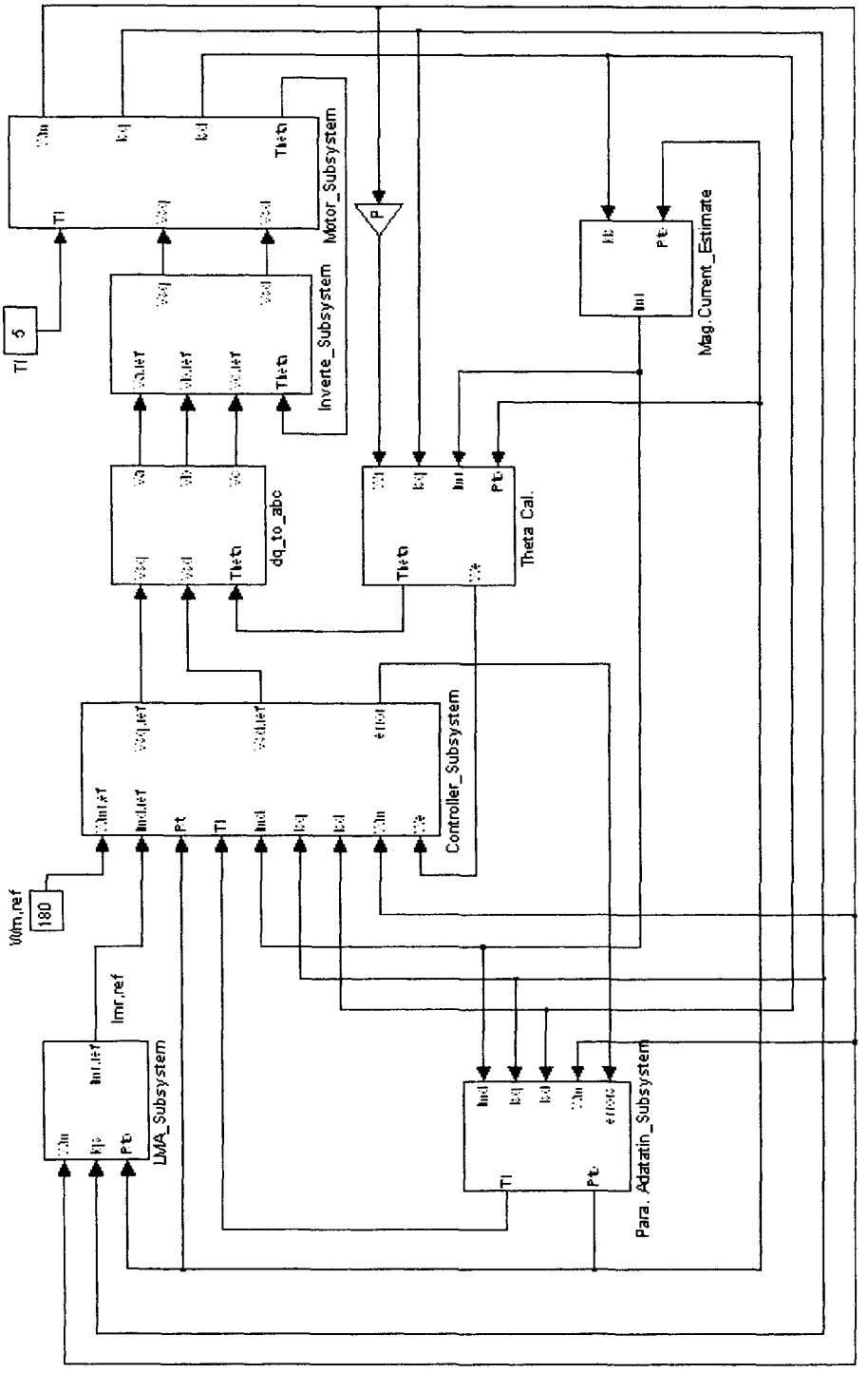

Fig.5.2: Simulink schematic of the complete ABNC based IM drive system

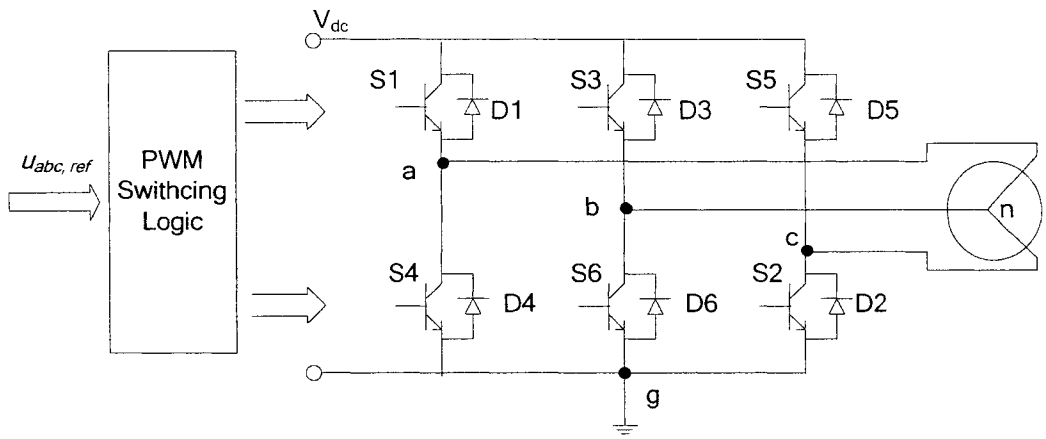

Fig.5.3: Three-phase inverter feeding a Y-connected IM

using equation (4.34) as shown in Fig.4.1 and update all R_l and T_l values used in the blocks in drive system.

5.1.1 Three-Phase Inverter

A switch-mode dc-ac voltage-source inverter feeding an IM is shown in Fig.5.3. This inverter consists of three legs, each having two transistor switches and two diodes. The motor terminals (a, b and c) are connected to the mid-point of each inverter leg. The motor phase windings are Y-connected. 'n' is the neutral point and 'g' is the inverter ground. The inverter leg voltages (with respect to ground g) are denoted by

$$u_{abcg} = \begin{bmatrix} u_{ag} \\ u_{bg} \\ u_{cg} \end{bmatrix} \tag{5.1}$$

and the motor phase voltages (with respect to neutral n) are denoted by

$$u_{abcn} = \begin{bmatrix} u_{an} \\ u_{bn} \\ u_{cn} \end{bmatrix} \tag{5.2}$$

Application of Kirchhoff's voltage law to the inverter motor circuit in Fig.5.3 yields a relationship between the inverter leg voltages u_{abcg} and motor phase voltages u_{abcn} as below:

$$u_{abcn} = u_{abcg} - u_{ng} l_3 \tag{5.3}$$

where u_{ng} is the voltage drop from the motor neutral into the inverter ground g and l_3 is defined as:

$$l_3 = \begin{bmatrix} 1 \\ 1 \\ 1 \end{bmatrix} \tag{5.4}$$

For the instantaneous balanced 3-phase motor phase voltage,

$$u_{an} + u_{bn} + u_{cn} = 0 \tag{5.5}$$

Combining (5.3) with (5.5) yields

$$u_{ng} = \frac{1}{3}(u_{ag} + u_{bg} + u_{cg}) \tag{5.6}$$

Substituting u_{ng} from (5.6) into (5.3) results in

$$u_{abcn} = C u_{abcg} \tag{5.7}$$

where C is the coupling matrix given by

$$C = \frac{1}{3}\begin{bmatrix} 2 & -1 & -1 \\ -1 & 2 & -1 \\ -1 & -1 & 2 \end{bmatrix} \tag{5.8}$$

The equation (5.7) implies that it is possible to express the motor phase voltage u_{abcn} from the inverter leg voltage u_{abcg}.

The basic operation of the three-phase inverter can be explained by considering the single inverter leg. For example, turning on switch S1 and turning off switch S4 would establish V_{dc} across terminals 'a' and 'g', therefore u_{ag}=V_{dc}. On the other hand, turning off S1 and turning on S4 would apply zero voltage across 'a' and 'g',

therefore u_{ag}=0. Turning on both S1 and S4 would short the voltage bus to ground, thus a dead time must be included in switching logic by intentionally delaying the all off-on transitions of the transistor switches. During the dead time, both S1 and S4 are simultaneously turned off and the direction of current i_a will determine the actual voltage. If $i_a < 0$, then u_{ag}=V_{dc} and diode D1 will conduct. If $i_a > 0$, then u_{ag}=0 and diode D4 will conduct.

Since the on-and-off states of the power switches in one inverter leg are always opposites without considering the dead time, each inverter leg can be in either of two states. Therefore, the three-phase inverter as a whole can be in any of possible eight states. Table 5.1summarizes these eight inverter states and corresponding invert leg voltages and motor phase voltage using the relations in (5.7).

5.1.2 Pulse Width Modulation (PWM)

Among the various PWM schemes, well-known are sinusoidal PWM, hysteresis PWM, space vector modulation (SVM). The PWM strategies considered in this thesis are sinusoidal PWM and hysteresis PWM.

In sinusoidal PWM, three-phase reference voltages of variable amplitude and frequency from the controller are compared in three separate comparators with a common triangular carrier wave of fixed amplitude and frequency. In the entire control system, the inverter reference signals are initially issued in the *dq* co-ordinates from the controller and then transformed into the *abc* coordinates. Each comparator output forms the switching-state of the corresponding inverter leg. The sinusoidal reference voltage establishes the desired fundamental frequency of the inverter output, while the triangular carrier wave establishes the switching frequency of the inverter. The switches of the phase legs are controlled based on the following comparison:

Phase state 'abc'	u_{ag}	u_{bg}	u_{cg}	u_{an}	u_{bn}	u_{cn}
000	0	0	0	0	0	0
001	0	0	V_{dc}	-1/3V_{dc}	-1/3 V_{dc}	2/3V_{dc}
010	0	V_{dc}	0	-1/3 V_{dc}	2/3 V_{dc}	-1/3 V_{dc}
011	0	V_{dc}	V_{dc}	-2/3 V_{dc}	1/3 V_{dc}	1/3 V_{dc}
100	V_{dc}	0	0	2/3 V_{dc}	-1/3 V_{dc}	-1/3 V_{dc}
101	V_{dc}	0	V_{dc}	1/3 V_{dc}	-2/3 V_{dc}	1/3 V_{dc}
110	V_{dc}	V_{dc}	0	1/3 V_{dc}	1/3 V_{dc}	-2/3 V_{dc}
111	V_{dc}	V_{dc}	V_{dc}	0	0	0

Table 5.1: possible cases of inverter state and corresponding inverter leg voltages (u_{ag}, u_{bg}, u_{cg}) and motor phase voltage (u_{an}, u_{bn}, u_{cn})

$u_{a,ref} > u_{triangle}$, S1 is on, State 1 for phase a

$u_{a,ref} < u_{triangle}$, S4 is on, State 0 for phase a

$u_{b,ref} > u_{triangle}$, S3 is on, State 1 for phase b

$u_{b,ref} < u_{triangle}$, S6 is on, State 0 for phase b

$u_{c,ref} > u_{triangle}$, S5 is on, State 1 for phase c

$u_{c,ref} < u_{triangle}$, S2 is on, State 0 for phase c

Figure 5.4 (a) shows the sinusoidal PWM signal generation and corresponding inverter leg voltages (u_{ag}, u_{bg}, u_{cg}) and motor phase voltage u_{an} when dead time = 0.

In hysteresis PWM, the switch logic is realized by three hysteresis controllers, one for each phase. Each controller determines the switching state of one inverter leg in such a way that the corresponding actual current is maintained within a hysteresis

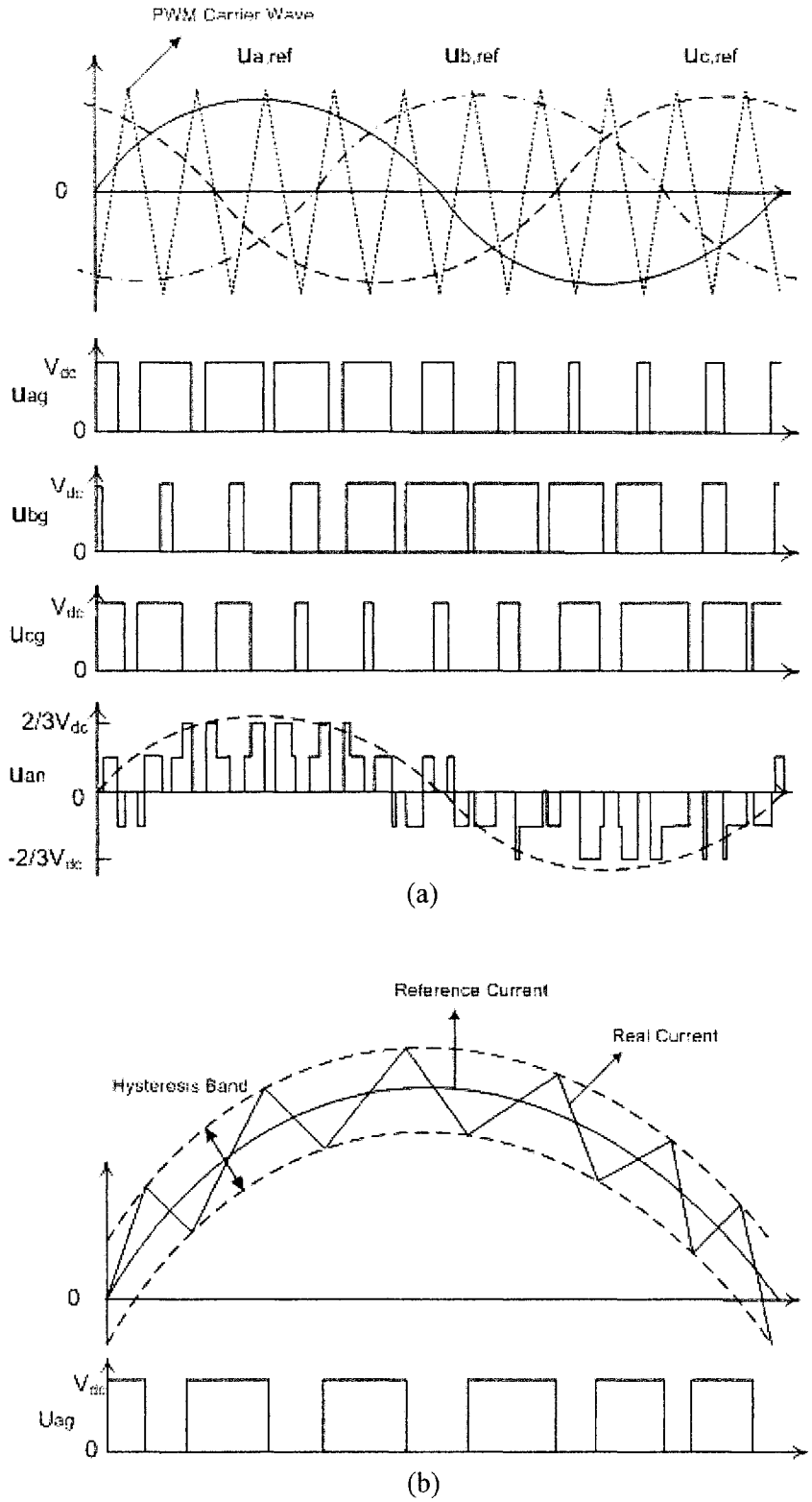

Fig.5.4: Pulse Width Modulation (PWM) when dead time = 0: (a) Sinusoidal PWM signal generation with inverter leg voltages (u_{ag}, u_{bg}, u_{cg}) and a motor phase voltage u_{an} and (b) hysteresis PWM signal generation with inverter leg voltage (u_{ag}).

band Δi of reference current. To increase a phase current, the corresponding inverter leg voltage is equal to the V_{dc} until the upper band-range is reached. Then, the negative V_{dc} is applied until the phase current drops to the lower limit of a hysteresis. Due to the elimination of an additional current controller, the motor parameter dependence is very low. However, PWM frequency is not fixed and switching frequency increase at lower modulation. Fig.5.4 (b) shows hysteresis PWM signal generation and an inverter leg voltage.

5.2 Simulation Results and Discussion

5.2.1 Performance of ABNC

An extensive simulation has been done in order to predict the performance of the proposed adaptive backstepping based nonlinear controller (ABNC) and LMA. First, the performance of the proposed ABNC and drive system has been investigated. The controller gains, k_1, k_2, k_3 and k_4 are chosen as 800, 800, 400 and 400 respectively.

Figure 5.5 (a) shows the speed response for the reference speed of 180 rad/s at no load condition. The actual speed converges to the reference speed in a very short time without any overshoot and nearly zero steady state error. Figs. 5.5 (b) and (c) show the developed torque and the output voltage from the PWM inverter, respectively. The actual motor phase current i_a is shown in Fig. 5.5 (d).

Figures 5.6 (a) to (d) show the corresponding tracking errors e_1, e_2, e_3 and e_4 defined in backstepping design which all successfully converge to 0. Thus, it ensures the global stability of the drive system and it was the goal in designing the controller.

In Fig. 5.7, the motor is commanded to track the velocity trajectory, $\omega_{ref}(t) = 50\cos(2\pi t)$, at no load condition. Figs. 5.7 (a) and (b) show the speed response and developed torque, respectively and actual a, b and c-phase currents are shown in Fig. 5.7 (c). It is shown that the proposed controller successfully tracks the given sinusoidal speed reference.

Figures 5.8 (a)-(c) show the responses including speed, developed torque and actual phase current i_a at full load (49 N.m) and speed command of 180 rad/s. The speed follows the speed command without any overshoot or stead-state error and developed torque settles down at the value of load torque. Although the only two cases, no load and full load condition, are shown in this thesis, more simulations are done at many different load conditions with satisfactory results. Therefore, the proposed ABNC based IM drive can follow the command speed at various loading conditions.

In high performance drive applications, it is essential to change the speed reference with situational demand. Figure 5.9 (a) shows the speed response for a step decrease in reference speed from 150 rad/s to 50 rad/s at no load condition. There is a small undershoot ($\approx$ 6 rad/s), but actual speed converges with the reference with no steady state error. Figs. 5.9 (b)-(d) show the corresponding result of the developed torque, the phase current and steady state of a, b and c-phase currents.

Figures 5.10 (a)-(c) show the responses of speed, developed torque and a phase current for a step increase in reference speed from 180 rad/s to 300 rad/s at no load condition. Again, the speed follows the speed reference without overshoot and steady state error. Since the motor is commanded to run in the field weakening area, the magnetizing current reference is reduced beyond the rated speed by the field weakening rule. The function in M code for this field weakening rule is shown in

Appendix B3 and the magnetizing current command is shown in Fig. 5.10 (d). As a result of this reduction in magnetizing current, the transient time from 180 to 300 rad/s is longer than one from 0 to 180 rad/s.

Figures 5.11 (a) and (b) show the speed and developed torque with the step changes in reference speed from 150 to 50 rad/s and 180 to 360 rad/s, respectively at full load conditions. Similar results as in Fig. 5.9 and Fig. 5.10 are obtained.

Another important feature that has to be tested is the robustness of the controller to the disturbances. The change of load is a typical external disturbance and also for a high performance drive, the load change is a very common situation. Figure 5.12 shows the speed and developed torque responses with step changes in load. Fist, the motor started with half load (24.5 N.m) while the motor is running at a speed of 180 rad/s. Then, load is suddenly increased to full load (49 N.m) at t=0.5 s and again load is decreased to no load (0 N.m) at t=1 s. As shown in Fig.5.12 (a) the drop and spike in speed due to the sudden load changes are very small, and the speed recovered to its command speed in a very short time, showing the insensitivity of the controller to these step changes of load.

Figure 5.13 shows the simulation results to test the effectiveness of parameter adaptation. The motor is started with wrong parameter values of T_l =1 Nm, and R_r'=0.1 Ω to the controller at a reference speed of 180 rad/s while the true values are T_l = 5 Nm and R_r'=0.3105 Ω . At t=2 s, parameter adaptation is activated, and at t=5 s, a step load of 35 Nm is applied suddenly. Figs. 5.13 (a) and (b) show the successful parameter adaptation results and Fig. 5.13 (c) shows the speed response. There is a steady state error in speed due to the wrong parameters before the parameter adaptation is activated as shown in Fig. 5.12 (c). However, once parameter adaptation is initiated at t=2 s, this steady state error becomes zero. At t=5 s, speed drop is

observed due to sudden load increase, but speed is recovered to its reference value in a short time due to the effectiveness of the adaptation laws.

Figure 5.14 shows the simulation results of the developed torque and speed responses when the motor is accelerated and decelerated between 150 rad/s and 180 rad/s by torque control at no load condition. When the motor is being accelerated and decelerated, the reference torques are 6 N.m and –6 N.m, respectively. When the motor is being accelerated, if the speed becomes 180 rad/s, the torque reference is changed from 6 N.m to -6 N.m and vice versa. Fig. 5.14 (a) shows the responses of the controller designed without the iron loss consideration. In this case, the actual torque is lower than the reference torque. As a result, the acceleration is slower than the deceleration. The iron loss in the motoring area can be regarded as the extra power that has to be supplied to the machine by the inverter in order to achieve perfect torque control, so that the actual output torque is lower than the reference torque. In contrast, the extra power corresponding to iron loss is added to the converted mechanical power in the braking area, so that the absolute value of the actual torque is higher than reference torque. Fig. 5.14 (b) is the case of the proposed controller, in which iron loss is considered and shows the accurate torque regulation.

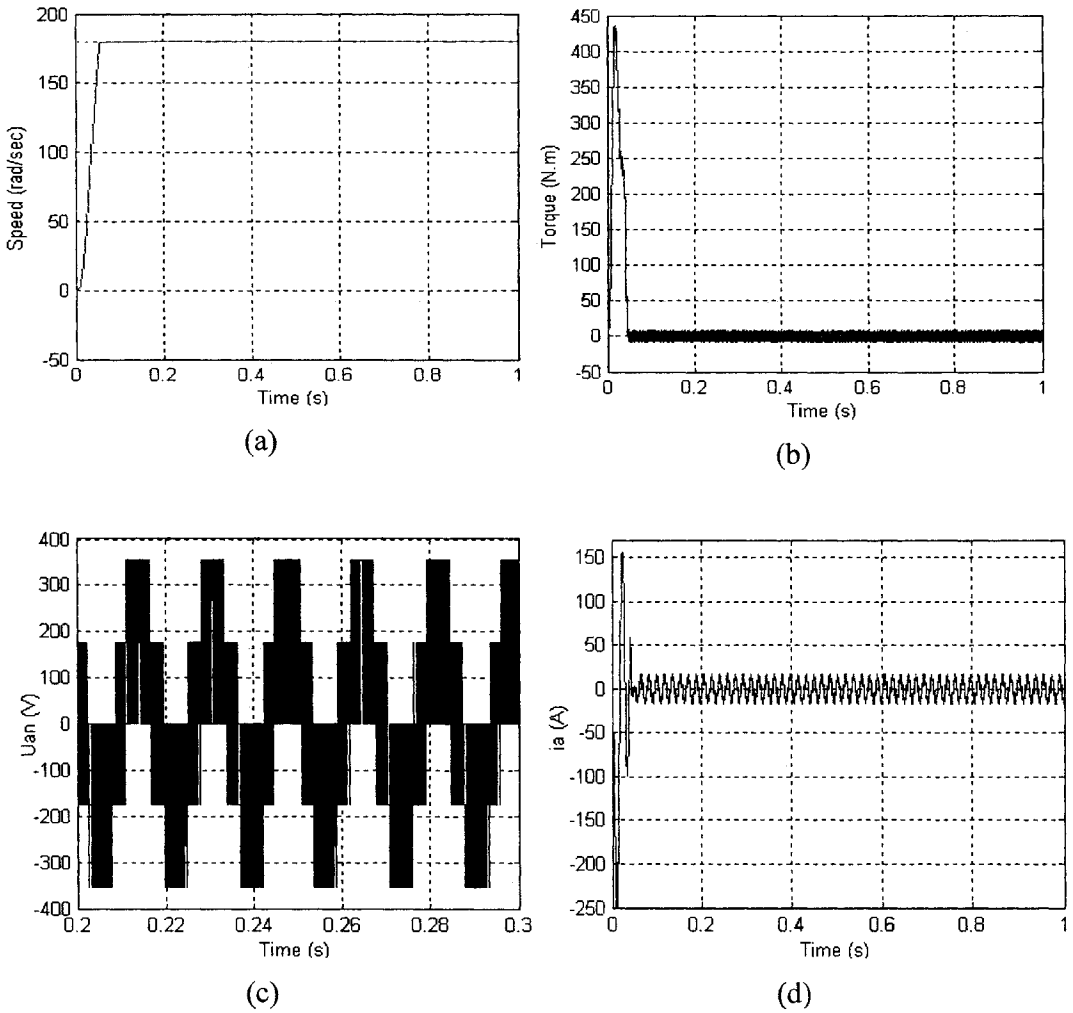

Fig.5.5: Simulated responses of the proposed ABNC and drive at no load and speed of 180 rad/sec: (a) speed, (b) developed torque, (c) output voltage from PWM inverter, and (d) actual a-phase current.

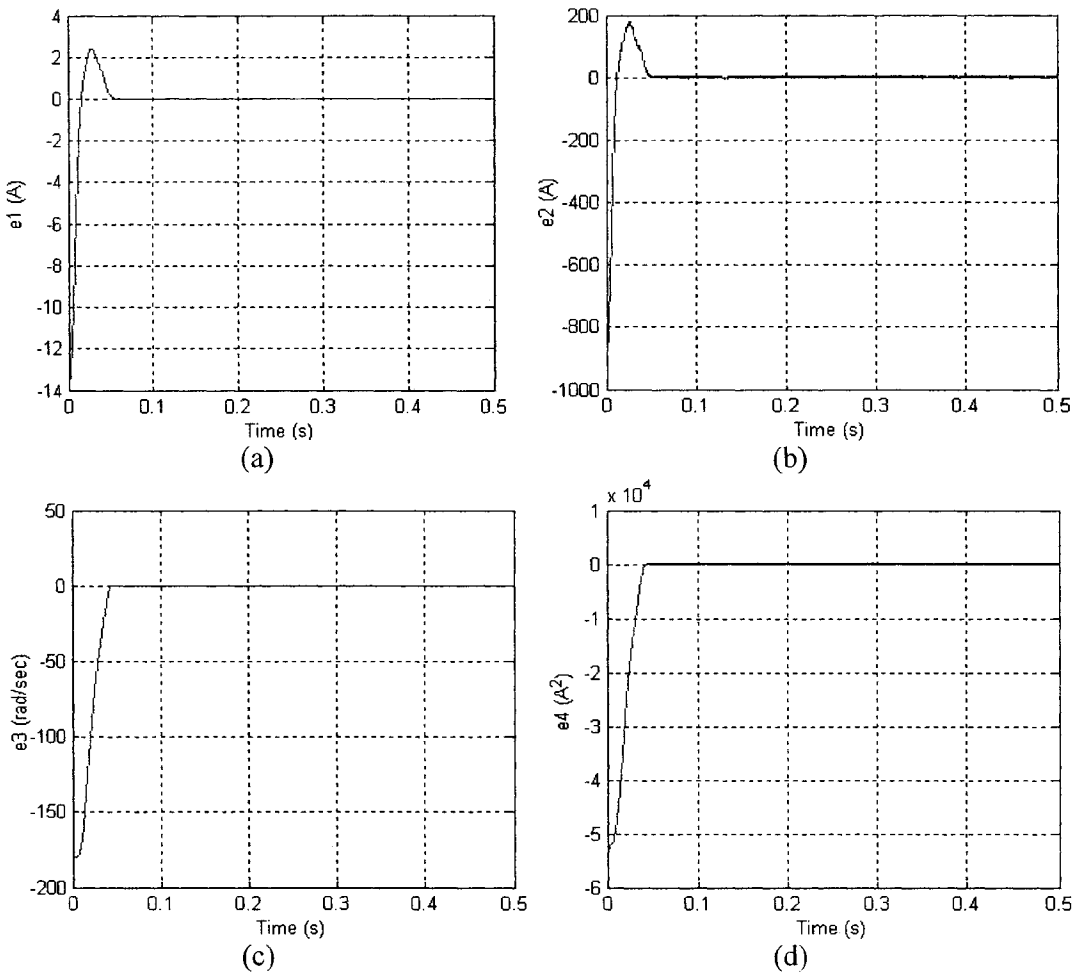

Fig.5.6: Simulated responses of the proposed ABNC and drive at no load and speed of 180 rad/sec: (a) magnetizing current tracking error ($e_1 = i_{mr} - i_{mr,ref}$), (b) d-axis current tracking error ($e_2 = i_{sd} - i_{sd,ref}$), (c) speed tracking error ($e_3 = \omega_m - \omega_{ref}$), and (d) torque related tacking error ($e_4 = i_{mr} i_{sq} - (i_{mr} i_{sq})_{ref}$).

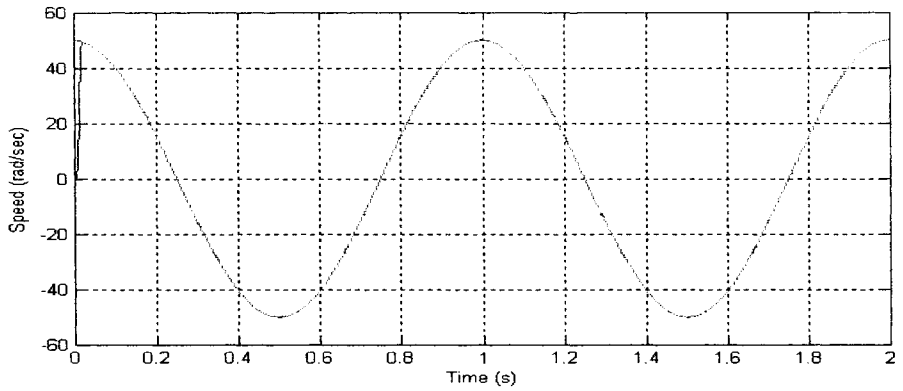

(a)

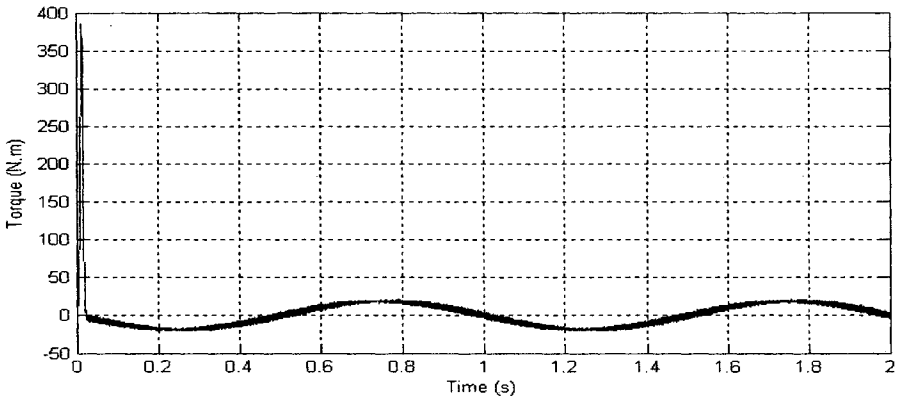

(b)

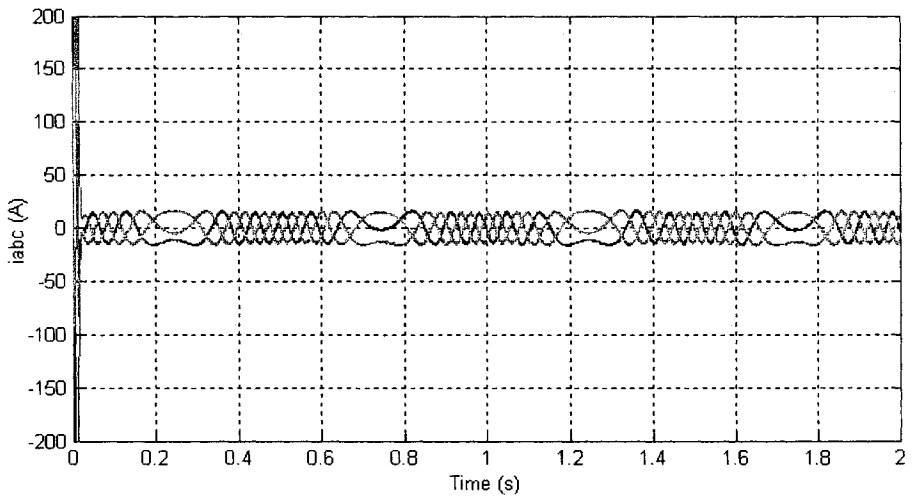

(c)

Fig.5.7: Simulated responses of the proposed ABNC and drive at no load and speed command of $\omega_{ref}(t) = 50\cos(2\pi t)$: (a) speed, (b) develop torque, and (c) actual a, b and c-phase currents.

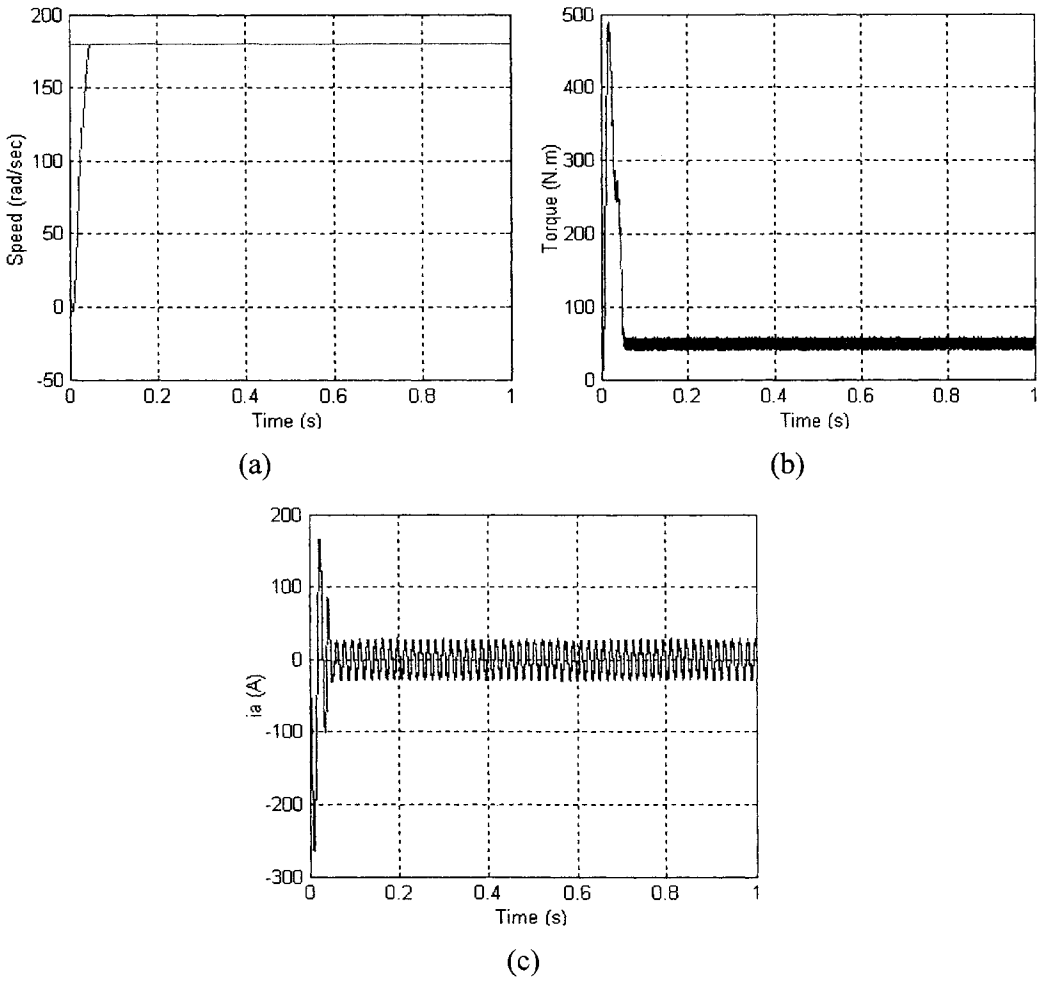

Fig.5.8: Simulated responses of the proposed ABNC and drive at full load and speed of 180 rad/sec: (a) speed, (b) developed torque, and (c) actual a-phase current.

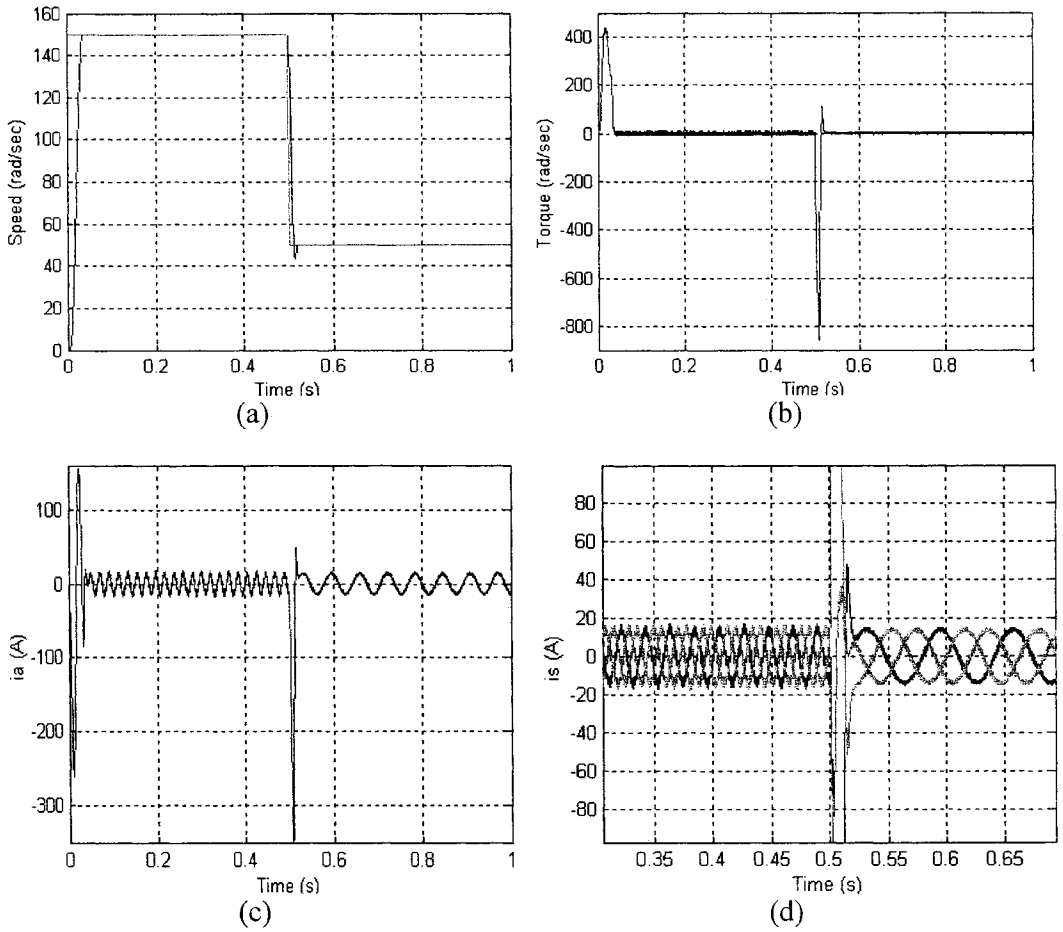

Fig.5.9: Simulated responses of the proposed ABNC and drive at no load and with step change in command speed: (a) speed, (b) developed torque, (c) actual a-phase current, and (d) actual a, b and c-phase current.

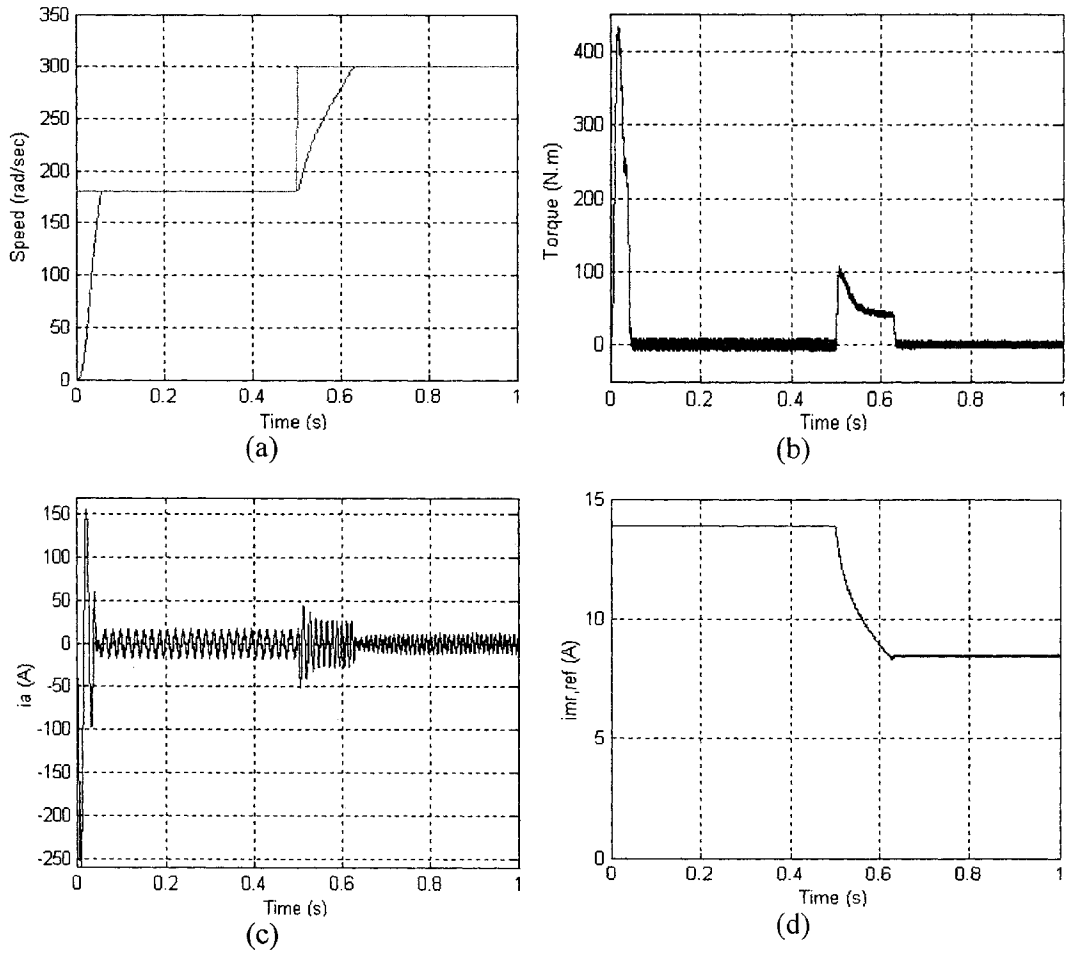

Fig.5.10: Simulated responses of the proposed ABNC and drive at no load and with step change in command speed: (a) speed, (b) developed torque, (c) actual a-phase current, and (d) magnetizing current reference.

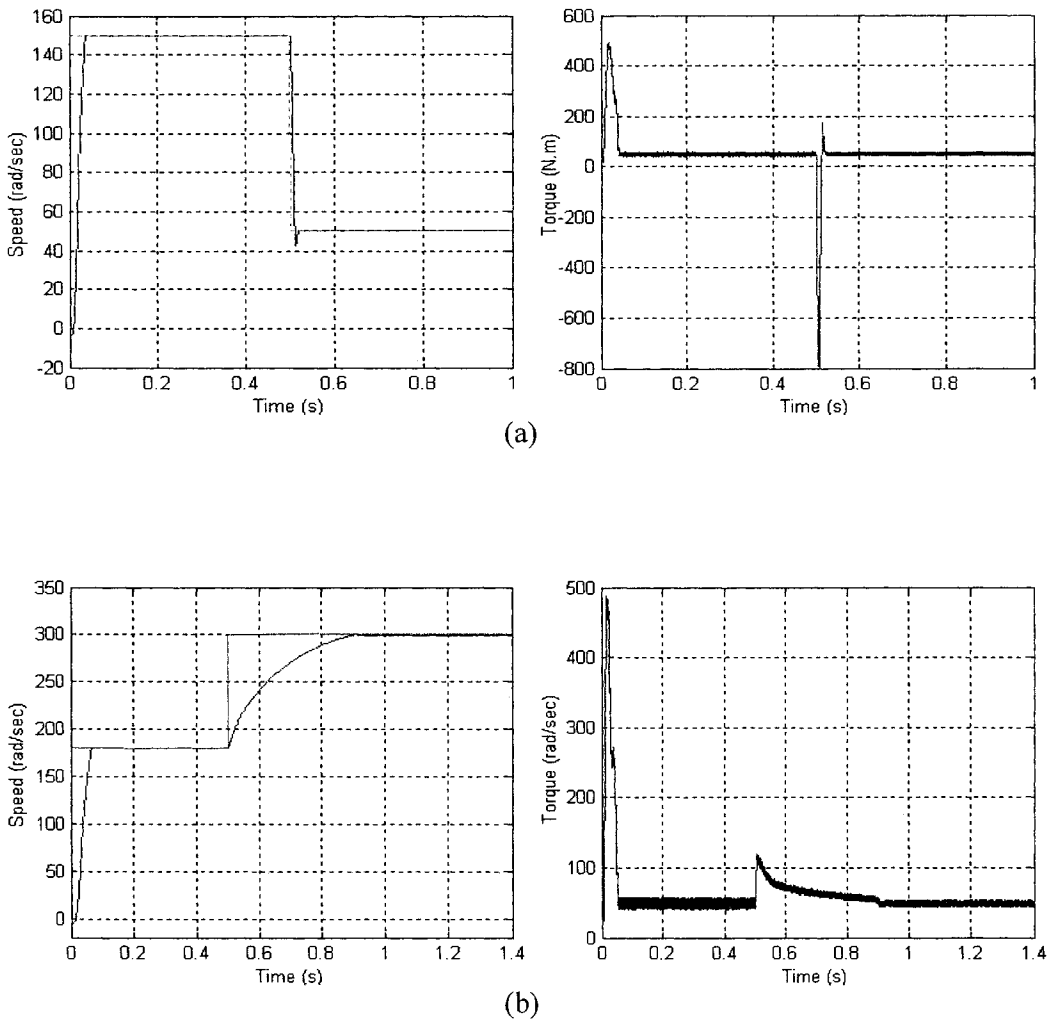

Fig.5.11: Simulated responses of the proposed ABNC and drive at full load and with step change in command speed: (a) speed, (b) developed torque, (c) speed, and (d) developed torque.

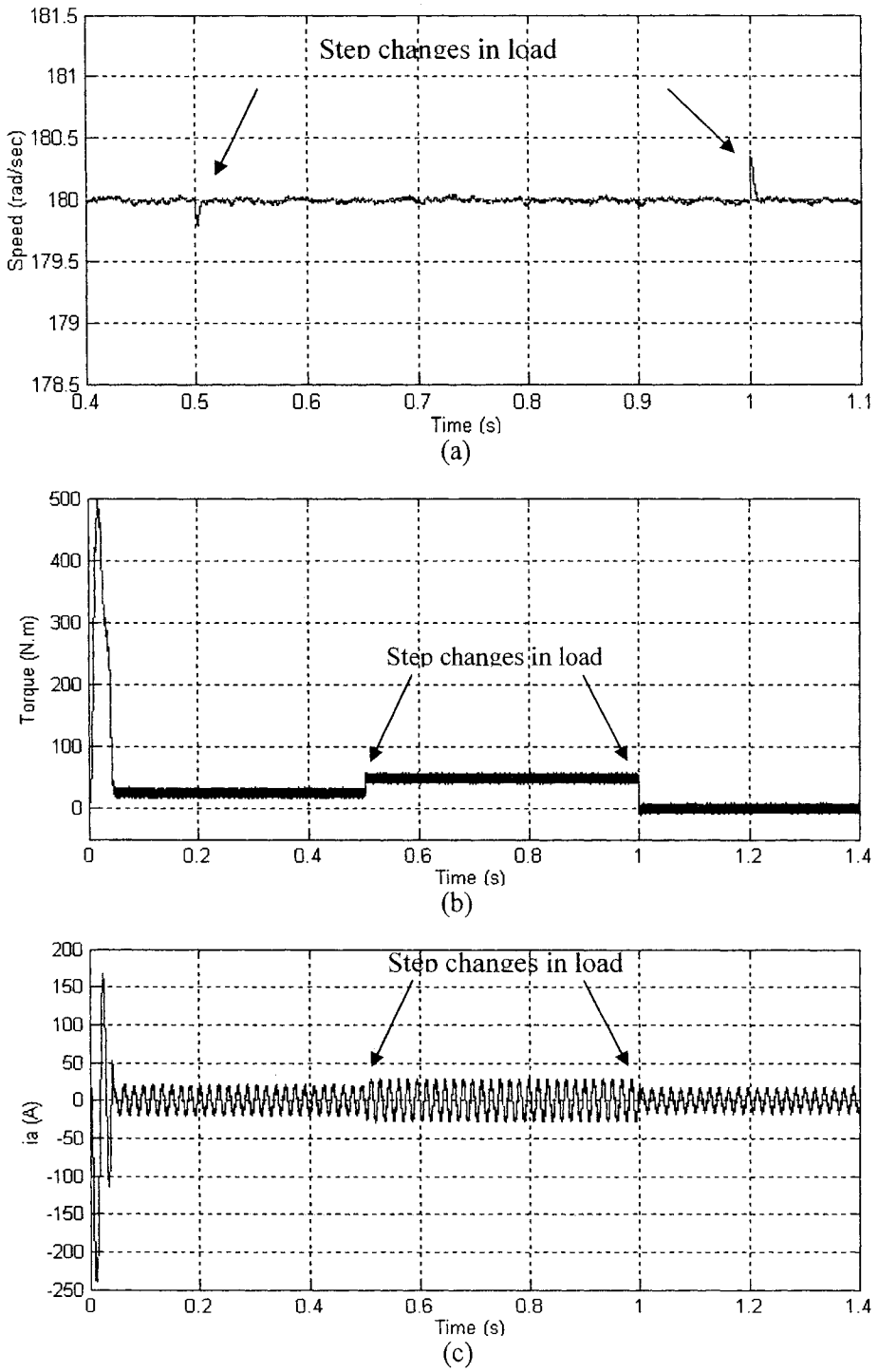

Fig. 5.12: Simulated responses of the proposed ABNC and drive at speed of 180 rad/sec with step changes in load torque (half load to full load, full load to no load): (a) speed, (b) developed torque, and (c) actual a-phase current.

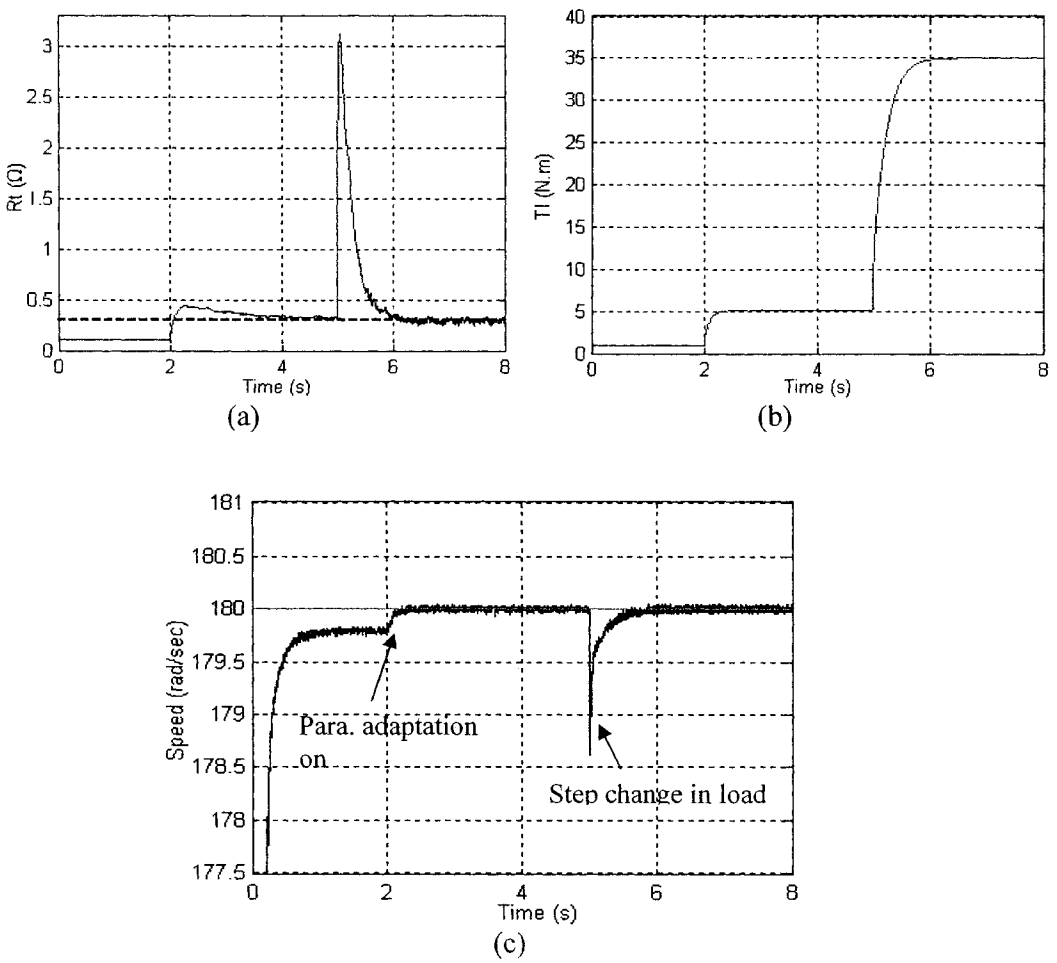

Fig.5.13: Simulated responses of the proposed ABNC and drive at speed of 180 rad/sec with step change in load torque (5 N.m to 35 N.m): (a) estimated R_t, (b) estimated T_l, and (c) speed.

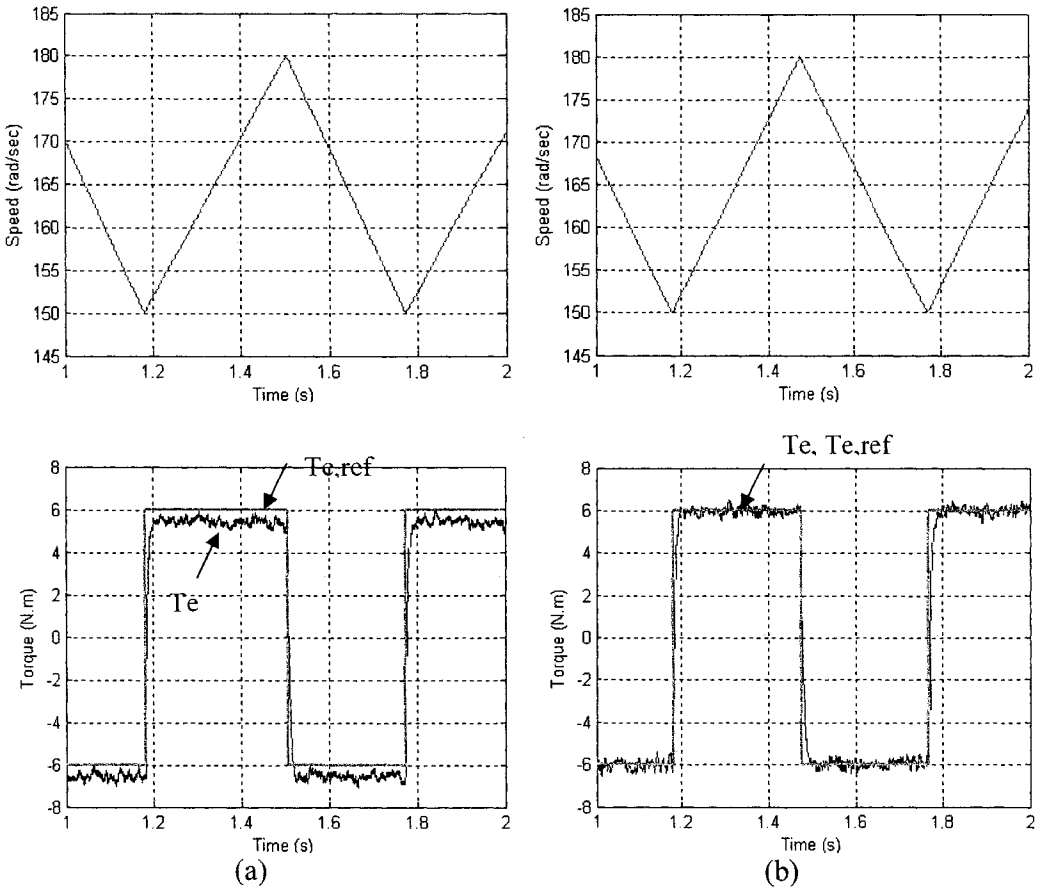

Fig.5.14: Simulated responses of the proposed ABNC and drive at torque command of 6 N.m and -6 N.m: (a) case without consideration of iron loss (b) case with consideration of iron loss.

5.2.1 Performance of LMA

The performance of the proposed LMA along with ABNC is examined. Figure 5.15 shows the responses of the speed, magnetizing current command, d and q axis currents, torque and stator currents before and after loss minimization is initiated. The simulation started with the load torque of 5 N.m and the reference speed of 180 rad/s. The loss minimization scheme is activated at t=3 s. When the loss minimization is activated, LMA calculates the optimum magnetizing current level online based on the speed and motor parameters, so that the magnetizing current reference is changed as shown in Fig. 5.15 (a). This leads to the rearrangements of i_{sd} and i_{sq} in order to maintain the same torque, which are shown in Figs. 5.15 (b) and (c), respectively. As a result of this rearrangements of i_{sd} and i_{sq}, total loss is significantly reduced as shown in Fig. 5.15 (d) while maintaining the same torque and speed. The developed torque and speed response are shown in Figs. 5.15 (e) and (f), respectively. Furthermore, it is observed that the torque ripples are significantly reduced after LMA is on while maintaining the same torque of 5 N.m. Even at the moment the LMA is activated, there is no significant drop in speed because of the filter inserted after LMA block. This filter avoids any abrupt change in the motor magnetizing current reference thus, ensure the excellent dynamic performance. Figs. 5.15 (g) and (h) show the zoom-in view of actual a- phase stator current and a, b, and c-phase currents. Significant decreases in stator currents are observed again.

Next, to exam the effectiveness of the overall system, the motor is started with wrong parameters, which causes the steady state speed error. The LMA is initiated at t=2 s, and the parameter adaptation is on at t=4 s. Figure 5.16 shows the effectiveness of both LMA and adaptation algorithms. It is observed from Fig. 5.16 (b) that when

LMA is on at t=2 s with the motor speed of 180 rad/s, the total loss has decreased significantly, but a small steady state speed error still exits due to the incorrect parameter values to the controller, which is shown in Fig. 5.16 (a). When the parameter adaptation is activated at t=4 s, the total loss has decreased even further. Moreover, the actual speed is accurately following the reference speed. From the simulation results, it is clear that the parameter adaptation not only improves the dynamic performance of the controller but also contributes to further loss minimization of the IM. The corresponding estimated parameters are shown in Figs. 5.16 (c) and (d).

Simulation is done at various speed conditions including the field weakening region with load torque of 5 N.m and simulation results are plotted and shown in Fig. 5.17. For the field weakening operation region, field weakening rule specified in Appendix B3 is used. Figs. 5.17 (a), (b) and (c) show the comparison of d, q axes current and total loss against motor speed, respectively in three different cases: 1) vector control with constant magnetizing current, 2) proposed LMA without parameter adaptation, and 3) proposed LMA with parameter adaptation. When the proposed LMA is used, a significant reduction in total loss is achieved as shown in Fig. 5.17 (c). It is also observed that when LMA is used with parameter adaptation the best results are achieved.

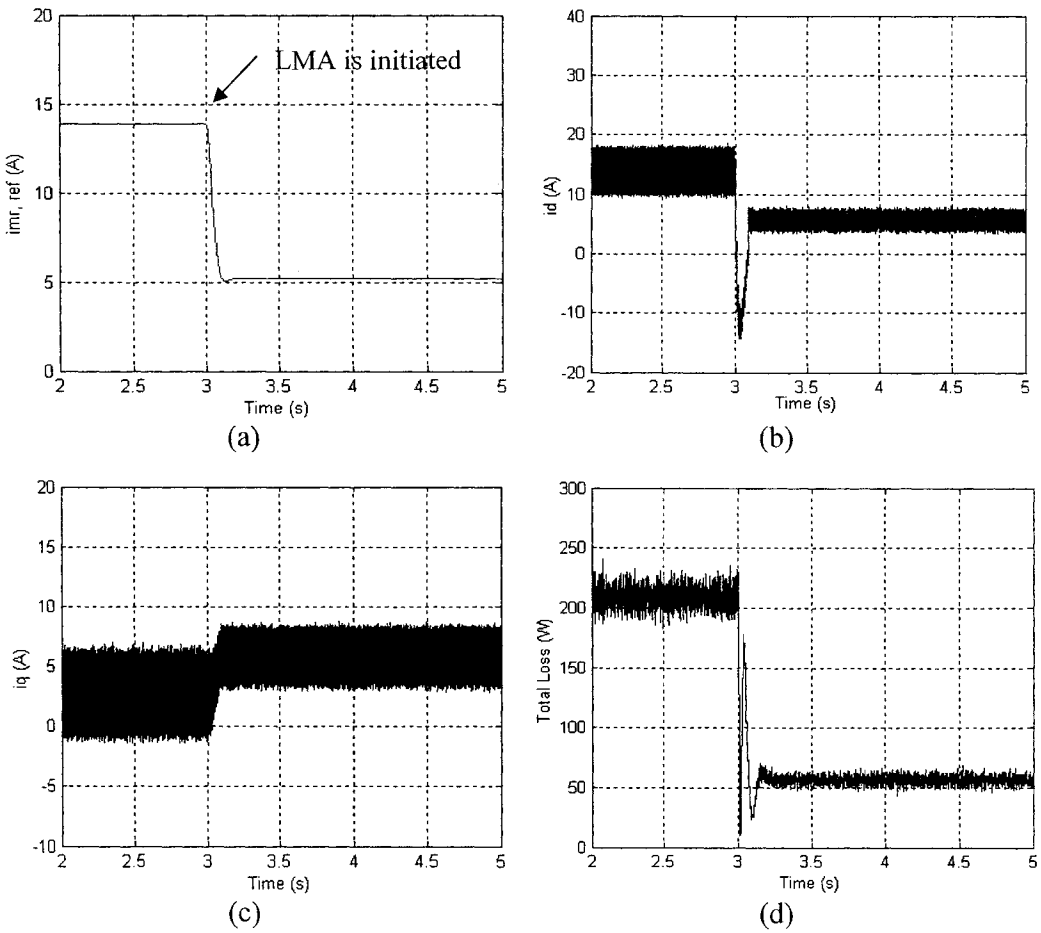

Fig.5.15: Simulated responses of the proposed ABNC and drive at speed of 180 rad/sec and load of 5 N.m: (a) magnetizing current, (b) d-axis current, (c) q-axis current, and (d) total loss before and after the LMA is on.

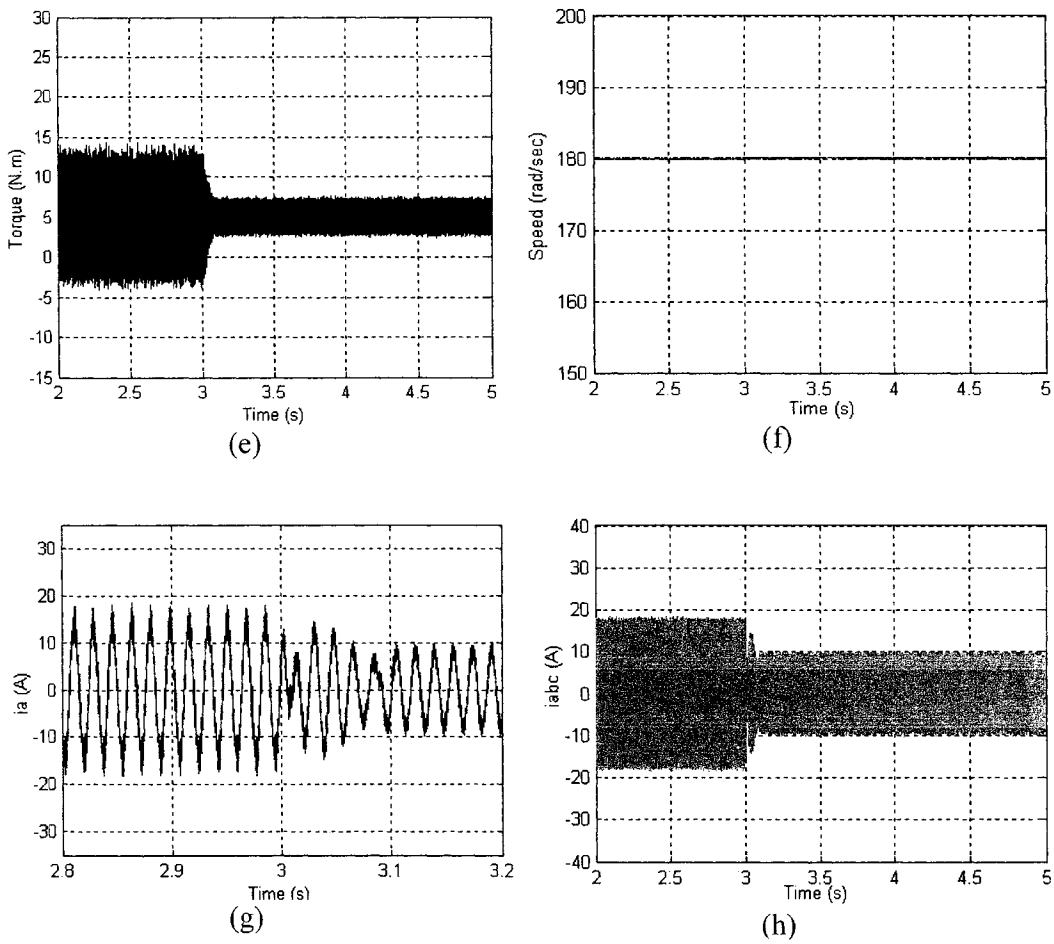

Fig.5.15 (Cont'd.): (e) developed torque, (f) speed, (g) actual a-phase current, and (h) actual a, b and c-phase current before and after the LMA is on.

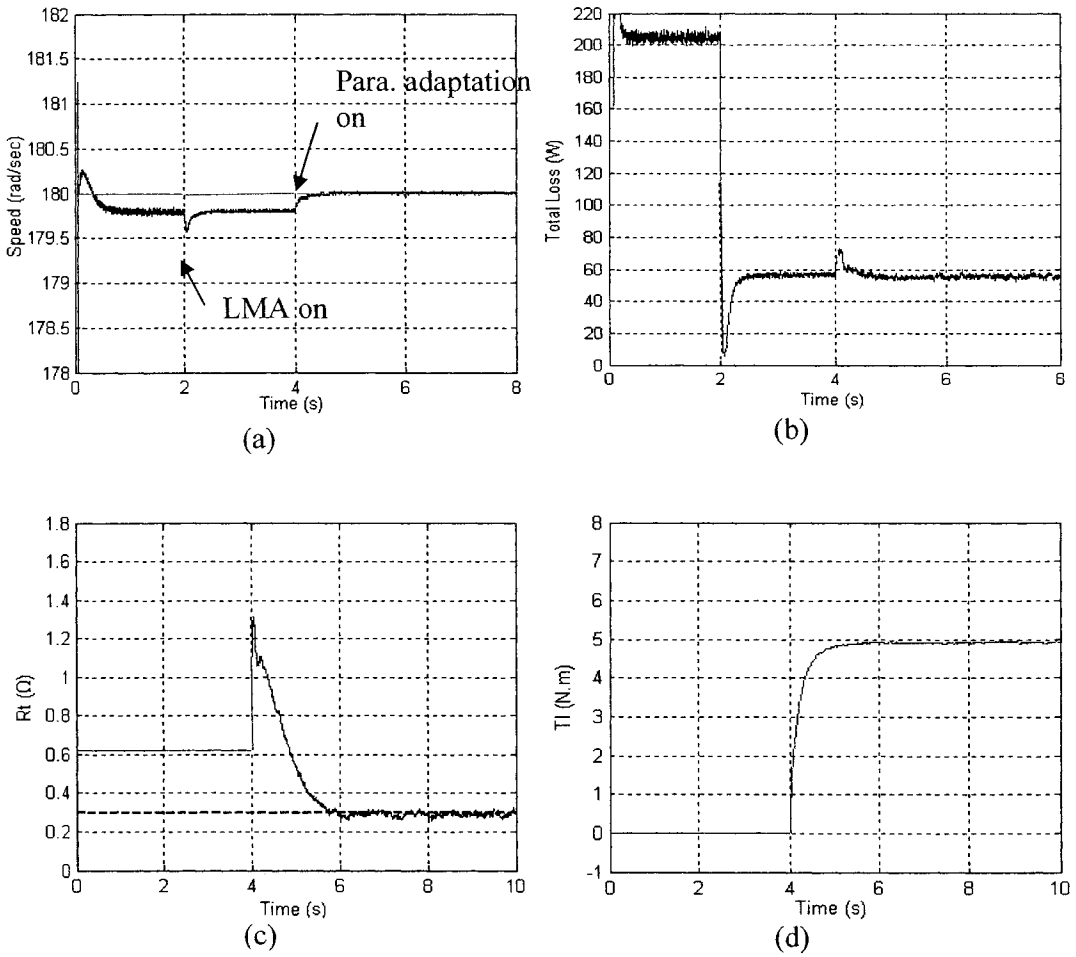

Fig.5.16: Simulated responses of the proposed ABNC and drive at speed of 180 rad/sec and load torque of 5 N.m: (a) speed, (b) total loss, (c) estimated R_t, and (d) estimated T_l when the LMA is on at t=2s and parameter adaptation in on at t=4.

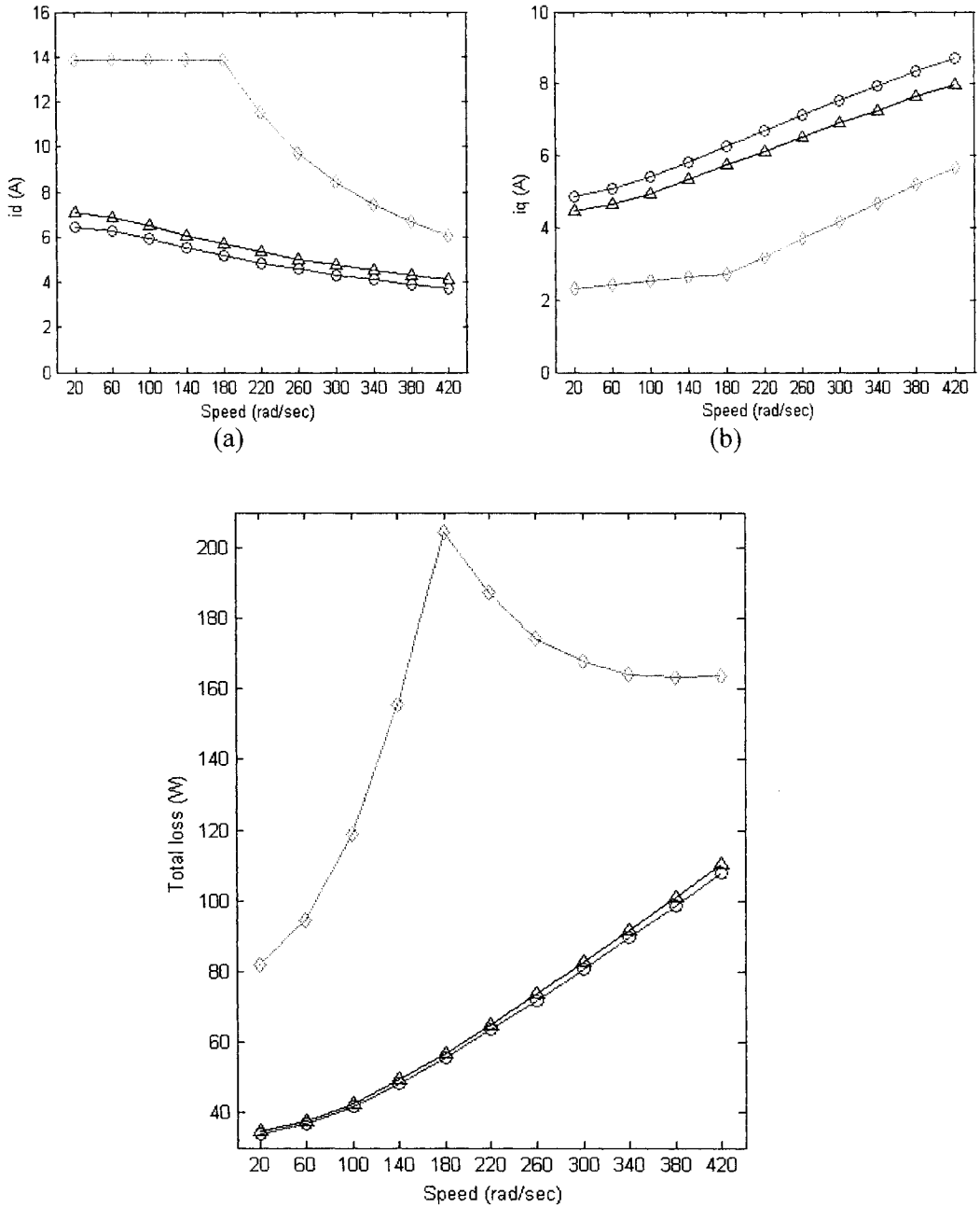

Fig.5.17: Simulated responses of the proposed ABNC and drive at speed of 180 rad/sec and load torque of 5 Nm: (a) d-axis current, (b) q-axis current, and (c) total loss for the following three cases:

(◊): vector control with constant magnetizing current

(Δ): proposed LMA without parameter adaptation

(O): proposed LMA with parameter adaptation

5.3 Concluding Remarks

A novel complete vector control scheme of an IM drive incorporating the proposed LMA and ABNC is presented in this chapter. The simulation results show encouraging performances of the proposed drive both in terms of dynamic performance and loss minimization. The simulation results validated the proposed ABNC and LMA are superior to the conventional ones. Furthermore, when they are combined together, even further loss reduction is achieved.

In order to confirm the effectiveness of the proposed ABNC based on-line loss minimization control of IM drive, the implementation of the complete vector control scheme of the drive is carried out in real-time as an integrated part of this work. The detailed experimental implementation procedures are described in the following chapter.

Chapter 6

Experimental Verification

This chapter presents the experimental implementation of a proposed IM drive system in real time using DSP controller board DS 1104 on an available experimental 1/3 hp IM for the sake of testing the proposed algorithms. The experimental setup and both hardware and software implementation are described. Extensive experimental results and discussion are also presented in order to verify the effectiveness of the proposed scheme.

6.1 Description of the Experimental Setup

The experimental setup used for the real-time implementation of the proposed ABNC based online loss minimization control of IM is shown in Fig.6.1.

The test induction motor is labeled as 'M'. The test motor is coupled to a DC machine and this DC machine's winding is connected to several variable resistances. This DC machine and variable resistances work as a mechanical load to the motor and labeled as 'D' and 'L' respectively. The rotor position of the test motor is measured by an optical incremental encoder which is labeled as 'E'. The encoder is connected to the DC machine shaft using a flexible coupler. The actual motor currents are measured through Hall-effect current sensor and connected to the interface circuit. These sensors and interface circuit are labeled as 'H' and 'I', respectively. A base

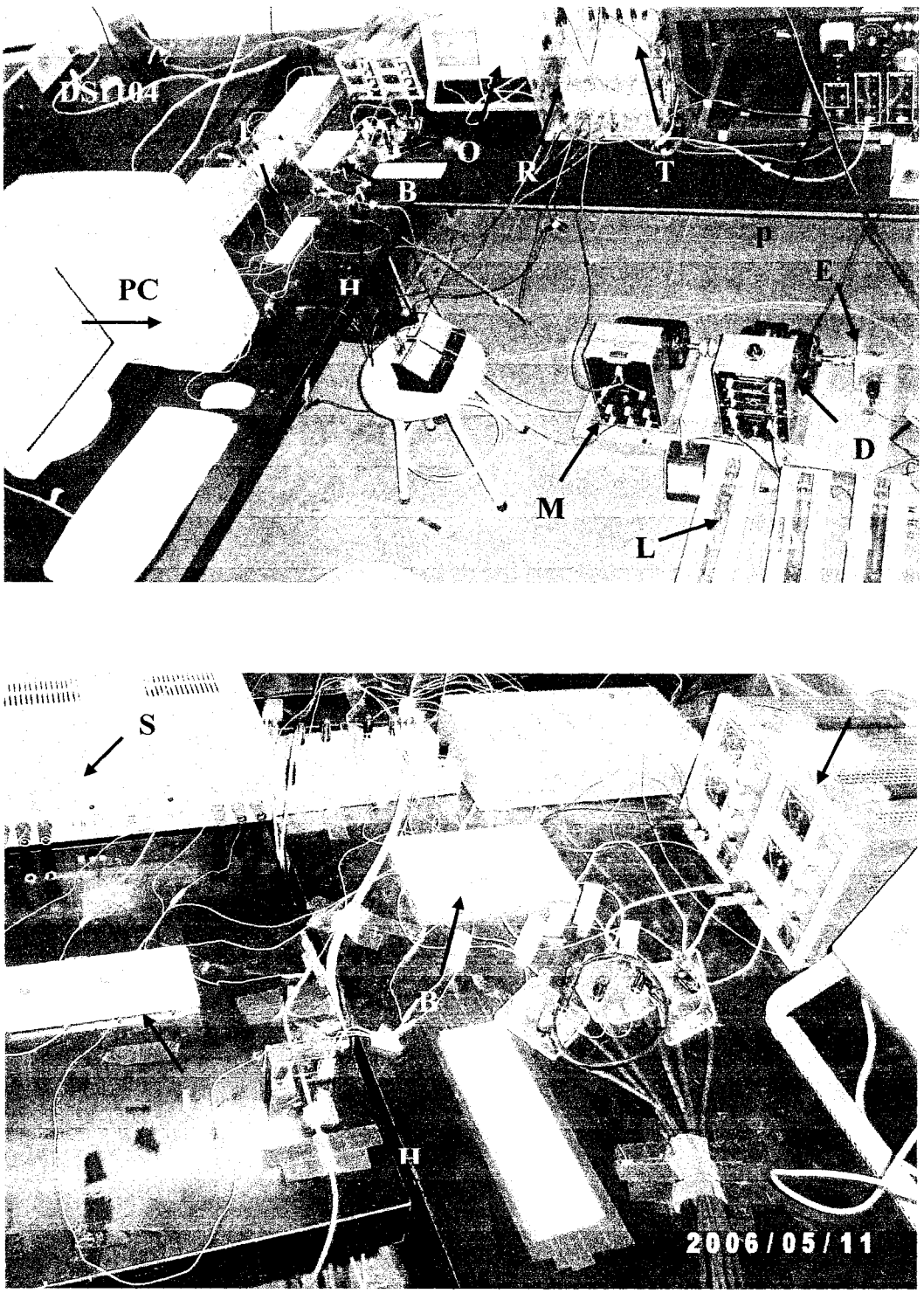

Fig.6.1: Experimental setup for the proposed IM drive. The labeled components are referred to in Section 6.1.

drive circuit is used to increase the power level of the firing pulses so that these are sufficient to drive the inverter switches. The base drive circuit also provides isolation between the low power control and the high power supply circuits. In Fig. 6.1 the base drive circuit is labeled as 'B'. The power circuits consist of a 3-phase (6-pulse) insulated gate bipolar transistor (IGBT) inverter, variable AC power supply and a rectifier. The 3-phase inverter module is labeled as 'T'. This inverter has Active Security feature against short-circuit and under-voltage of the power supply as well as built-in thermal protection which prohibits destructive heatsink temperatures. The DC bus voltage for the voltage source inverter (VSI) is obtained by rectifying the AC voltage. The variable AC power supply module is labeled as 'P' and the rectifier is labeled as 'R'. The personal computer, in which the DSP board DS1104 is installed, is labeled as 'PC'. A digital storage oscilloscope is used to capture the desired signals coming out through D/A port of the DSP board. The oscilloscope is labeled as 'O'. All other DC power supplies are labeled as 'S'.

6.2 DSP-Based Hardware Implementation

The DSP controller board DS 1104 [45-46] is used for the real time implementation of the proposed IM drive system. The board is installed in an Intel PC with uninterrupted communication through dual port memory. The block diagram of the DSP board is shown in Fig.6.3. The DS1104 board is mainly based on a PowerPC type PPC603e processor. This processor operates at the clock of 250 MHz with 32 KBytes cache. This board has a 32 MBytes of SDRAM global memory and 8 MBytes of flash memory. The DSP is supplemented by a set of on-board peripherals used in digital control systems including analog to digital (A/D), digital to analog (D/A) converters and digital incremental encoder interfaces. This board is also equipped

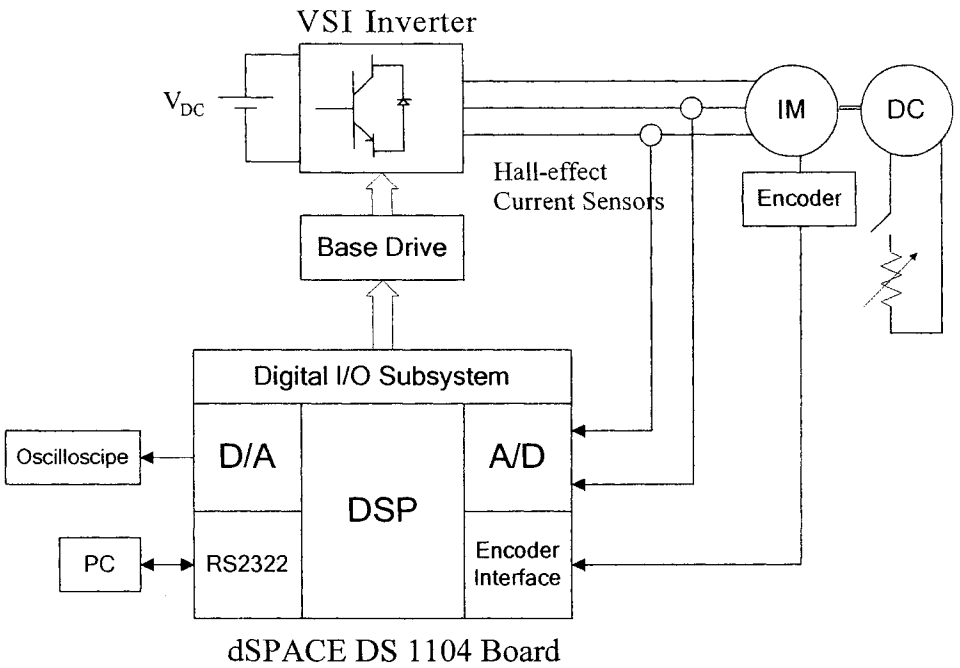

Fig.6.2: Hardware schematic for experimental implementation of the IM drive

with a Texas Instruments TMS320F240 16-bit micro controller DSP that acts as a slave processor and provides the necessary digital I/O ports and timer function such as input capture, output capture and PWM generation. In this work, the slave processor is used only for digital I/O configuration. The actual motor currents are measured by the Hall-effect sensors, which have current range of 0 to $\pm$ 200 A and a frequency range of DC to 250 KHz. The output current signal of these sensors is converted to a voltage by connecting a resistor between output of the sensor and ground. Output voltage can be scaled by selecting various resistor values, and fed to the DSP board through the A/D converter. In the thesis, in order to reduce the effect of noise in measurement, the output voltages of current sensors are boosted through interface circuits, which is a non-inverting amplifier with the chip LM741CN as shown in Appendix B. As the motor neutral is not grounded, only two phase currents are measured and fed back to the DSP board and the other phase current is calculated

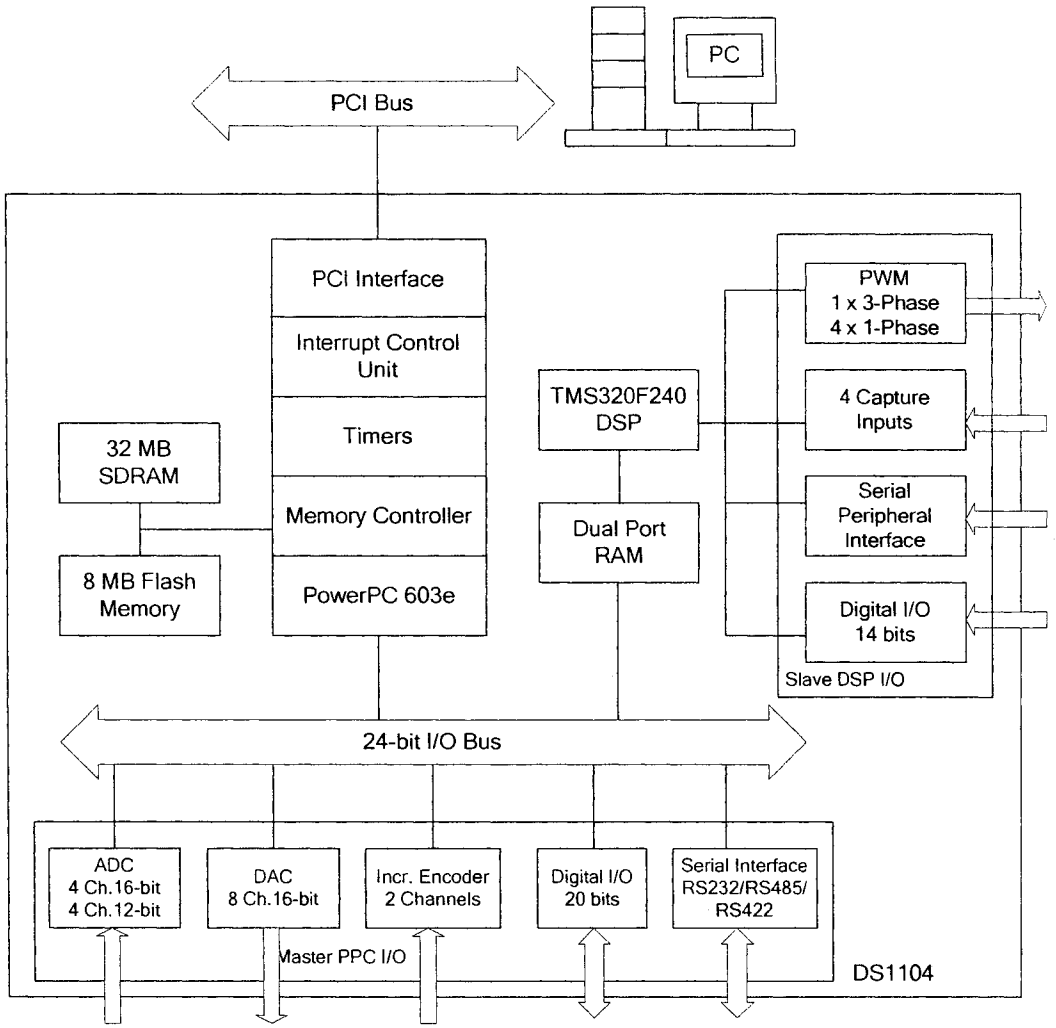

Fig.6.3: Block diagram of the DS-1104 board

from them. The rotor position angle is measured by an incremental encoder connected to the DC machine shaft and fed to the DSP board through the encoder interface. The encoder used in this work generates 1000 pulses per revolution, which means a resolution of $0.36°$. These pulses are fed to the one of two digital incremental encoder interface channels of the board. A 24-bit position counter is used to count the encoder pulses and is read by a calling function in the software. The counter is reset once per revolution by the index pulse generated from the encoder.

The command voltages are generated from the ABNC and compared with the carrier wave. This generates the logic signals which act as firing pulses for the inverter switches. Thus, these six logic signals are the output of the DSP Board and are fed to the base drive circuit of the IGBT inverter power module. The main function of the drive circuit is to generate six pulses having proper voltage level for the six IGBTs of the inverter. The outputs of the digital I/O subsystem of the DS 1104 are six pulses with a magnitude of 5 V. This voltage level is not sufficient for the gate drive of IGBTs. Therefore, the voltage level is shifted from +5 V to +15V through the base drive circuit with the chip SN7407N as shown in Appendix B.

6.3 Software Development for real-time implementation

The dSPACE DS1104 board is a self contained system, not an embedded system. This means the board installed in the lab computer through a PCI slot is its own entity and none of the processing for a system implemented on the board is done by the host PC. As a result, the board requires that software be created and downloaded to the board for the system to function.

As a first step for the implement of the proposed control algorithm, a real-time Simulink model for the complete drive system is developed and the dSPACE program code in ANSI 'C' is generated from it by the real-time workshop (RTW). The real-time Simulink model for the proposed control scheme is shown in detail in Appendix D. Then, ControlDesk software is used to download software to the DSP board, start and stop the function of the DS1104 as well as create a layout for interfacing with global variables in dSPACE programs. The sampling frequency used in this work is found to be 10 kHz. If the sampling frequency that is higher than 10 kHz is chosen, the 'overrun error' occurs, which indicates too much computational burden to the processor.

The flow chart of the software is shown in Fig.6.4. After initializing all the required variables, the timer interrupt routine is set up to read the values of the currents and rotor position angle every $100\,\mu s$.

The motor currents obtained through analog to digital converter (ADC) channel 1 and 2 are multiplied by the gain 7.1429 and 6.6667, respectively in order to obtain the actual current values in software. These constants depend on the Hall-effect sensors specifications and the resistors used in the interface circuit. After these digitalized currents in *abc* coordinates are converted into rotating reference frame of *dq* coordinates, the magnetizing current, i_{mr} is estimated.

The incremental encoder interface on the DS 1104 board consists of a 24-bit up/down counter to count the shaft encoder pulses, which is 1000 per revolution in this work. The index pulse is generated by the encoder to reset the counter to zero each revolution, which means that the maximum rotor angle equals 2π. Therefore, the rotor position angle can be calculated in radian by the equation of $2\pi/1000$. Once the rotor position angle is calculated, the rotor speed is computed from the measured

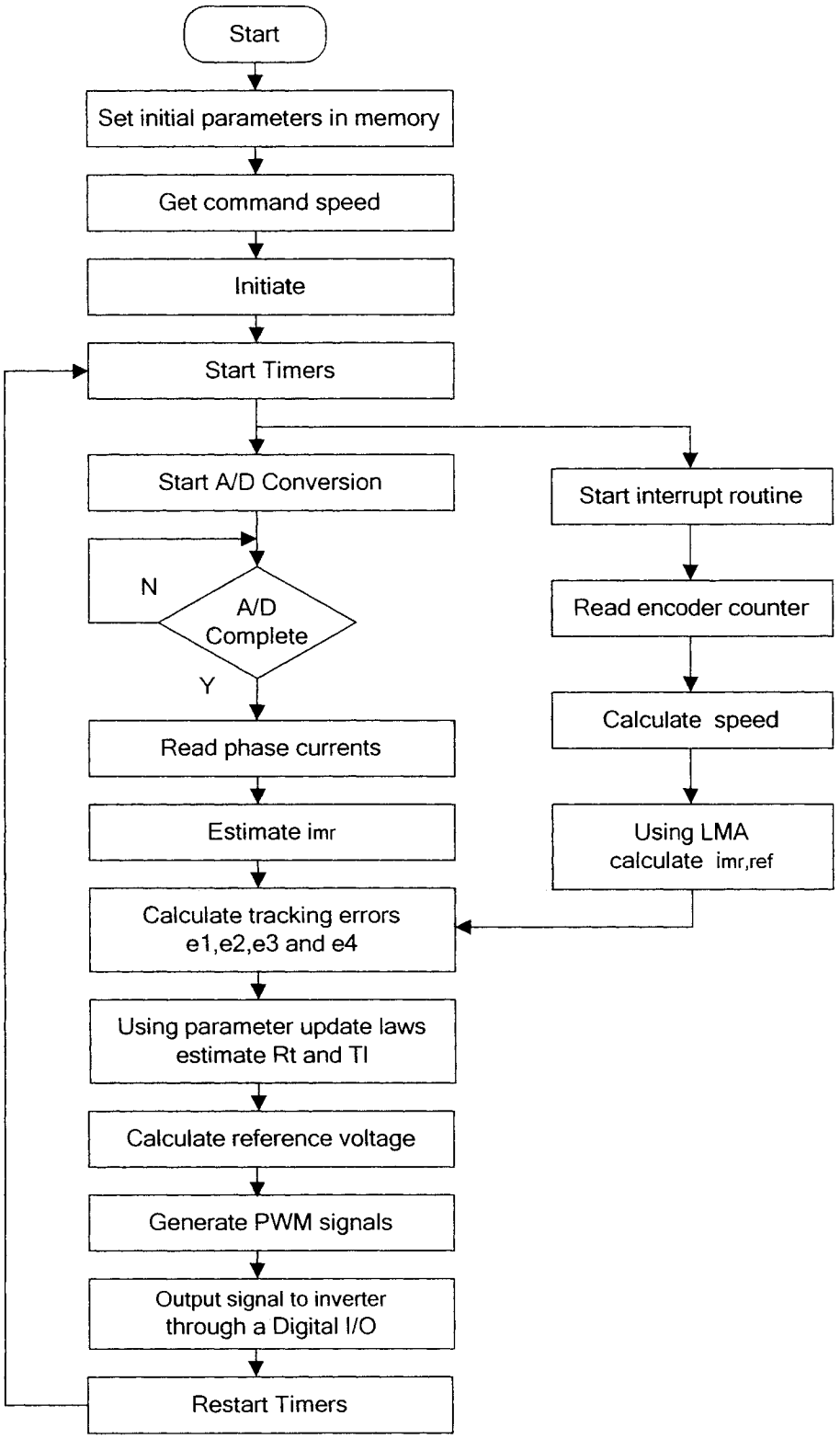

Fig.6.4: Flow chart of the software for real time implementation of the adaptive backstepping based online loss minimization control of IM.

rotor position angels using numerical backward differentiation. Based on the calculated speed, the magnetizing current reference, $i_{mr,ref}$ for the minimum loss operation of IM is calculated according to the proposed LMA.

All the calculated and measured values as explained above such as d, q-axes currents, rotor speed, $\hat{i}_{mr}$ and $i_{mr,ref}$ along with initial parameters stored in memory compute the tracking errors e_1, e_2, e_3 and e_4. Based on these tracking errors, parameter R_t and T_l are estimated by the parameter update laws developed in Chapter 4. These newly estimated parameters will be used in the routine of control loop until next parameter adaptation occurs.

The reference voltages are calculated according to the developed control algorithm in Chapter 5 using all the necessary variables obtained above and updated parameters. Lastly, the reference voltages are compared with the triangular carrier signal (1.2 kHz) to generate the six PWM pulses for the inverter switches. All off-to-on transitions of the PWM pulses are delayed by the dead time of 0.5×10^{-3} second in order to prevent the shorting of the voltage bus to ground. These pulses are sent to the inverter base drive through a Digital I/O subsystem in the board.

6.4 Design of PI Controller for the Further Investigation of the Proposed LMA

In order to compare the proposed LMA with the conventional LMA used in [22], PI controllers are designed for speed and magnetizing current control. The inputs to the PI controllers are the speed and magnetizing current errors and the outputs are the q-axis command current $i_{sq,ref}$ and d-axis command current $i_{sd,ref}$. These command

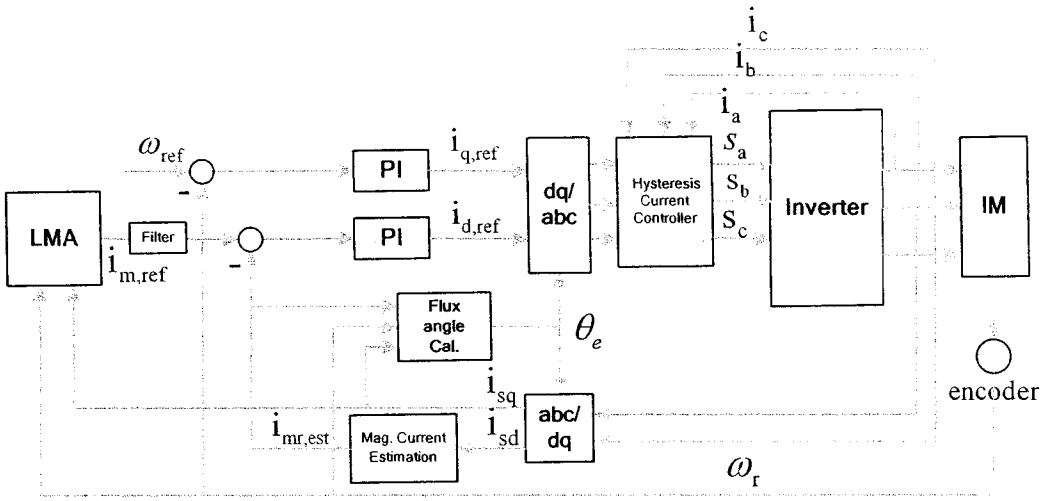

Fig.6.5: Block diagram for PI based speed and the magnetizing current control.

currents are transformed into *abc* coordinates and fed to the hysteresis controller, where the command currents are compared with the measured a, b, and c-phase stator currents to generates the PWM logic signals as explained in Chapter 5. The proportional gains and integral gains are chosen to be 0.06 and 0.25 for speed control and 0.35 and 0.65 for flux control respectively by trial and error in order to achieve reasonable settling time, overshoot and zero steady state error. Block diagram for PI controller is shown in Fig.6.5.

6.5 Experimental Results and Discussion

6.5.1 Performance of ABNC

Experimental tests are carried out to verify the effectiveness of the proposed scheme at different operation conditions on 1/3 hp motor. This is smaller motor than the one in Simulation, but was the only IM available in the laboratory. The detailed

IM parameters used in the experiment are given in Appendix A. The controller gains, k_1, k_2, k_3 and k_4 are chosen as 500, 1100, 200 and 300 respectively.

First, the performance of the proposed ABNC has been investigated. Figure 6.6 shows the speed and magnetizing current response for the reference speed of 180 rad/s at 34% of the rated load. The supplying voltage from Power Supply to the motor is increased to the rated voltage level as rapidly as possible to start the motor and this results in slower starting response as compared to the ideal simulation results. The actual speed converges to the reference speed in a short time with minimum overshoot and nearly zero steady state error. Fig.6.6 (b) shows the magnetizing current response which also converges to the reference value in a very short period with minimum oscillation.

Figures 6.7 (a) to (d) show the corresponding tracking error e_1, e_2, e_3 and e_4 defined in the backstepping design which all successfully converge to 0. Therefore, the control objectives of the proposed ABNC are met. The experimental results in Fig.6.6 and Fig.6.7 show that the proposed ABNC based system is capable of running the motor with almost no overshoot and zero steady-state error at a rated command speed.

The performance of the drive is also investigated for a sudden change of command speed. Figs.6.8 (a) and (b) show the speed response for a step increase in command speed (from 50 rad/s to 150 rad/s) and a step decrease in command speed (180 rad/s to 130 rad/s), respectively at about 34% of the rated load. In the case of a sudden increase in command speed as shown in Fig.6.8 (a), the speed follows the command speed smoothly with zero steady-state error and almost no overshoot. Fig.6.8 (b) shows the case of a sudden decrease in the command speed. A small

undershoot and oscillation are observed, but the speed quickly settles to the command speed without steady state error.

In practical industrial applications, the sudden change of load is a common phenomenon. The speed responses for a sudden increase in load are shown in Fig.6.9. In Fig.6.9 (a), the motor is running at a light load condition without the parameter adaptation and after some time suddenly about the 40% of the rated load is applied to the motor. When the parameter adaptation is not used, the motor speed drops by about 25 rad/sec and cannot recover to the command speed showing the significant steady state speed error. Since the parameter is fixed in the controller, the deviation of actual load torque will produce an error in speed. However, when the parameter adaptation is used, it is shown in Fig. 6.9 (b) that the speed error caused by the load torque disturbance is quickly recovered to the command speed. Fig. 6.9 (c) shows the estimation of the load torque. It does not converge to the true value in this experiment, but effectively compensates the speed controller so that speed converges back to the command speed.

Figure 6.10 shows the estimation of the rotor resistance when the motor is started with no parameter adaptation and the wrong parameter value of R_r, and after some time a parameter adaptation is activated. This parameter convergence is tested with the different initial values, i.e. an initial value of 5 Ω for Fig.6.10 (a) and 2 Ω for Fig.6.10 (b). In both cases, the successful parameter adaptation results are obtained.

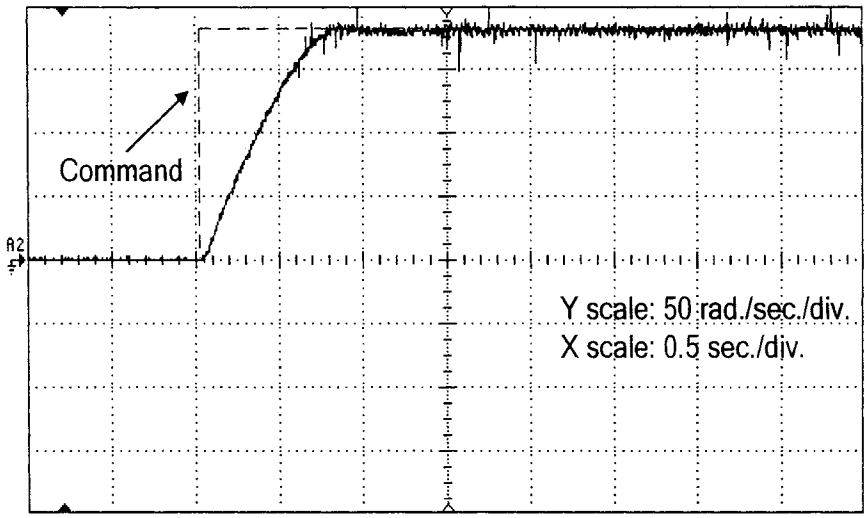

(a)

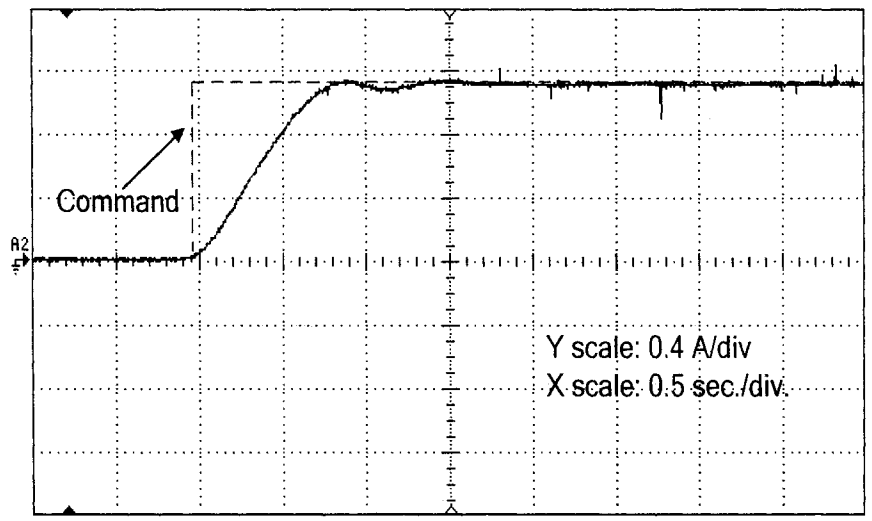

(b)

Fig.6.6: Experimental responses of the proposed ABNC and drive at 34 % of the rated load and speed of 180 rad/sec: (a) speed, (b) magnetizing current.

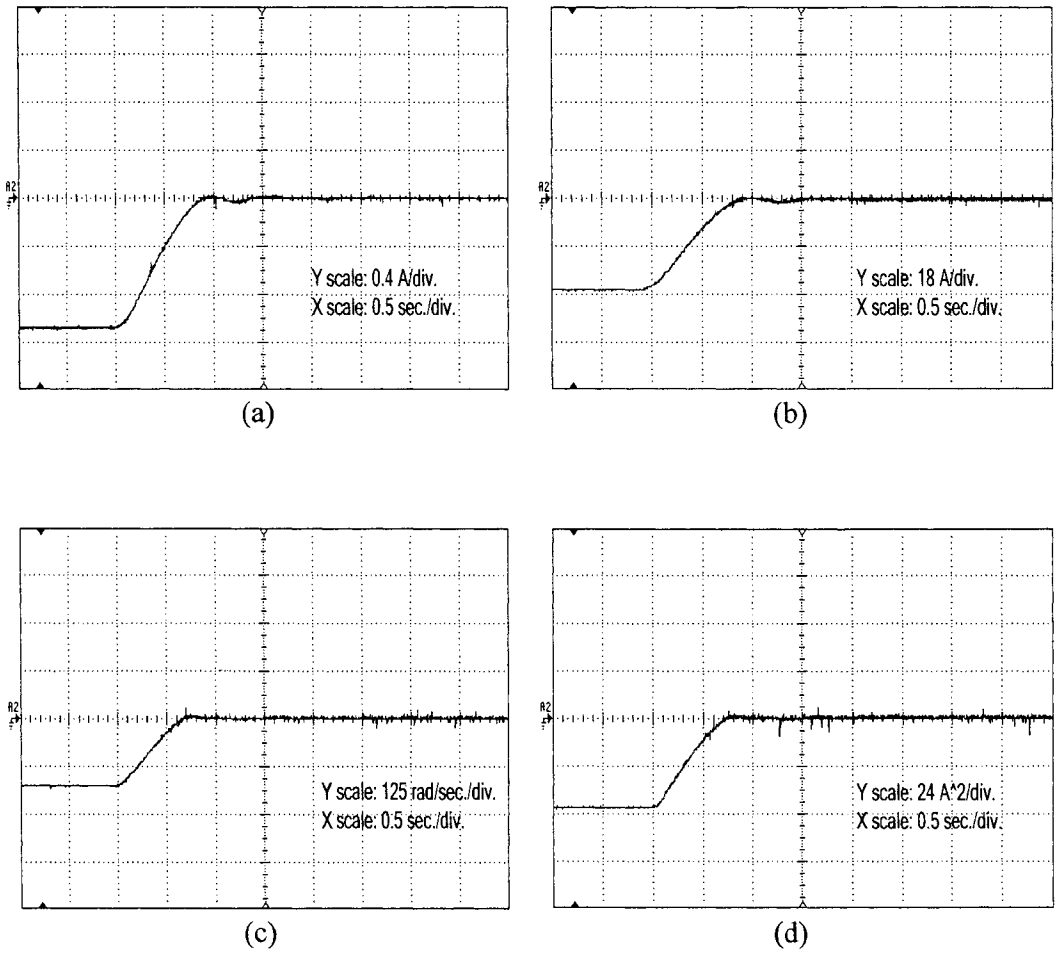

Fig.6.7: Experimental responses of the proposed ABNC and drive at 34 % of the rated load and speed of 180 rad/sec: (a) magnetizing current tracking error ($e_1 = i_{mr} - i_{mr,ref}$), (b) d-axis current tracking error ($e_2 = i_{sd} - i_{sd,ref}$), (c) speed tracking error ($e_3 = \omega_m - \omega_{ref}$), and (d) torque related tracking error ($e_4 = i_{mr} i_{sq} - (i_{mr} i_{sq})_{ref}$).

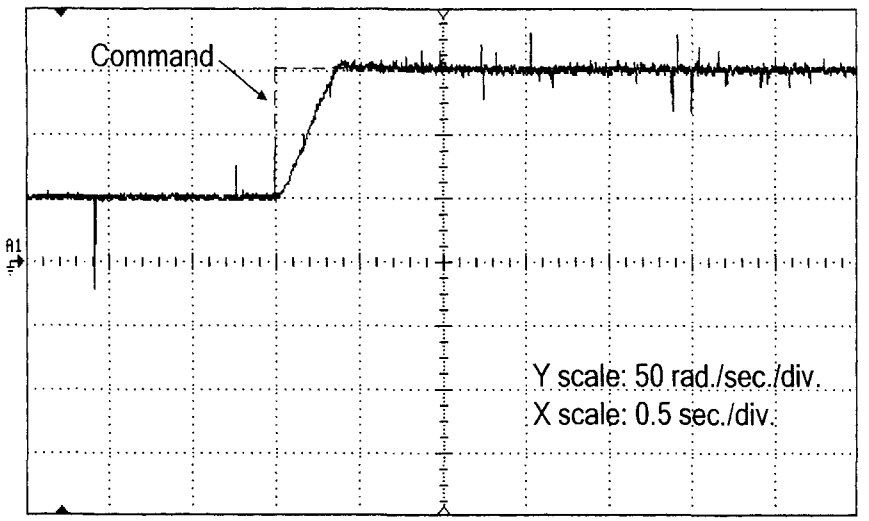

(a)

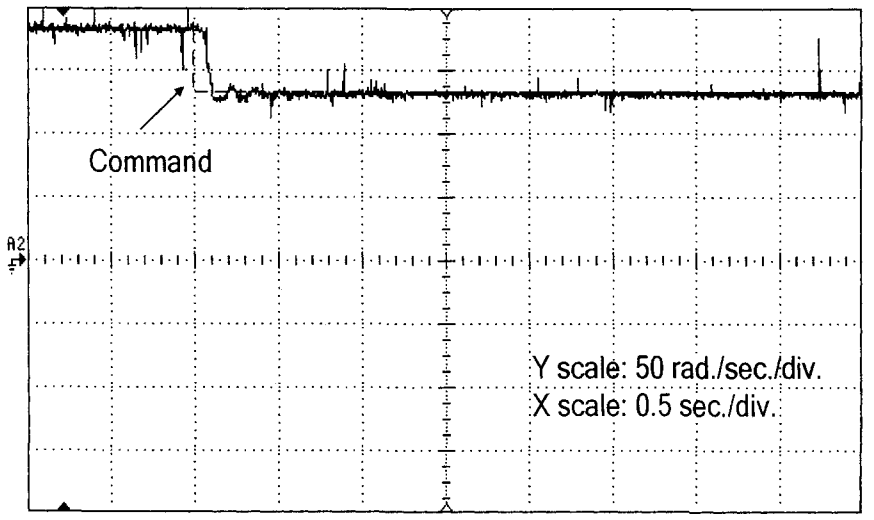

(b)

Fig.6.8: Experimental speed responses of the proposed ABNC and drive at 34% of the rated load with step changes in command speed: (a) 50 to 150 rad/sec and (b) 180 to 130 rad/sec.

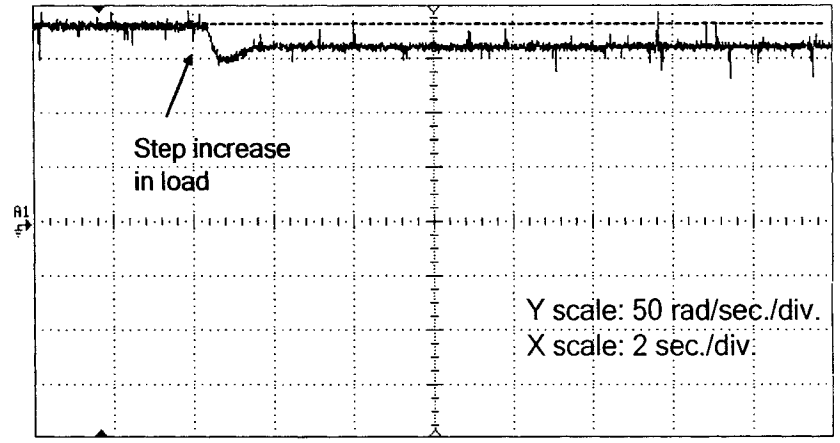

(a)

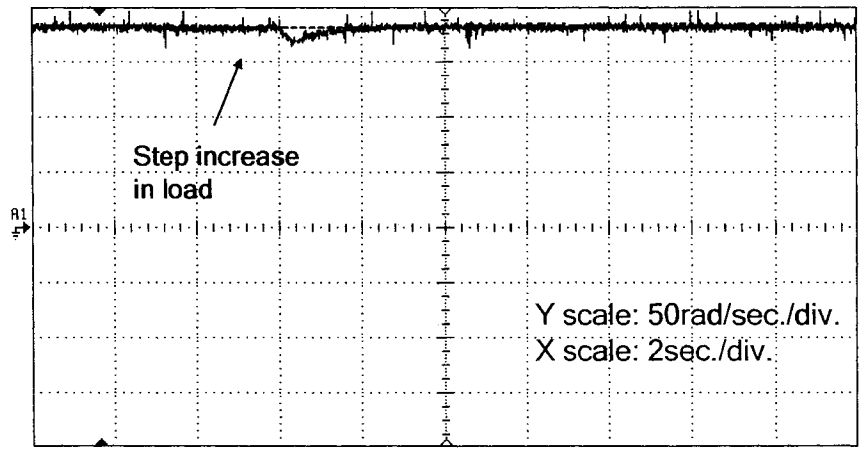

(b)

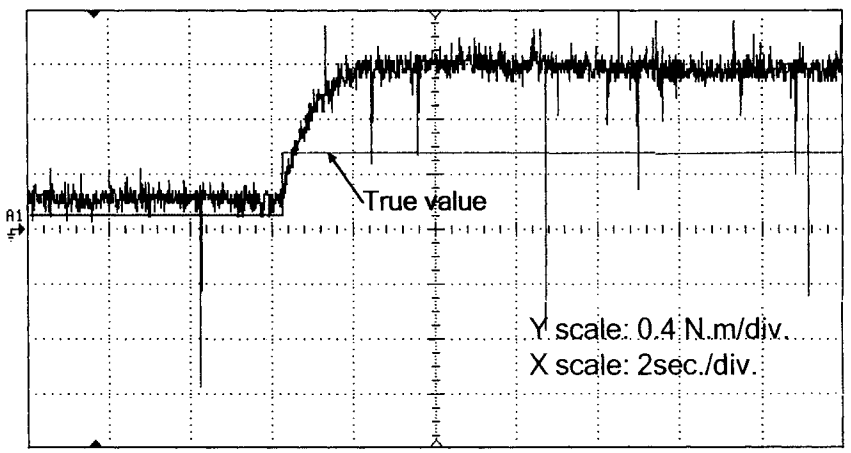

(c)

Fig.6.9: Experimental responses of the proposed ABNC and drive at speed command of 180 rad/sec with a step change in load torque (inertia load to about 40% of the rated load): (a) speed response without parameter adaptation, (b) speed response with parameter adaptation, and (c) estimated load torque.

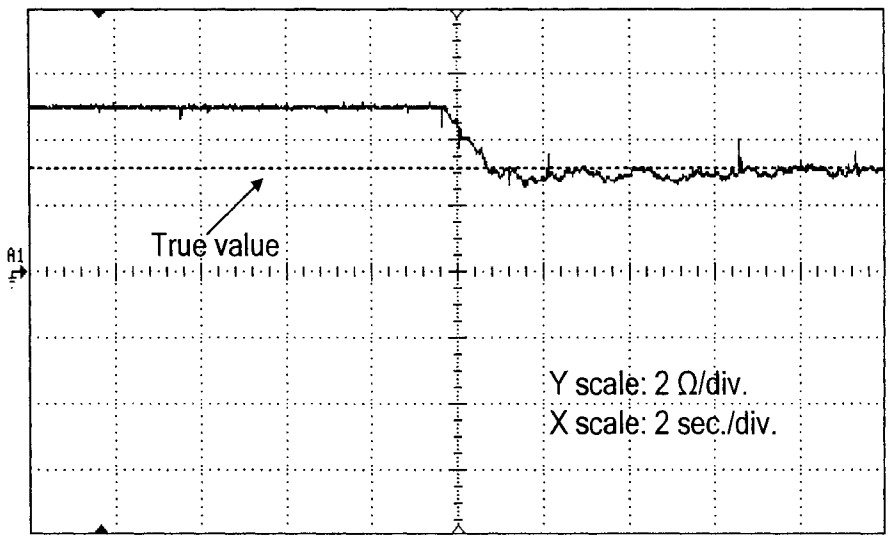

(a)

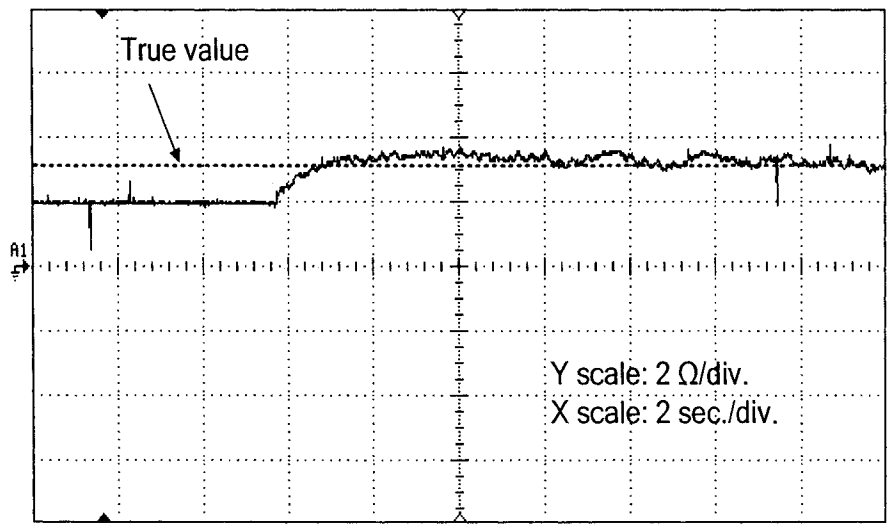

(b)

Fig.6.10: Experimental responses of the proposed ABNC and drive at speed of 180 rad/sec and 16% of the rated load: (a) estimated R_t with stating point at $5\,\Omega$ and (b) estimated R_t with starting point at $2\,\Omega$.

6.5.1 Performance of LMA

Next, the effectiveness of the proposed LMA is investigated. The motor is operated at 180 rad/sec with about 16% of the rated load torque for some time, then LMA is initiated. Fig.6.11 shows the changes of magnetizing current command, d and q axis current, actual a-phase current, total loss, developed torque and total loss before and after LMA is initiated. As expected, the magnetizing current command is reduced when the LMA is on, which is shown in Fig.6.11 (a). This leads to the rearrangement of d and q axis stator current as shown in Fig.6.11 (b) and (c), respectively. The total loss is calculated using equation (3.47) in Chapter 3 and measured in real time through the digital filters. Fig.6.11 (d) shows the significant total loss drop achieved by the proposed LMA. It is shown that the developed torque and speed remains same regardless of activation of LMA as shown in Fig.6.11 (e) and (f) while actual a-phase current and total loss are reduced, which is shown in Fig.6.11 (g). It is also observed that the proposed LMA contributes to the decrease of torque ripple too.

In order to verify the effectiveness of the proposed LMA under various conditions, the measurement of total loss is repeated at different speeds and load torques. Fig.6.12 (a), (b) and (c) show the experimental result of total loss before and after the LMA is on at 16%, 22% and 34% of the rated load torque respectively. In all three cases, the most total loss reduction is observed at the rated speed. This is because in a conventional vector control, the magnetizing current is controlled at constant value up to the rated speed. It is also found that as the load torque increases the effect of LMA in loss reduction is less. For instance, there is about 30 W of total loss reduction at 180 rad/sec of rotor speed and 16 % of the rated load torque as shown in Fig.6.12 (a) while about 23 W of total loss is observed at the same speed and 34% of the rated

load torque as shown in Fig.6.12 (c). From Fig.6.10 and 6.11, the effectiveness of the proposed LMA is proven at various speed and load torque conditions and it is also concluded that the most total loss reduction can be achieved at the rated speed with light load conditions.

Fig.6.13 investigates the effect of parameter adaptation on LMA. The motor is started with LMA on, but wrong parameter value of R_t. After some time, the parameter adaptation is activated. Y1 and Y2 in Fig. 6.13 (a) show the calculated total loss and estimated R_t, respectively at 180 rad/s with 16% of the rated load. As the estimation of R_t converges to the true value, slight reduction in calculated total loss is observed. Fig.6.13 (a) also shows loss reduction in total loss, where the motor is operating at 150 rad/sec. Fig.6.13 (c) is the plotted simulation results at different speed levels for three cases: 1) vector control with constant magnetizing current (Δ), 2) proposed LMA without parameter adaptation ($\times$), and 3) proposed LMA with parameter adaptation ($\bigcirc$). It is shown that when parameter adaptation is used with LMA the minimum total losses are achieved in all speed conditions.

Lastly, Figure 3.6 in Chapter 3 showed that the proposed LMA has a smaller Loss Factor (LF) than the traditional one used in [22] in all speed ranges. In order to verify that this smaller LF results in more loss reduction over the conventional LMA in real time and test the effectiveness of the proposed LMA as stand alone, it is combined with PI based controller as shown in Fig.6.5 and its performance is investigated. The experiments of the traditional LMA and the proposed one are done in exactly same conditions except for the loss minimization block, which generates the magnetizing current level for the minimum loss operation of an IM. To exclude the effects of temperature change on motor, motor was operated for a set period of time, the loss was measured, and then completely cooled down before the next run. Figure 6.14 (a)

shows the experimental results of total loss with/without the proposed LMA in the PI based drive. The significant total loss reduction is attained when the proposed LMA is used. Fig.6.14 (b) shows the experimental results of extra loss reductions in percentage over the conventional scheme at different speeds. Total losses are measured three times at each operation of speed and the average is calculated. The total loss difference between the conventional LMA and the proposed LMA is not significant. However, the proposed LMA exceeds the expectation of the conventional LMA in all speed ranges while there was no difference in the dynamic performance of the controller.

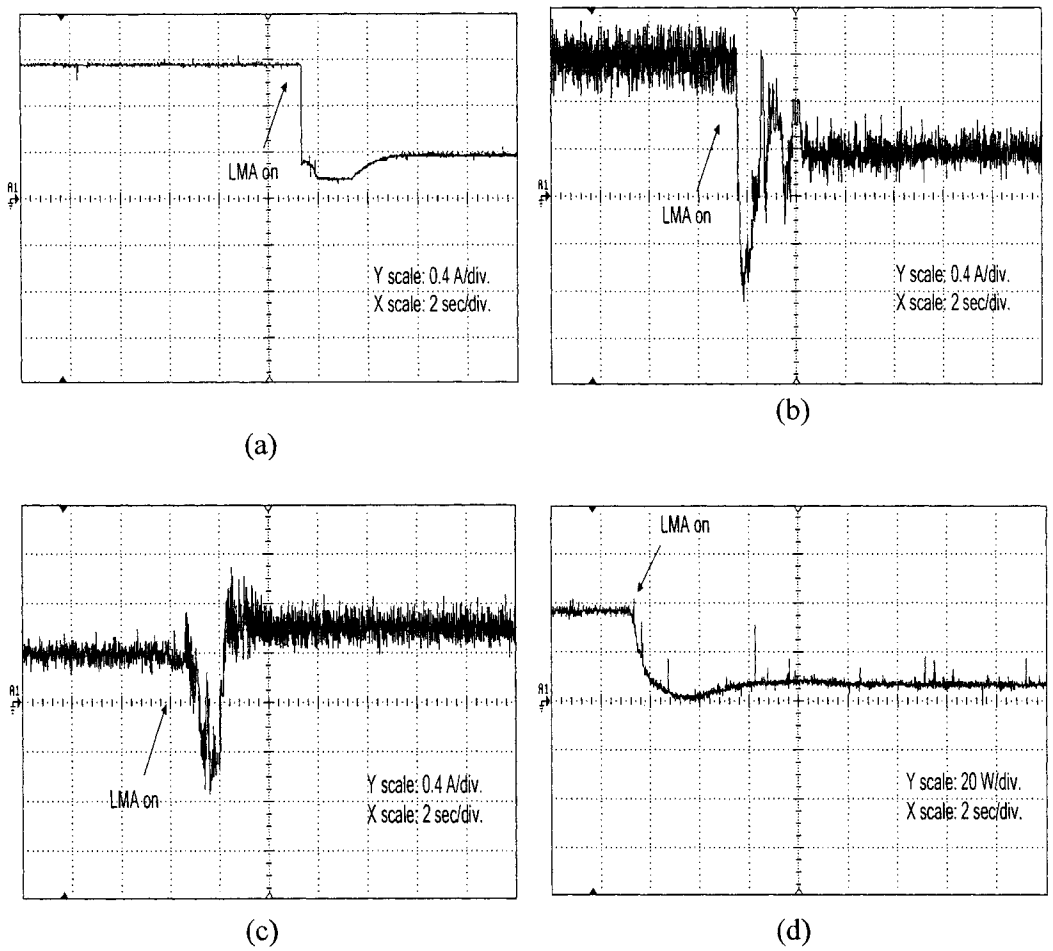

Fig.6.11: Experimental responses of the proposed ABNC and drive at speed of 180 rad/sec and 16% of the rated load: (a) magnetizing current, (b) d-axis current, (c) q-axis current, and (d) total loss before and after the proposed LMA is on.

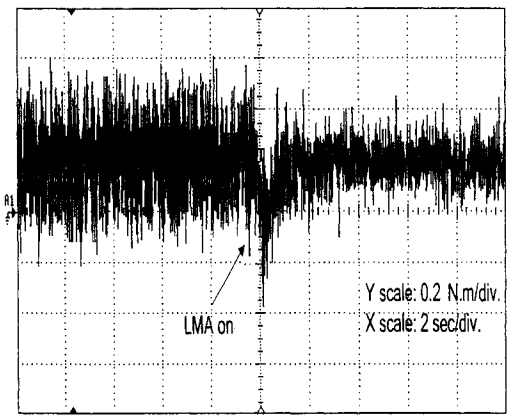

(e)

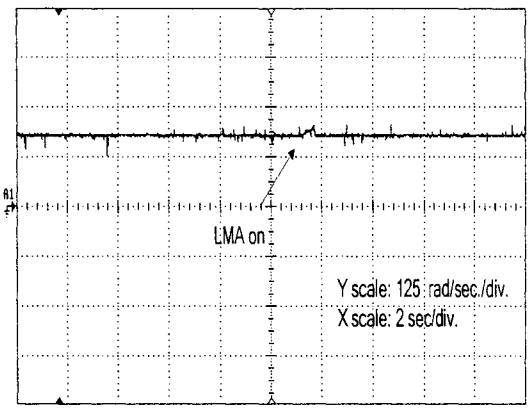

(f)

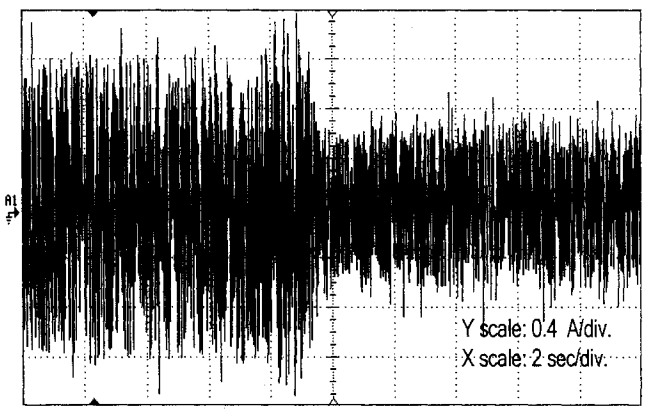

(g)

Fig.6.11 (Cont'd): (e) developed torque, (f) speed and (g) actual a-phase current before and after the proposed LMA is on.

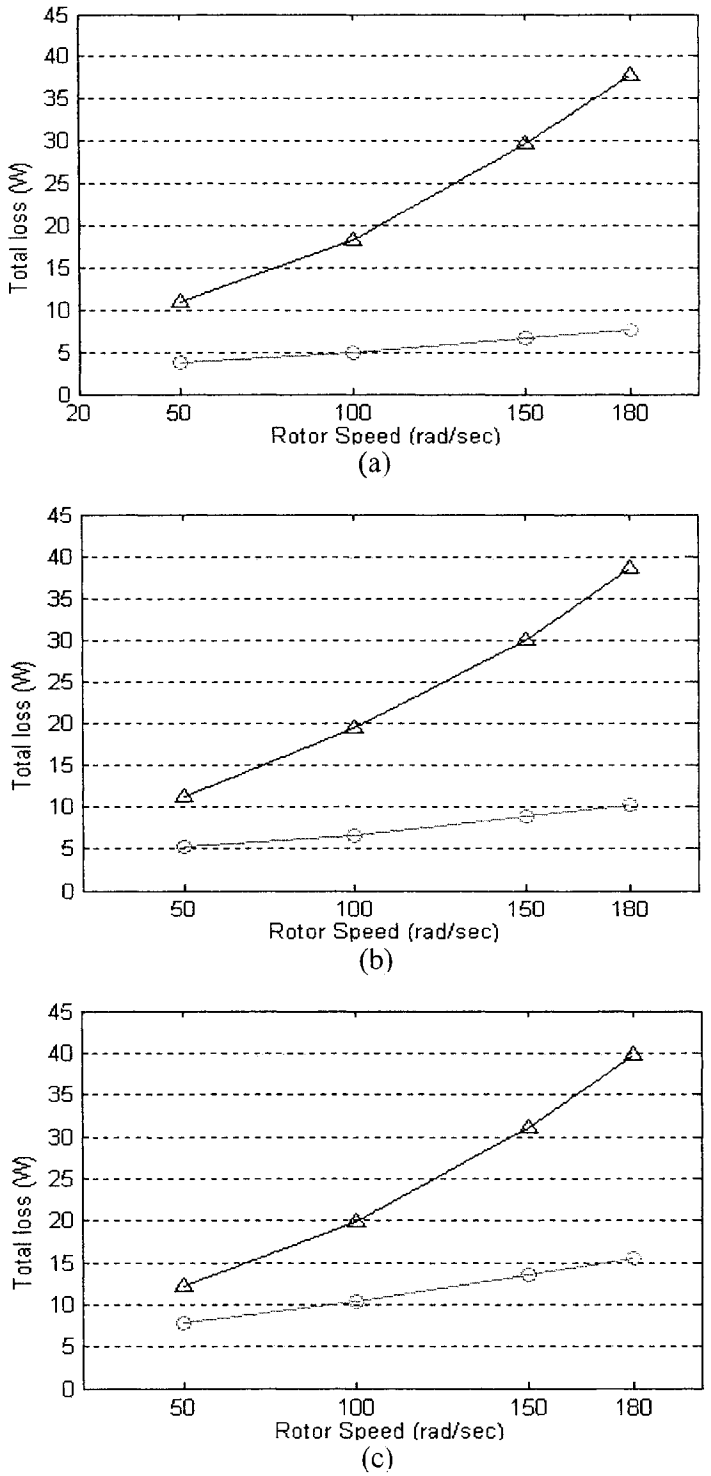

Fig.6.12: Experimental total loss results of the proposed LMA and drive: (a) 16% of the rated load, (b) 22% of the rated load and (c) 34% of the rated load with (○) and without the proposed LMA (Δ).

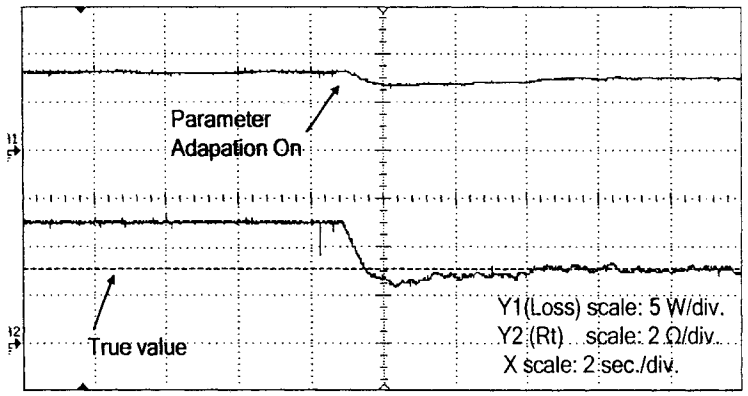

(a)

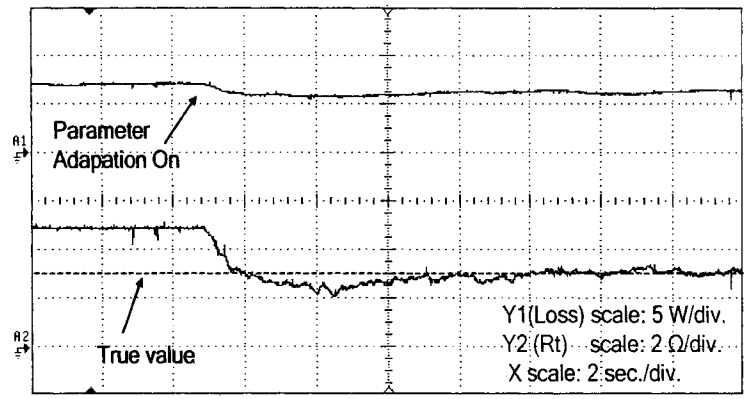

(b)

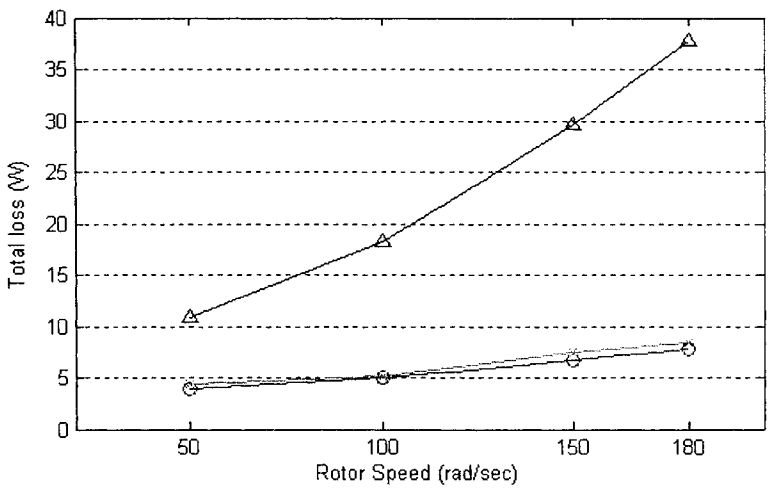

(c)

Fig.6.13: Experimental responses of the proposed ABNC and drive at 16% of the rated load torque: (a) total loss and estimated R_t at 180 rad/sec, (b) total loss and estimated R_t at 150 rad/sec before and after parameter adaptation is on and (c) total losses for the following three cases:

(Δ): vector control with constant magnetizing current

(×): proposed LMA without parameter adaptation

(○): proposed LMA with parameter adaptation

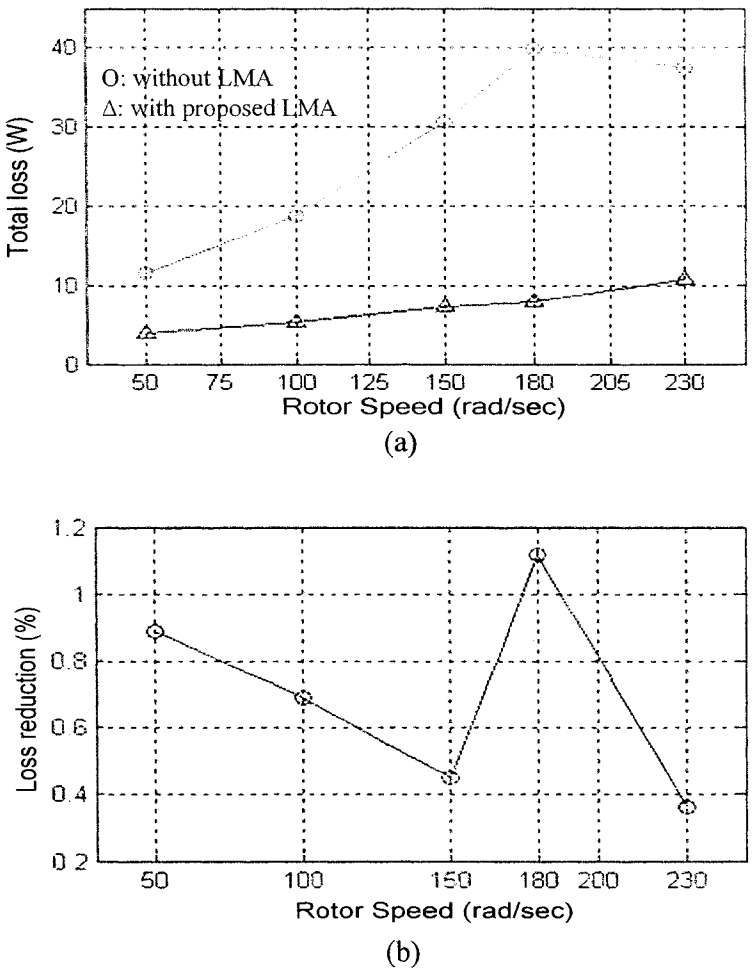

Fig.6.14: Experimental results of the proposed LMA with PI based drive: (a) total loss with/without the proposed LMA (b) extra loss reduction compared to the conventional LMA.

6.6 Concluding Remarks

In this chapter, the detailed DSP based real-time implementation procedures for the proposed IM drive is presented. The complete drive is implemented using a digital signal processor board DS 1104 in a prototype laboratory 1/3 hp induction motor. The implementation involves both hardware and software.

The dynamic performance of the proposed drive and parameter adaptations are investigated at different dynamic operating conditions such as a sudden change of command speed and load disturbance. The experimental results show the robustness of the proposed drive. The effectiveness of the proposed LMA is demonstrated at different speed and load conditions. When the proposed LMA is combined with ABNC, the best experimental results for loss reduction is obtained, which validates the simulation results. The proposed LMA is also tested with the PI controller based IM drive and it is found that the proposed LMA is superior to the traditional LMA in terms of loss reduction.

Chapter 7

Conclusions

As addressed at the opening chapter of this thesis, the loss minimization control of IMs can significantly contribute to overall energy saving considering the fact, that IMs consume more than half of the electric energy generated. At the same time, the excellent dynamic performance of a controller has to be achieved in order to be used in high performance variable speed drive applications. In compliance with these requirements, a new online loss minimization control strategy for IM has been proposed in this thesis. In order to achieve high dynamic performance and further reduction of loss, adaptive backstepping based nonlinear controller (ABNC) has also been proposed. The design, analysis, simulation, real-time implementation and extensive experimental test results have been presented

In Chapter 1, the literature review of various loss minimization algorithms (LMA) and IM control techniques identified the drawbacks of currently available LMAs i.e. a long search time, torque pulsations, demand for the precise knowledge of a loss model, and parameter dependency. A new loss-model based controller (LMC) combined with ABNC has been proposed in order to overcome the limitations and drawbacks of the existing loss minimization controllers. In Chapter 2, the mathematical IM model incorporating the iron loss has been derived. First the IM model was converted from the conventional *abc* to the synchronously rotating *dq* frame by Clarke's and Park's

transformations for the field oriented control (FOC). Then, the motor model was referenced to the rotor magnetizing current, and the resistance that represents the iron loss was added in parallel to the magnetizing current. In Chapter 3, losses that are involved in IM drives were classified and possible methods of loss reduction were explained. A new LMC has been developed based on the steady state motor model in Chapter 2. In Chapter 4, a new ABNC has been developed for the control of the speed and magnetizing current based on the motor model derived in Chapter 2. Step-by-step procedures for the control and parameter adaptation design have been provided. Stability analysis has also been presented. In Chapter 5, the simulation model for the proposed complete drive system has been developed and explained. The extensive simulation results at different operating conditions were also shown. In Chapter 6, the real-time implementation procedures of the proposed control system for the development of both hardware and software have been provided and the experimental results were shown.

From the simulation and experimental results, the proposed LMC has been found to be superior to the conventional one in loss reduction and the proposed ABNC has been found robust against speed changes and load disturbances and showed high dynamic performance. When they were combined together, both high dynamic performance and even more loss reduction, due to the effectiveness of parameter adaptation, have been achieved. Thus, the proposed ABNC based LMC for IM drives could be a potential high performance and energy saving industrial drive application.

7.1 Contributions

The contributions of this dissertation are:

- Mathematical model of an IM incorporating the iron loss has been derived. In these equations, no extra state variables are added while the iron loss is incorporated into the equations. Hence, this set of equation can be used to develop controllers that take iron loss into account without adding too much complexity to the design as compared to the case without considering the iron loss. This will benefit especially, for the nonlinear controller design because the extra state variables introduced to explain the current flowing through iron resistance in conventional motor model caused the difficulties in the design of a nonlinear controller.

- Adaptive backstepping based nonlinear controller (ABNC) for an IM incorporating the iron loss has been developed under the parameter uncertainties of the rotor resistance and load torque. The performance of this controller has been evaluated by both simulation and experimental results showing excellent dynamic performance. Simulation results also show the proposed controller is superior to the one without the consideration of iron loss and it could be a potential candidate for high performance industrial drive application.

- A new LMC based loss minimization algorithm (LMA), which operates an IM at the minimum loss point has been developed based on the steady state motor model described in 1. Due to the decomposition feature of the steady state motor model, the rotor leakage inductance is not ignored. The proposed LMA has been evaluated through the computer simulation and experiment using different types of speed controllers. Both simulation and experimental results

show superior results in comparison to the conventional LMA most popularly used.

- A novel loss minimization control system for IM has been proposed by combining the proposed LMC and ABNC. Simulation and experimental results verified the effectiveness of the proposed control system. It is shown that the parameter adaptation of ABNC contributes to both the dynamic performance of the controller and accuracy in search of an optimum magnetizing current level.

- The proposed adaptive backstepping based online loss minimization control of an IM drive has been successfully implemented in real-time using a digital signal processor (DSP) controller board DS 1104 for a prototype 1/3 hp motor in the Power Electronics & Drives Research Laboratory of Lakehead University. The detailed information about the real-time implementation of both hardware and software has been presented.

7.2 Future Scope of the work

In the implementation phase of this research as shown in Chapter 6, a DS 1104 controller board could easily meet the computing requirement for the digital implementation of the proposed strategy in terms of speed and memory because this is one of the latest research & development boards with a powerful processor. Therefore, there was no need for special effort on conservative use of the computing hardware to reduce the computational burden. However, the use of such a powerful DSP board may not be possible or recommended due to economic concerns in most of the commercial applications. Therefore, it is worth trying to implement the proposed control strategy with less computational burden. This can be done by writing the

entire control system in 'C' programming language with theses concerns in mind. Apart from a possible development of efficient control software, the proposed LMC and ABNC can be used as a stand alone. For example, the proposed LMA can be combined with the conventional PI based controller, and ABNC can be used with a constant magnetizing current with or without parameter adaptations according to the applications.

In this thesis, the parameter update laws for rotor resistance and load torque have been developed. Through the exactly same backstepping controller design steps, the parameter update laws can be easily extended to stator resistance. In contrast to the previous suggestion, the control system computation in this case becomes more demanding. However, in return it might be possible to achieve better results in terms of both dynamic performance and loss minimization.

The effect of core saturation can be incorporated in the development of the proposed LMC by computing the magnetizing inductance as a function of the magnetizing current through experimental measurements.

References

1 R. Fei, E.F. Fuchs, and H. Huang, "Comparison of Two Optimization Techniques as Applied to Three-Phase Induction Motor Design," *IEEE Trans. on Energy Conversion,* vol.4, no.4, pp.651-660, Dec.1989.

2 M. P. Kazmierkowski, R. Krishnan, and F. Blaabjerg, *Control in Power Electronics*, Academic Press, 2002.

3 A. M. Trzynadlowski, *Control of Induction Motors*, Elsevier 2000.

4 S. J. Chapman, *Electric Machinery Fundamentals,* New York, NY: McGraw-Hill, 1999.

5 Paul Cochran, *Polyphase Induction Motors*, CRC, 1989.

6 B. K. Bose, "Power Electronics and Motion Control-Technology Status and Recent Trends," *IEEE Trans. on Industry Applications*, vol.29, no.5, pp.902-909, Sep./Oct. 1993.

7 F. Blaschke, "The principle of Field Orientation as Applied to the New Transvector Closed Loop Control System for Rotating–Field Machines," *Siemens Review*, vol.34, pp.217-220, May 1972.

8 D. W. Novotny and T. A. Lipo, *Vector control and dynamics of AC drives*, Oxford University Press, 1997.

9 A. M. Trzynadlowski, *The field orientation principle in control of induction motors*, Kluwer Academic, 1994.

10 D. G. Tayler, "Nonlinear Control of Electric Machines: An Overview," *IEEE Control Systems*, pp.41-51, Dec.1994.

11 M. Krstic, I. Kanellakopoulos, and P. Kokotovic, *Nonlinear and Adaptive Control Design*, John Wiley & Sons, 1995.

12 F. Khorrami, P. Krishnamurthy, and H. Melkote, *Modeling and Adaptive Nonlinear Control of Electric Motors*, Springer, 2003.

13 R. Marino, S. Peresada, and P. Valigi, "Adaptive Input-Output Linearizing Control of Induction Motors," *IEEE Trans. on Automatic Control*, vol.38, pp.208-221, Feb.1993.

14 R. Ortega, A. Loria, P. J. Nicklasson, and H. Sira-Ramirez, *Passivity-based Control of Euler-Lagrange Systems,* Springer Verlag, London, 1998.

15 H. Tan and J. Chang, "Adaptive Backstepping Control of Induction Motor with Uncertainties," in *Conf. Rec. American Control Conference*, vol.1, pp.1-5, 1999.

16 A. Kusko and D. Galler, "Control Means for Minimization of Losses in AC and DC Motor Drives," *IEE Trans. on Industry Applications*, vol.19, pp.561-570, July/Aug. 1983.

17 D. S. Kirschen, D. W. Novotny, and W. Suwanwisoot, "Minimizing Induction Motor Losses by Excitation Control in Variable Frequency Drives," *IEE Trans. on Industry Applications*, vol.20, pp.1244-1250, Sept./Oct. 1984.

18 H. G. Kim, et al., "Optimal Efficiency Drive of a Current Source Inverter Fed Induction Motor by Flux Control," *IEE Trans. on Industry Applications*, pp.1453-1459, 1984.

19 I. Kioskeridis and N. Margaris, "Loss Minimization in Induction Motor Adjustable-Speed Drives," *IEEE Trans. on Industrial Electronics*, vol.43, pp.226-231, Feb. 1996.

20 P. Famouri and J. J. Cathey, "Loss Minimization Control of an Induction Motor Drive," *IEEE Trans. on Industry Applications*, vol.27, pp.32-37, Jan./Feb. 1991.

21 R. D. Lorenz and S. M. Yang, "Efficiency-Optimized Flux Trajectories for Closed-cycle Operation of Field-Orientation Induction Machine Drives," *IEEE Trans. on Industry Applications*, vol.28, pp.574-580, May/June 1992.

22 G. O. Garica, J. C. M. Luis, R. M. Stephan, and E. H. Watanabe, "An Efficient Controller for an Adjustable Speed Induction Motor Drive," *IEEE Trans. on Industrial Electronics*, vol. 41, pp.533-539, Oct. 1994.

23 C. Chakraborty and Y. Hori, "Fast Efficiency Optimization Techniques for the Indirect Vector-Controlled Induction Motor Drive," *IEEE Trans. on Industry Applications*, vol.39, pp.1070-1076, no.4, July/Aug. 2003.

24 F. Fernandez-Bernal, A. Garcia-Cerrada, and R. Faure, "Model-based Loss Minimization for DC and AC Vector-Controlled Motors Including Core Saturation," *IEEE Trans. on Industry Applications*, vol.36, no.3, pp.755-763, May/June 2000.

25 S. Lim and K. Nam, "Loss-Minimising Control Scheme for Induction Motors," *IEEE Proc-Electr. Power Appl.*, vol.151, no.4, pp.385-397, July 2004.

26 J. C. Moreira, T. A. Lipo, and V. Blasko, "Simple Efficiency Maximizer for an Adjustable Frequency Induction Motor Drive," *IEEE Trans. on Industry Applications*, vol.27, pp.940-946, Sept./Oct. 1991.

27 S. K. Sul and M. H. Park, "A Novel Technique for Optimal Efficiency Control of a Current-Source Inverter-Fed Induction Motor," *IEEE Trans. on Power Electronics*, vol.3, pp.192-199, Apr. 1988.

28 D. S. Kirschen, D. W. Novotny, and W. Suwanwisoot, "On-line Efficiency Optimization of a Variable Frequency Induction Motor Drive," *IEEE Trans. on Industry Applications*, vol.21, pp.610-615, May/June 1985.

29 G. C. D. Sousa, B. K. Bose, and J. G. Cleland, "A fuzzy Logic Based On-Line Efficiency Optimization Control of an Indirect Vector-Controlled Induction Motor Drive," *IEEE Trans. on Industrial Electronics*, vol.42, pp.192-198, Apr. 1995.

30 G. K. Kim, I. J. Ha, and M. S. Ko, "Control of Induction Motors for Both High Dynamic Performance and High Power Efficiency," *IEEE Trans. on Industrial Electronics*, vol.39, pp.323-333, Aug. 1992.

31 C. M. Ta and Y. Hori, "Convergence Improvement of Efficiency-Optimized Control of Induction Motor Drives," *IEEE Trans. on Industry Applications*, vol.37, pp.1746-1753, Nov./Dec. 2001.

32 J. Zhou, Y. Wang, and R. Zhou, "Adaptive Backstepping Control of Separately Excited DC Motor with Uncertainties," in *Conf. Rec. International Conf. on Power System Technology*, vol.1, pp.91-96, 2000.

33 M. Vilathgamuwa, M .A. Rahman, K. Tseng, and M. N. Uddin, "Nonlinear Control of Interior Permanent Magnet Synchronous Motor," *IEEE Trans. on Industry Applications*, vol.39, pp.408-415, Mar./Apr. 2003.

34 H. Tan and J. Chang, "Field Orientation and Adaptive Backstepping for Induction Motor Control," in Conf. Red. *IEEE-IAS Annual Meeting*, vol.4, pp.2357-2263, 1999.

35 H. Tan and J. Chang, "Adaptive Position Control of Induction Motor Systems under Mechanical Uncertainties," in *Conf. Rec. IEEE International Conf. on Power Electronics and Drive Systems*, vol.2, pp.597-620, 1999.

36 C. I. Huang and L. C. Fu, "Adaptive Backstepping Speed/Position Control with Friction Compensation for Linear Induction Motor," in *Conf. Rec. IEEE Conference on Decision and Control*, vol.1, pp.474-479, 2002.

37 H. Shieh and K Shyu, "Nonlinear Sliding-Mode Torque Control with Adaptive Backstepping Approach for Induction Motor Drive," *IEEE Trans. on Industrial Electronics,* vol.456, pp.380-389, Apr. 1999.

38 S. Lin and C. Fang, "Adaptive Backstepping Motion Control of Induction Motor Drives," *Journal of the Chinese Institute of Engineers.* vol.27, pp.449-454, 2004.

39 G. O. Garcia, J. A. Santisteban, and S. D. Brignone, "Iron Losses Influence on a Field-Oriented Controller," in *Conf. Rec. of IEEE IECON'94,* pp.639-644, 1994.

40 S. D. Wee, M. H. Shin and D. S. Hyun, "Stator-Flux-Oriented Control of Induction Motor Considering Iron Loss," *IEEE Trans. on Industrial Electronics*, vol.48, pp.602-608, June. 2001.

41 Emil Levi, "Impact of Iron Loss on Behavior of Vector Controlled Induction Machine," *IEEE Trans. on Industry Application*, vol.31, pp.1287-1296, Nov./Dec. 1995.

42 J. Choi, D. Chung and S. Sul, "Implementation of Field Oriented Induction Machine Considering Iron Losses," in *Conf. Rec. Applied Power Electronics Conference and Exposition*, vol.1 pp.375-379, Mar. 1996.

43 M. Sokola, E. Levi, G. Jamieson and D. Williams, "Representation and Compensation of Iron Loss in Rotor Flux Oriented Induction Machines," *in Conf. Rec., International Conference on Power Electronics, Dries and Energy Systems for Industrial Growth*, vol.1, pp.243-249, Jan.1996.

44 H. Rasmussen, P. Vadstrup and H. Borsting, "Rotor Field Oriented Control with Adaptive Iron Loss Compensation," in *Conf. Red. IEEE-IAS Annual Meeting*, vol.2, pp.1253-1258, 1999.

45 *Simulink User Guide*. The Mathworks Inc., 2004.

46 *dSPACE, Implementation Guide*, Paderborn, Germany, 2003.

47 A. Fransua, N. Margaris, *Electrical Machines and Drive Systems*, Technical Press, 1984.

48 A. H. Bonnett, "Understanding the Changing Requirements and Opportunities for Improvement of Operating Efficiency of AC Motors", *IEEE Trans. on Industry Application*, vol.29, pp.600-610, May/Jun. 1993.

49 F. Abrahamsen, F. Blaabjerg, J. K. Pedersen, P. Grabowski, P. Thogersen, E. J. Petersen, "On the Energy Optimized Control of Standard and High-Efficiency Induction Motors in CT and HVAC Applications," in *Conf. Rec. IEEE-IAS Annual Meeting*, vol.1, pp.621-628, 1997.

50 I. Takahashi, H. Mochikawa, "A New Control of PWM Inverter Waveform for Minimum Loss Operation of an Induction Motor Drive", *IEEE Trans. on Industry Applications*, vol.21, pp.580-587, May/June. 1985.

51 F. C. Zach, H. Ertl, "Efficiency Optimal Control for AC Drives with PWM Inverters," *IEEE Trans. on Industry Applications*, vol.21, pp.60-66, July/Aug. 1985.

52 Krstic, M., Kaneelankopoilos, I., and Kokotovic, P. *Nonlinear and Adaptive Control Design*; John Wiley & Sons, Inc.: New York, 1995.

53 J. J. E. Slotin and W. Li, Applied Nonlinear Control. Englewood Cliffs, NJ: Prentice-Hall, 1991.

54 G. C. Verghese and S. R. Sanders, "Observers for Flux Estimation in Induction Machines," *IEEE Trans. on Industrial Electronics*, vol.35, pp.85-94, 1988.

55 Y. R. Kim, S. K. Sul, and M. H. Park, "Speed Sensorless Vector Control of Induction Motor using Extended Kalman Filter," *IEEE Trans. on Industry Applications*, vol.30, pp.1225-1233, Sept./Oct. 1994.

56 S. W. Nam and M. N. Uddin, "Development of an Adaptive Backstepping based Nonlinear Control of an Induction Motor Incorporating Iron Loss with Parameter Uncertainties," *in Conf. Rec. Canadian Conference on Electrical and Computer Engineering*, Ottawa, Canada, 2006.

57 S. W. Nam and M. N. Uddin, "Model-based Loss Minimization Control of an Induction Motor Drive," in *Conf. Rec. IEEE International Symposium on Industrial Electronics,* Montreal, vol.3, pp.2367-2372, 2006.

58 P. A. Ioannou and J. Sun, *Robust Adaptive Control*, Prentice-Hall, Inc., New Jersey, 1996.

59 M. N. Uddin, "Intelligent control of an interior permanent magnet synchronous motor," *Ph.D. dissertation*, Memorial University of Newfoundland, St. John, Oct. 2000.

60 Jason Lau, "Adaptive Backstepping Based Nonlinear Control of an Interior Permanent Magnet Synchronous Motor Drive," *Master dissertation*, Lakehead University, Oct. 2005.

61 Hao Wen, "Development and Analysis of a Self-tuned Neuron-Fuzzy Controller for Induction Motor Drives," *Master dissertation*, Lakehead University, Oct.2005.

62 Werner Leonhard, *Control of Electrical Drives*, Springer, 2001.

APPENDIX-A

IM Parameters

Parameter	For Simulation	For Experiment
Number of phase	3	3
Number of pole pairs	2	2
Rated power	12 hp	1/3 hp
Rated speed	1750 RPM	1725 RPM
Stator resistance R_s	0.399 Ω	6.5 Ω
Rotor resistance R_r	0.3538 Ω	3.4 Ω
Iron loss resistance R_f	650 Ω	400 Ω
Stator inductance L_s	0.0593H	0.2758 H
Rotor inductance L_r	0.0604H	0.2809 H
Mutual inductance L_m	0.056 H	0.2655 H
Inertia constant J	0.0586 $Kg.m^2$	0.0012 $Kg.m^2$

APPENDIX-B

B.1 Base drive circuit for the inverter

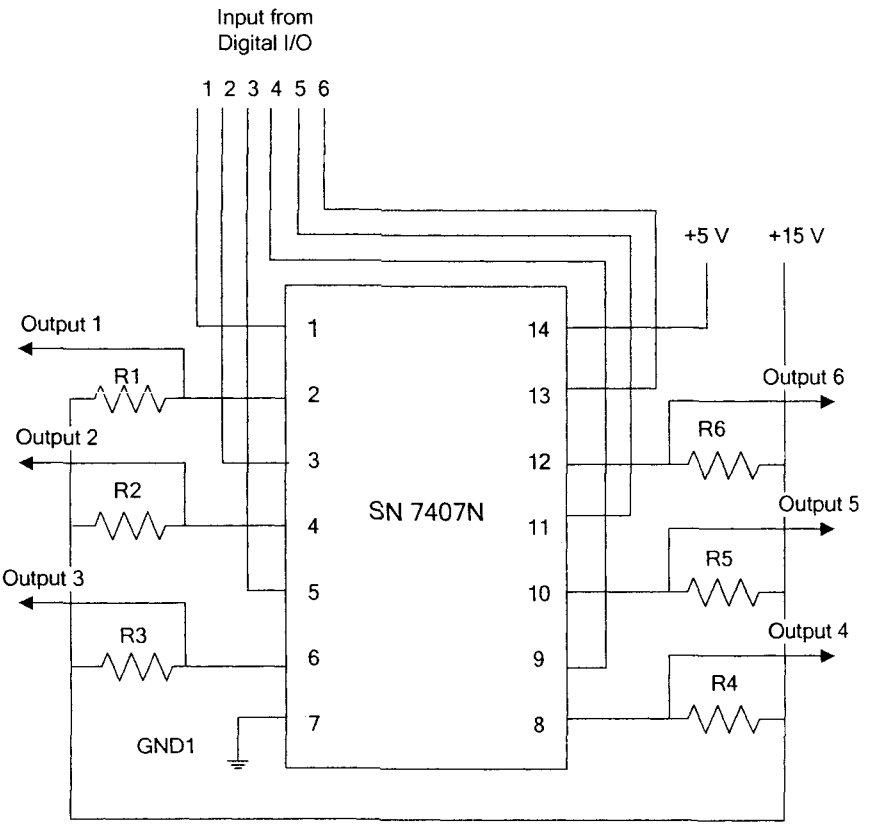

Fig.B.1: Base drive circuit for the inverter

B.2 Interface circuit for the current sensor

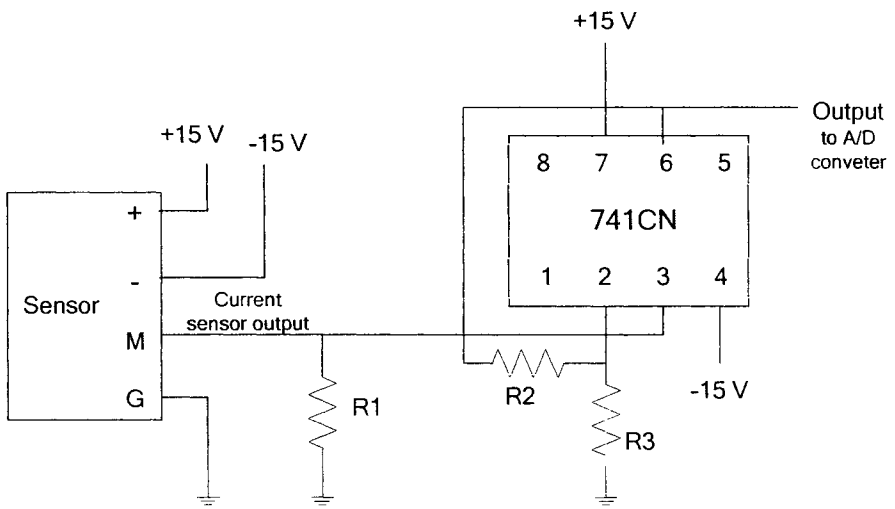

Fig.B.2: Current sensor and Interface circuit per phase

B.3 Field weakening rule

```
function [mag_cur_ref] = fieldweakening(we)
% we: rotor flux speed,
% rated_we: rated rotor flux speed
% mag_cur_ref: magnetizing current reference
% rated_mag_cur_ref: rated magnetizing current reference

    if we <= rated_we
       mag_cur_ref = rated_mag_cur_ref;
    else
       n = we – rated_we;
       mag_cur_ref = rated_mag_cur_ref
       for i=1:n-1
          mag_cur_ref = mag_cur_ref - mag_cur_ref / (we+i);
       end
    end
```

APPENDIX-C

Simulink Model

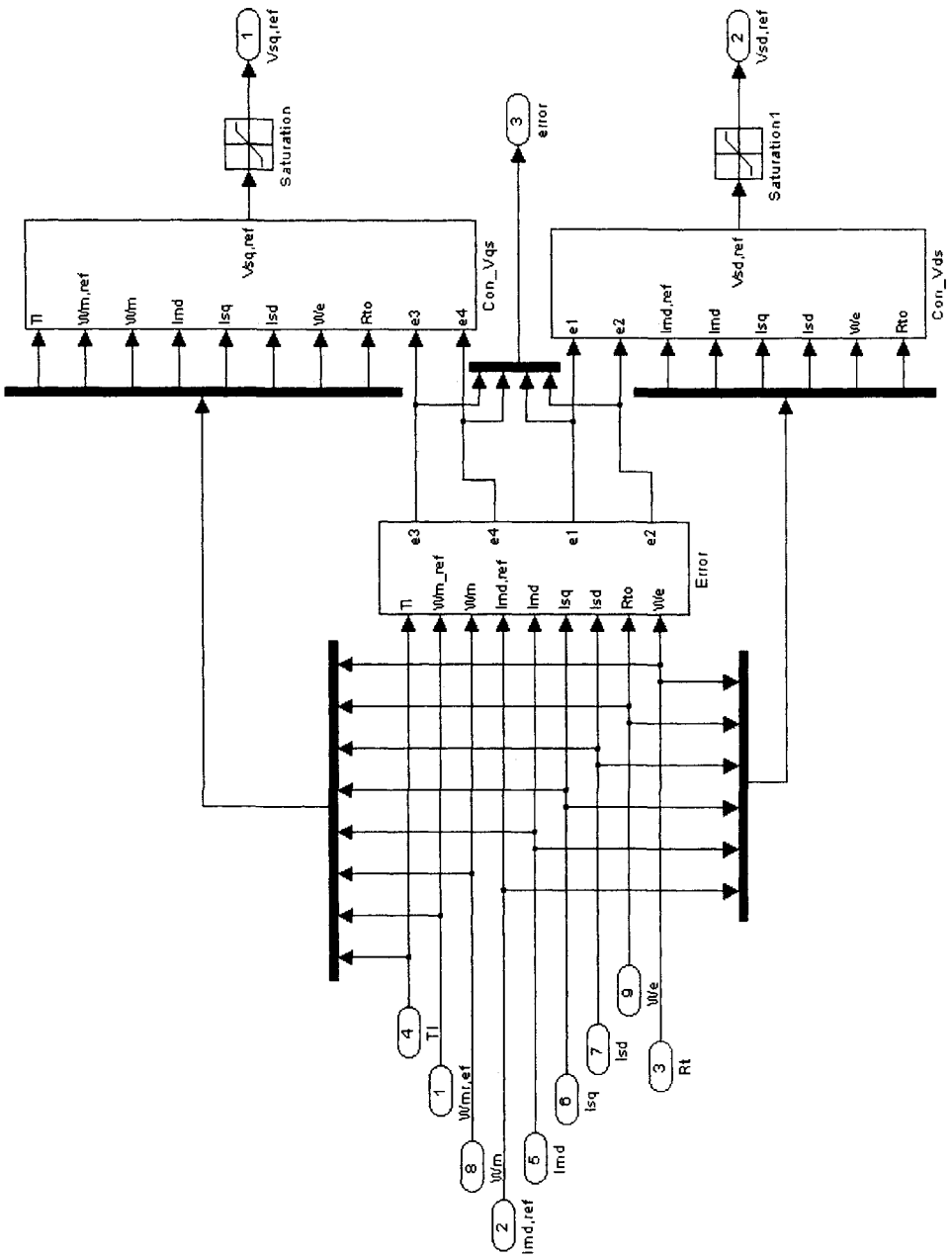

Fig.C.1: Controller Subsystem

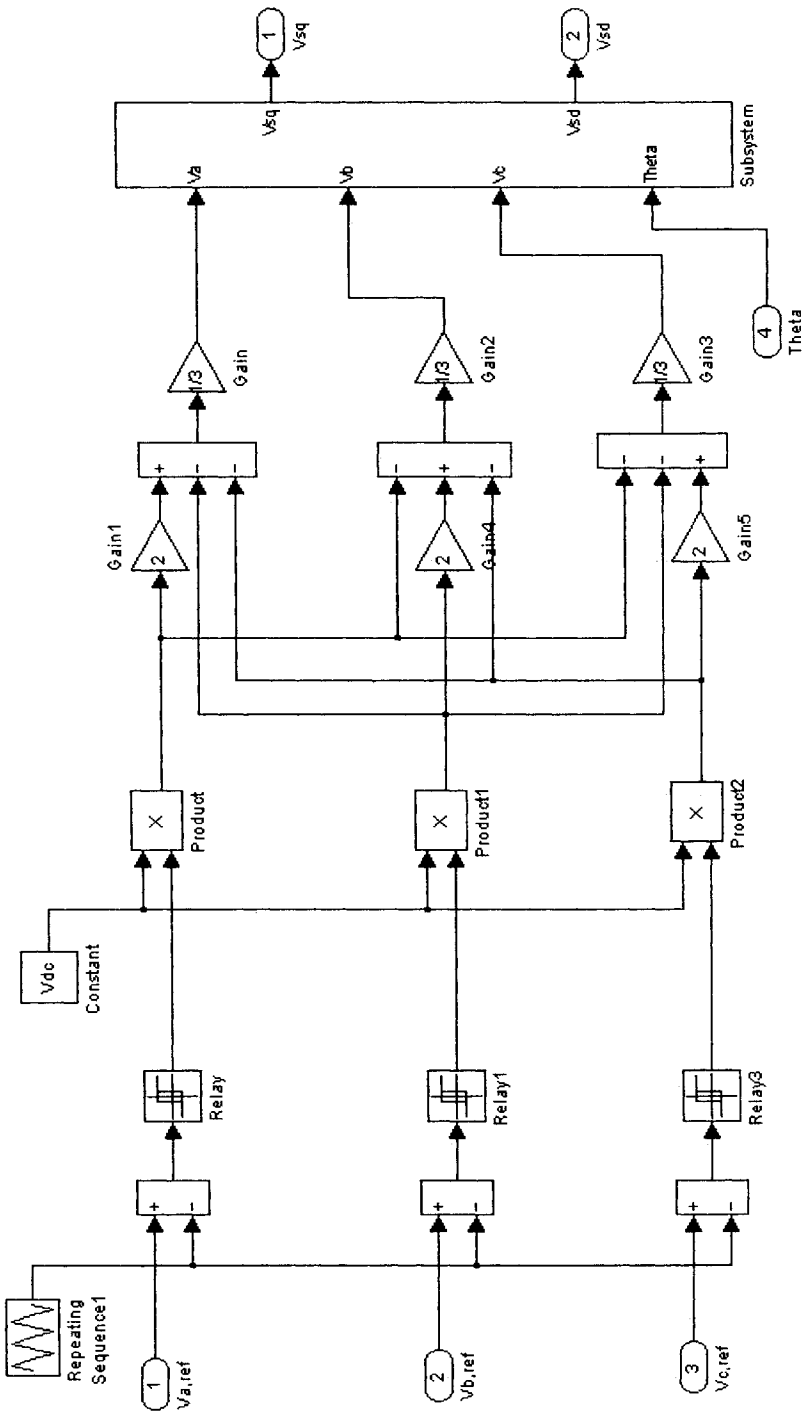

Fig.C.2: PWM Inverter Subsystem

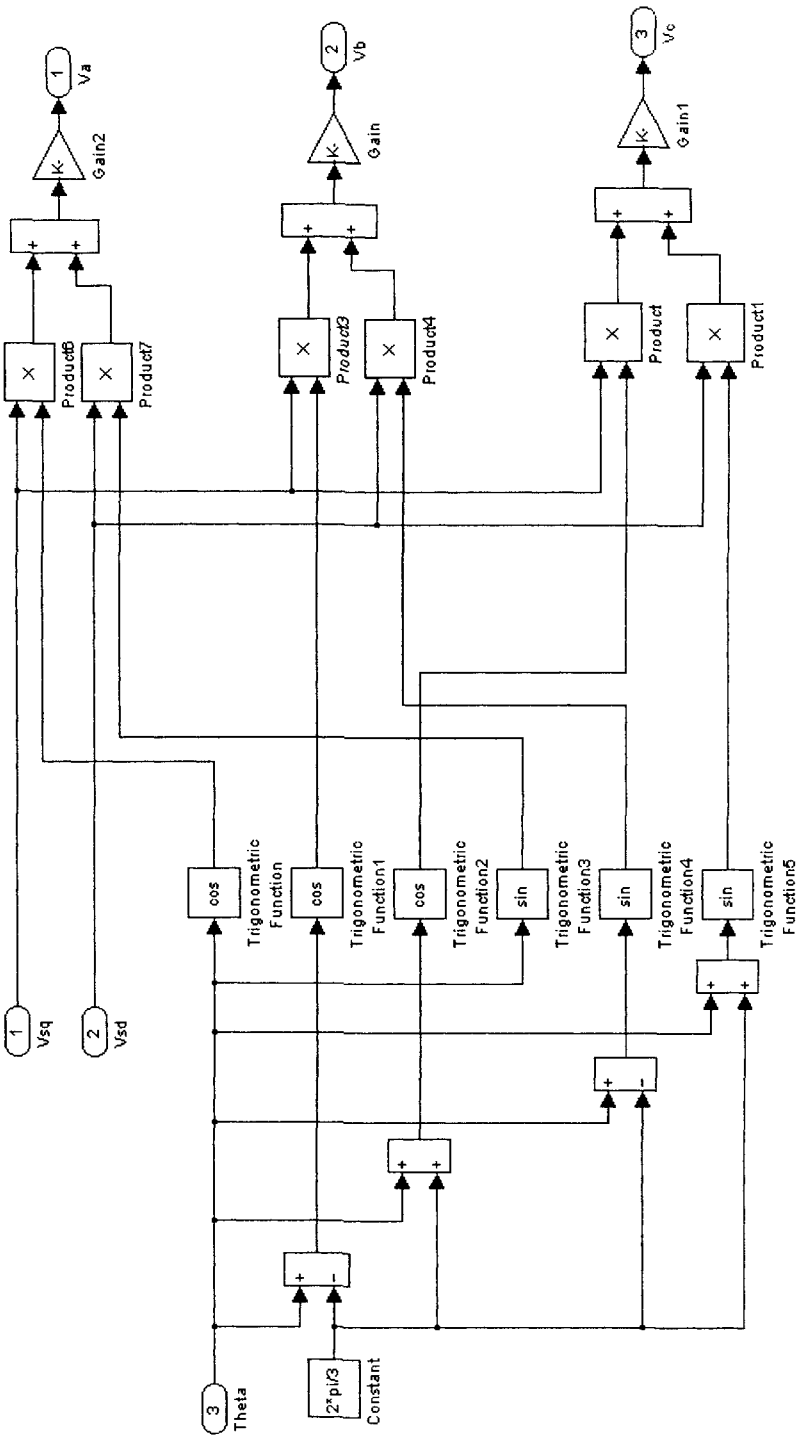

Fig.C.3: Coordinate Transformation Subsystem (dq to abc)

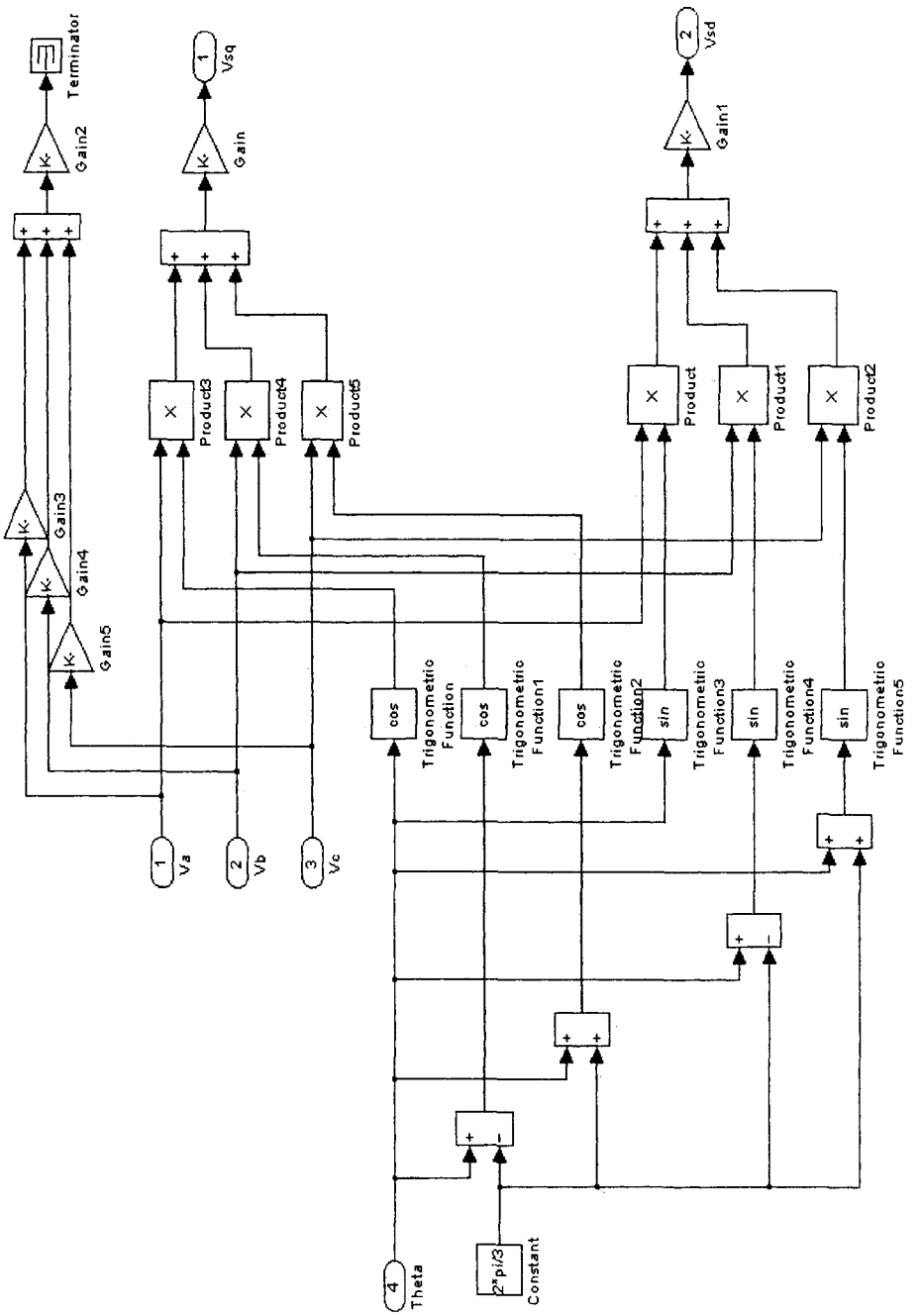

Fig.C.4: Coordinate Transformation Subsystem (abc to dq)

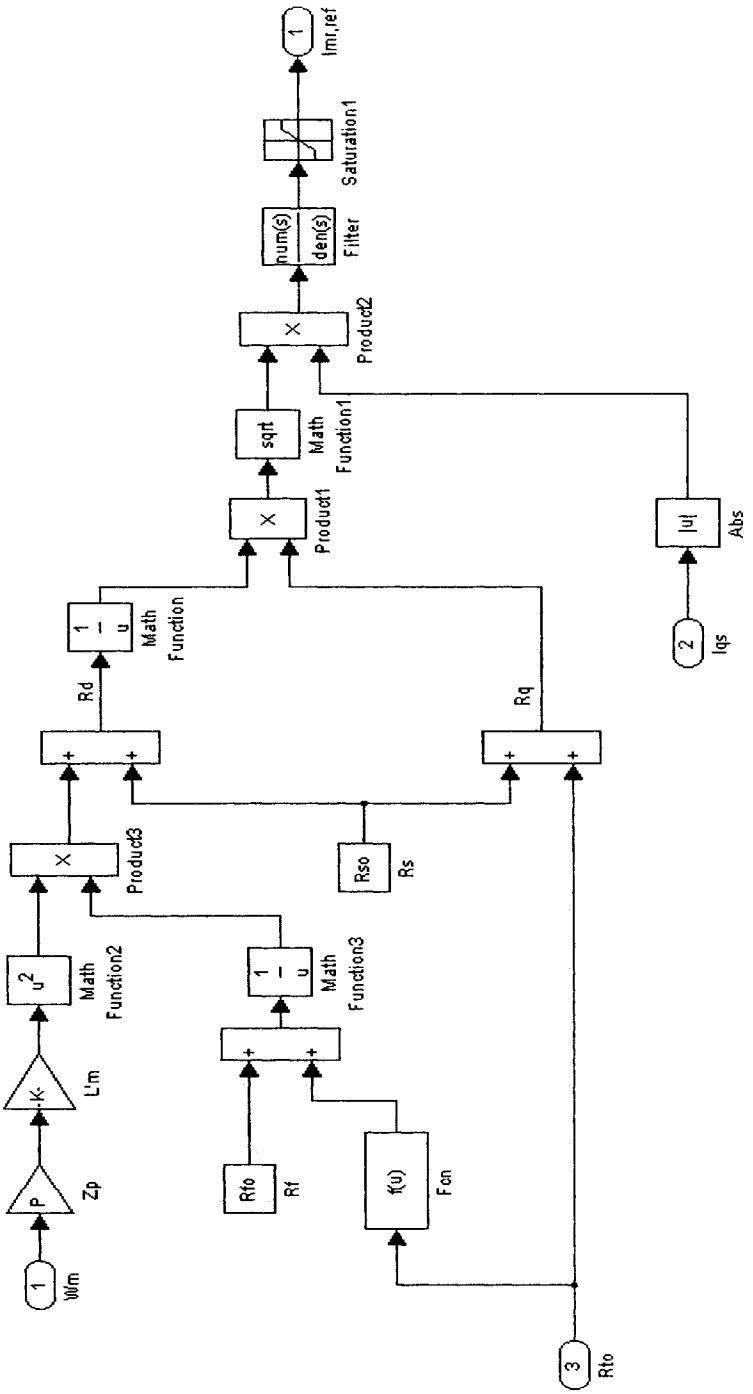

Fig.C.5: LMA Subsystem

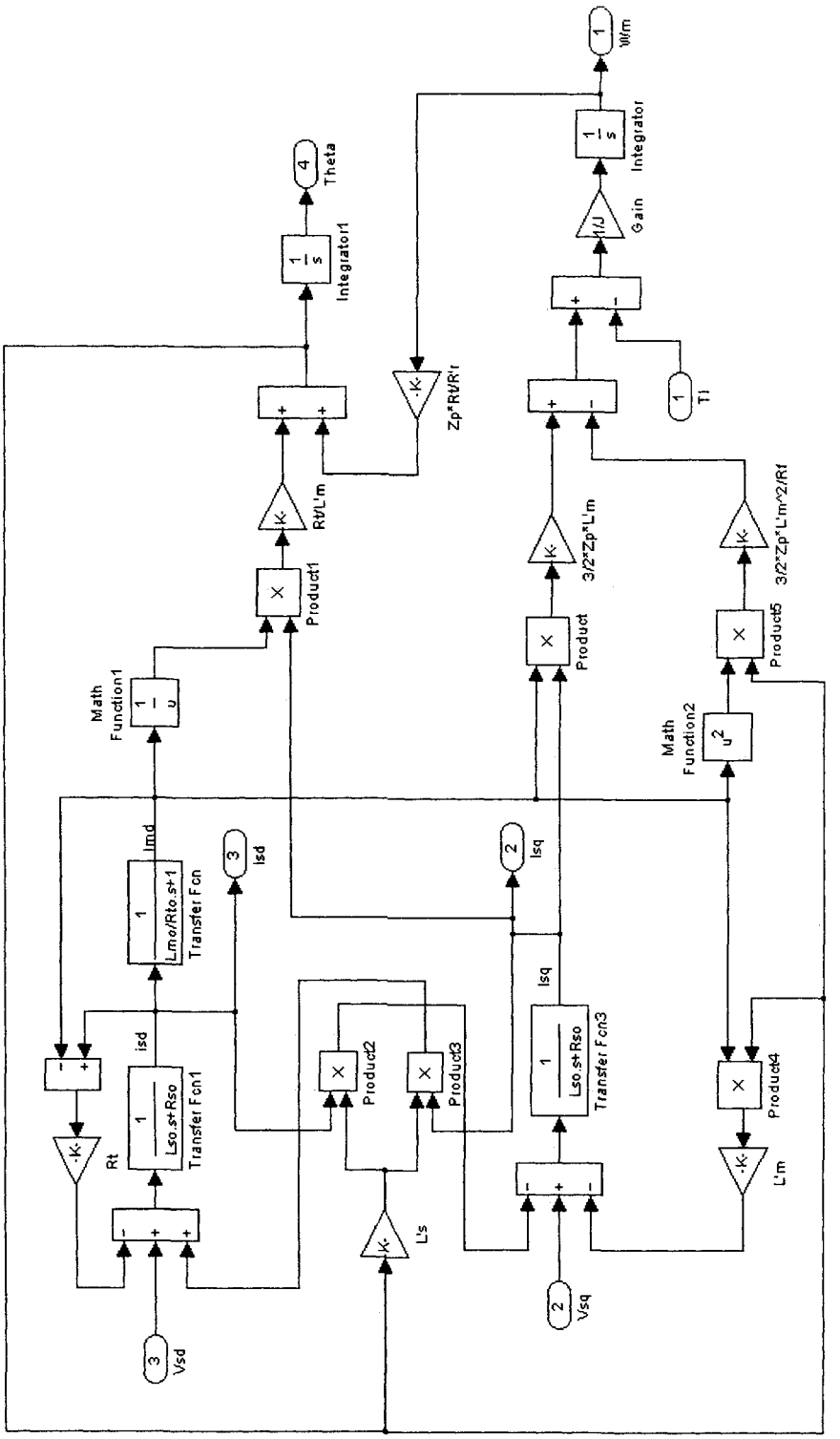

Fig.C.6: Motor Subsystem

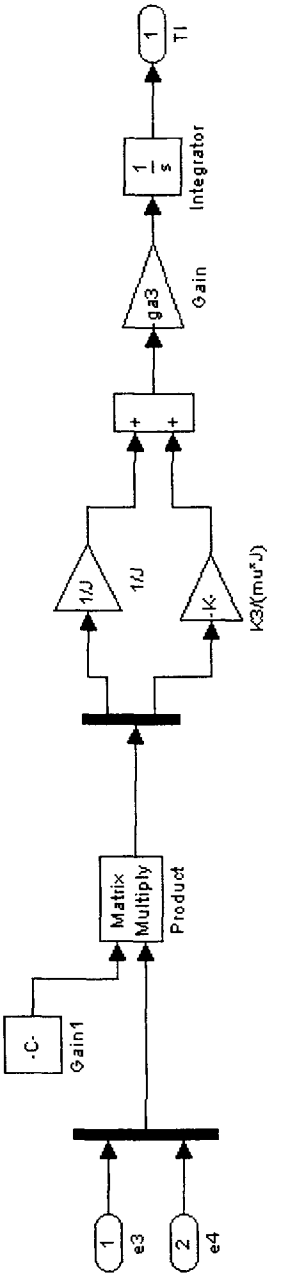

Fig.C.7: Parameter Adaptation Subsystem (Tl)

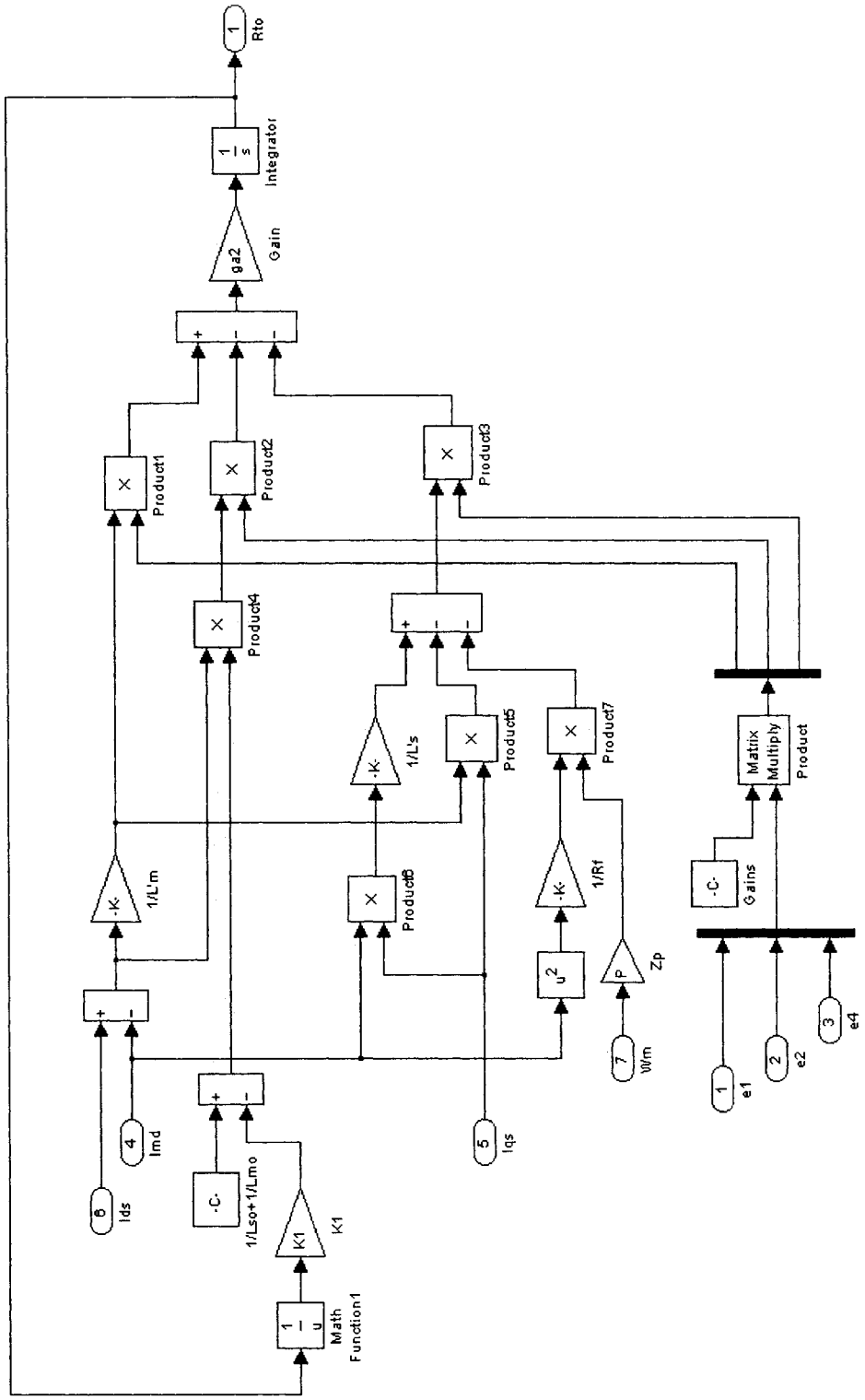

Fig.C.8: Parameter Adaptation Subsystem (Rt)

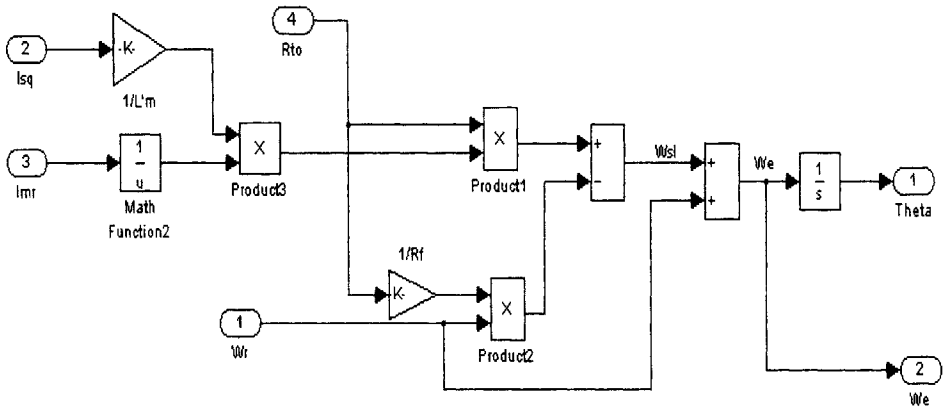

Fig.C.9: Field Angle Generation Subsystem

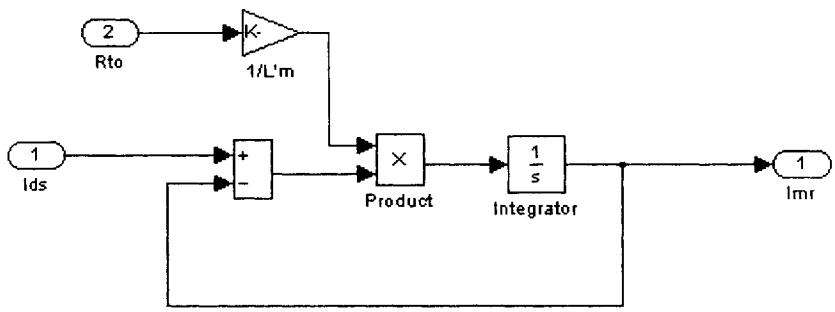

Fig.C.10: Magnetizing Current Estimation Subsystem

APPENDIX-D
Real-Time Simulink Model

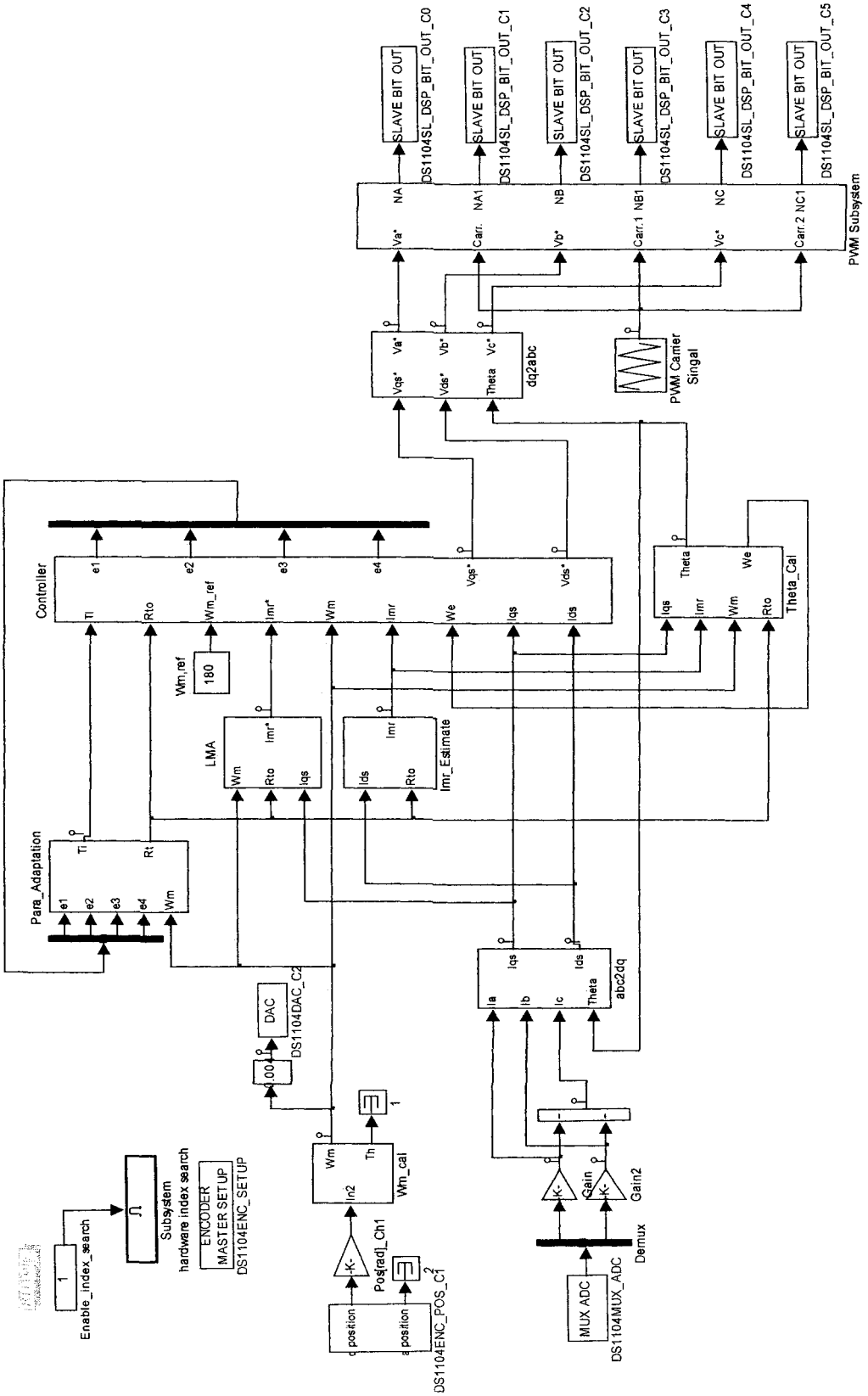

Fig. D: Real time Simulink model for the ABNC based loss minimization control of IM drive